

**MICROFLUIDIC SYSTEMS AND ANALYTICAL TOOLS FOR
GENETIC SCREENING, OPTOGENETICS, AND NEUROIMAGING
OF *C. ELEGANS***

A Dissertation
Presented to
The Academic Faculty

by

Hyewon Lee

In Partial Fulfillment
of the Requirements for the Degree
Doctor of Philosophy in the
School of Chemical & Biomolecular Engineering

Georgia Institute of Technology
May 2013

**MICROFLUIDIC SYSTEMS AND ANALYTICAL TOOLS FOR
GENETIC SCREENING, OPTOGENETICS, AND NEUROIMAGING
OF *C. ELEGANS***

Approved by:

Dr. Hang Lu, Advisor
School of Chemical & Biomolecular
Engineering
Georgia Institute of Technology

Dr. Todd Strelman
School of Biology
Georgia Institute of Technology

Dr. Athanassios Sambanis
School of Chemical & Biomolecular
Engineering
Georgia Institute of Technology

Dr. Joshua Weitz
School of Biology
Georgia Institute of Technology

Dr. Mark Styczynski
School of Chemical & Biomolecular
Engineering
Georgia Institute of Technology

Date Approved: March 29, 2013

To my significant other

ACKNOWLEDGEMENTS

I would like to express my sincere gratitude to my advisor Dr. Hang Lu for providing me with all of the advice, valuable guidance, and gracious support. She encouraged me to move forward with self-confidence. I would further like to thank my thesis committee members for providing me with valuable feedback and guidance. I would also like to thank all the current and past members of Dr. Lu's group. This work would not have been possible without their assistance and support. Finally, I express my greatest gratitude and love to all my family members. My parents always believed in me and supported me with unconditional love and constant encouragement. I also want to acknowledge my brother for all his sacrifice and teaching me to be humble.

TABLE OF CONTENTS

	Page
ACKNOWLEDGEMENTS	iv
LIST OF TABLES	ix
LIST OF FIGURES	xi
SUMMARY	xxv
 <u>CHAPTER</u>	
1 INTRODUCTION	1
1.1 <i>C. elegans</i> as a model system	1
1.1.1 General anatomy and physiology	1
1.1.2 Using <i>C. elegans</i> as a model for neuroscience	1
1.1.3 Tryptophan hydroxylase (TPH-1) as a linker between environmental perception and physiological phenotype	2
1.1.4 Gene expression profiling	3
1.1.5 Genetic screening	4
1.1.6 Cell ablation using optogenetic tool, KillerRed	5
1.2 System for neuroscience research using <i>C. elegans</i>	6
1.2.1 Conventional methods for imaging <i>C. elegans</i>	6
1.2.2 Microfluidics for gene-expression profiling in <i>C. elegans</i>	7
1.3 Thesis objective	9
2 DEVELOPMENT OF HIGH-THROUGHPUT SYSTEM FOR QUANTITATIVE SCREENING	11
2.1 Overview	11
2.2 Motivation and limitations of current microfluidic devices	14

2.3 High-throughput one-layer microfluidic device for a robust and reliable performance	14
2.3.1 Device fabrication	17
2.3.2 <i>C. elegans</i> culture, sample preparation, and isolation of putative double mutants	18
2.3.3 Device operation	19
2.3.4 Numerical model for characterizing the deformation of the membrane for valve operation	20
2.4 Quantitative Screen of target of interest	23
2.4.1 Necessity of quantitative analysis	24
2.4.2 Image analysis	25
2.5 Challenges of this screening	28
2.5.1 Stochastic effects	28
2.5.2 Day-to-day variation	34
2.6 Screening with adaptive algorithm	35
2.6.1 Use of an adaptive algorithm for sorting mutants	35
2.6.2 Isolation of putative mutants	37
2.7 Statistical analysis to characterize putative mutants	39
2.8 Phenotypical groupings based on probability distribution fitting	40
2.9 Conclusions	42
3 MODELING ANALYSIS OF POTENTIAL UNC-43/CAMKII-DEPENDENT REGULATORS OF TPH-1 EXPRESSION	43
3.1 Overview	43
3.2 Background	44
3.3 Model development	49
3.4 Model formulation of <i>tph-1</i> regulation in ADF neurons	51
3.4.1 Model equations	51

3.4.2	Parameter optimization with experimental data	54
3.5	Perturbing model parameters	56
3.5.1	Sensitivity analysis	56
3.5.2	Possible candidates from isolated mutants for UNC-43-interacting factors	61
3.5.3	Robustness test	63
3.6	Stochastic effects	65
3.6.1	Stochastic models to match the population variations in unc-43 mutants	65
3.6.2	Analysis of distribution of isolated mutants	70
3.5.3	Stochastic models for characterizing wild-type phenotypes	71
3.7	Conclusion	73
3.8	Future work	74
3.8.1	Testing hypothesis of bistability	74
3.6.2	Incorporation of Ca ²⁺ signalling pathway	76
4	DESIGN AND CONSTRUCTION OF MULTI-CHANNEL DEVICE FOR HIGH DENSITY TARGET-SELECTIVE STIMULATION OF C. ELEGANS	78
4.1	Overview	78
4.2	Motivation and limitations of single-channel devices	79
4.3	Materials and methods	81
4.3.1	KillerRed-expressed C. elegans strain	81
4.3.2	Fabrication of devices	81
4.3.3	System operation and bacteria preparation	82
4.3.4	Microscopic setup for optical ablation and imaging cells	82
4.3.5	Computational Fluid Dynamics	83
4.3.6	Behavior assay	84

4.4 Results and discussion	84
4.4.1 Design of microfluidic device	84
4.4.2 Simple and efficient trapping mechanism	87
4.4.3 Loading efficiency depending on design geometry	88
4.4.4 Easy recovery without damaging animals	94
4.4.5 Controlled delivery of chemicals, media, and bacteria	96
4.4.6 Parallel optical ablation of trapped worms	98
4.4.7 Simultaneous selective ablation of target neurons and long-term monitoring	100
4.4.8 Post-illumination recovery and behavior assay	104
4.5 Conclusion	107
5 THESIS CONTRIBUTIONS AND FUTURE WORK	108
5.1 Thesis contributions	108
5.2 Future work	111
5.2.1 Characterization of different responses from different cellular and subcellular features based on selective illumination	111
5.2.2 Neuro-imaging responding to chemical stimulation using microfluidics	112
5.2.3 Imaging L1 stage (early developmental stage) of animals	113
REFERENCES	116

LIST OF TABLES

	Page
Table 2.1: Comparison between single-layer and double-layer devices.	17
Table 2.2: Characterization of the sorting algorithm using wild-type (as a surrogate of the double mutant) and <i>unc-43 (gf)</i> mutants. Mixing different percentages of WT in <i>unc-43 (gf)</i> and choosing different threshold give different levels of enrichment. The false positives are a result of the stochasticity in gene expressions (as illustrated in previous figures), rather than a result of the algorithm. In the actual screen, it is difficult to know what the true occurrence of double mutants are; we arbitrarily chose 2% as screening threshold, but verified that 43 of all the mutants selected are true mutants with a secondary clonal expression profiling (see text and Fig. 2.1, Fig. 2.10, Fig. 2.12).	32
Table 3.1: The production rate given the combination of each occupancy status of promoter site in first and second copy	54
Table 3.2: Parameters assumed to be not perturbed	56
Table 3.3: Parameter set obtained by optimization with experimental data of average expression level at each temperature through deterministic steady state model	56
Table 3.4: Parameters optimized for stochastic effects in CaN activity	66

Table 3.5: Parameters obtained for stochastic effects in CaMKII activity	72
Table 4.1: Design considerations for optimal operation	90

LIST OF FIGURES

	Page
Figure 2.1: Schematics of screening strategy based on adaptive algorithm	13
Figure 2.2: 3D image of single-layer device (top) and optical micrograph of the imaging zone in a microdevice (bottom). The channels were filled with color dye to visualize features: blue, cooling channel; green, control valves; and red, sample flow channel.	16
Figure 2.3: The fabrication process of the single-layer microchip	18
Figure 2.4: Numerical models of membrane deformation. (a) The deformation of the disk-shaped membrane is a strong function of pressure. At a low pressure (5 psi, left/front), the membrane has a smaller deformation, as compared to a higher pressure (10 psi, right/back). Color scale represents the vertical displacement of the membrane in microns (μm). (b) and (c), The normalized cross-sectional diameter of the dome-like deformed membrane also depends on membrane properties, including the Young's modulus (b) and aspect ratio as defined by ratio of diameter to thickness (c). The solid squares and circles represent data for sensors with the membrane edge anchored. The hollow squares and circles are data for sensors with 5 μm edge displacement in the membrane.	22
Figure 2.5: Simplified mechanism for CaMKII-dependent regulation of <i>tph-1</i> in ADF neurons	23

Figure 2.6: Stochasticity in gene expressions in a genetically identical population. (a) Probability histogram of *tph-1* expression levels in single mutant (*unc-43*). The n value represents number of worms imaged. (b-e) Representative images of *tph-1* expressions in ADF neurons in *unc-43(gf)*, which correlate with each quantified bar in histogram (a). All fluorescent images are revised as a heat map for clarity. The color bar on the left represents the average intensity of target neurons, ADFL/R, which correlates with the expression levels of *tph-1*.

25

Figure 2.7: Quantitative analysis for expression levels of *tph-1* in ADF neurons with 1) Flattening *z*-stack images, 2) Thresholding images for ADF neurons identification, 3) Localization of neuron centers, and 4) Summing and averaging all pixel intensities within a define ROI.

27

Figure 2.8: Comparison of two quantitative analyses. Various targets (ADF and NSM neurons in wild-type and mutants at either 20 °C or 25 °C) are represented in different color. Red fitting curve shows a linear correlation with $R^2=0.844928$

Figure 2.9: Probability histogram of *tph-1* expression levels in between wild-type and single mutant (*unc-43(gf)*).

29

Figure 2.10: a), b) Occurrences of true positives (blue curve) among all sorted positives (blue shade) depend on the occurrences of the desired population among all animals. c) Overlaying the wild-type population, the *unc-43 (gf)* population, and the mutagenized population expression profiles. This demonstrates that the expression profile of the mutagenized population, which contains desired double mutants, is shifted from the *unc-43 (gf)* single mutants as expected. This also demonstrates that there are significant overlaps among the three populations such that any sorted mutants will need to be verified in secondary clonal imaging to be sure that they are true double mutants, rather than single mutants that stochastically show low expressions. 30

Figure 2.11: Applying different thresholds to the same mixed populations will result in either higher chance to find true positives but at a cost of higher false positives, or smaller false positive rates but at a cost of possibility of missing some true positives. 31

Figure 2.12: Illustration of the stochastic effect of gene expression resulting in overlaps in the expression profiles of isogenic populations. Because of this effect, wild-type or double mutant animals may have a higher expression than single mutant animals, and this effect results in an ultimate limit of enrichment for separations (depending on the size of the subpopulations). 33

Figure 2.13: Empirical cumulative distribution functions of *tph-1* expression for a different set of worms, which illustrate day-to-day variations. Then value represents number of worms imaged. 35

Figure 2.14: Schematics of adaptive screening algorithm for a single worm. Quantitative analysis is only applied to worms having dim TPH-1::GFP. The screening threshold is heuristically updated by every 50 images and possible double mutant is sorted based on threshold. 36

Figure 2.15: Quantitative screening with the adaptive algorithm. (a) The scattered plot showing *tph-1* expression levels in mutagenized *unc-43* worms. Each circle represents single worm intensity (average of two ADF neurons). Worms in shaded regions are bright enough to be identified by eyes due to high expression level of *tph-1*, which is above a certain threshold, and thus, it does not require to be quantified during actual screening. An example of high (b) and low (c) *tph-1* expression in ADF neurons. Mutant (M) selection in quantitative screening with flexible thresholds which are updated after every 50 worms. The first screening criterion is set based on minimum value (Min) of first 50 images. 37

Figure 2.16: The average expression levels of *tph-1* in all progenies from isolated putative mutants were compared to *unc-43(gf)*. Statistically all mutants showed significant differences from *unc-43(gf)* ($p < 0.01$). 40

Figure 2.17: The Characterizations of putative mutants. (a) 13 putative mutants have temperature-dependent changes in *tph-1* expression. (b-d) Three types putative double mutants that have temperature-dependent phenotype of *tph-1* expression in ADF neurons. Each probability histogram of *tph-1* expression levels fits with either Gaussian (b), Gamma (c), or double Gaussian distribution (d). 41

Figure 3.1: Boxplot of *tph-1* expression in a) ADF and b) NSM neurons in wild-type (GR1333, n=64 and 89 respectively), *unc-43(gf)* (ZC5, n=105 and 153 respectively), and *unc-43(lf)* (ZC3, n=93 and 66 respectively), at 20 °C or 25 °C. Differences between culture temperature in each strain, and differences induced by genetic factors in 20 °C were analyzed statistically for both ADF and NSM neurons. Statistical significance are marked as followed (***: $p < 10^{-20}$, **: $p < 10^{-10}$, *: $p < 0.05$) 47

Figure 3.2: The currently known temperature-responsive regulatory pathways of *tph-1* expression in ADF neurons with some putative details (arrows) still to be experimentally confirmed. ILS, TGF- β , and Ca^{2+} signaling pathways are involved in this regulation. 48

Figure 3.3: The schematic of simplified model network of *tph-1* transcription in ADF neurons. Parameters v_1-v_6 are kinetic parameters in phosphorylation pathway. k_1-k_2 are threshold for feedback regulation of CaMKII and CaN respectively. Two transcriptional factors regulate *tph-1* expression: inhibitor *I* and activator *A*. Due to lumped components, *I* can be regarded as ILS downstream component, and *A* represents TGF- β downstream regulator as well. Active CaMKII (either Ca²⁺-bound CaMKII or *unc-43(gf)*) increases *tph-1* expression level by inhibiting *I* (through v_2) and activating *A* (through v_4)

51

Figure 3.4: Scattered plot of average output (*tph-1* expression) variation with average parameter variation. Output variation represents deviation from the experimental average expression of *tph-1*. Parameter set having minimum average output variation was selected. Tested number of samples is $>10^6$ but here only example of 5,000 points were visualized

55

Figure 3.5: a) Changes of average *tph-1* expression in *unc-43(gf)* at 20 °C (blue) and 25 °C (red) by v_1 (see Fig. 3.3) variation. Squares represent average *tph-1* expression in *unc-43(gf)* at 20 °C (blue) and 25 °C (red) with the optimal parameter (v_1 is assumed to be a constant, 1). b) Zoomed in image of the boxed region in a. c) Zoomed in image of the boxed region in b. A total of 500 variations were simulated

58

Figure 3.6: a) Changes of average *tph-1* expression in *unc-43(gf)* at 20 °C (blue) and 25 °C (red) by v_2 (see Fig. 3.3) variation. Squares represent average *tph-1* expression in *unc-43(gf)* at 20 °C (blue) and 25 °C (red) with the optimal parameter (v_2 is optimized as 1.2472). b) Zoomed in image of the boxed region in a. c) Zoomed in image of the boxed region in b. A total of 500 variations were simulated

59

Figure 3.7: a) Changes of average *tph-1* expression in *unc-43(gf)* at 20 °C (blue) and 25 °C (red) by v_3 (see Fig. 3.3) variation. Squares represent average *tph-1* expression in *unc-43(gf)* at 20 °C (blue) and 25 °C (red) with the optimal parameter (v_3 is optimized as 3.317). b) Zoomed in image of the boxed region in a. c) Zoomed in image of the boxed region in b. A total of 500 variations were simulated.

60

Figure 3.8: Allowable range of *tph-1* expression generated by each parameter changes. Each line indicates the possible changes in average *tph-1* expression levels at two temperatures based on simulation. Red triangles represent experimental results of mutant alleles in the allowable range of the phenotypical space, which may potentially carry mutations downstream from CaMKII

62

Figure 3.9: Comparison of phenotypic changes generated by model and average expression levels of putative mutants. Fig. 3.8 is zoom-in view of Fig. 3.9 (see y-axis). Red triangle indicates that phenotypes of double mutants exist within the allowable range generated by parameter changes. Black diamonds represent phenotypes of double mutants having larger differences of *tph-1* expressions at the two temperatures

63

Figure 3.10: The simulation results of changes in average *tph-1* expression at 20 °C and 25 °C by variation parameter v_2 from 91 parameter sets. These parameter sets are generated from 10^6 random sampling; then, 91 parameter sets are selected based on defined error (here, 10 (AU)) compared to experimental results. Each line constituted with circles showing the possible changes in *tph-1* expression by v_2 variation at each parameter set. Red triangle indicates that phenotypes of double mutants exist within the allowable range generated by parameter changes from the optimal set (see section 3.4.2 and Fig. 3.9). Black diamonds represent phenotypes of double mutants used not to be within the range by single parameter variation from the optimal set

64

Figure 3.11: The simulation results of changes in average *tph-1* expression at 20 °C and 25 °C by variation parameter v_4 from 137 parameter sets. These parameter sets are generated from 1.5×10^6 random sampling; then, 137 parameter sets are selected based on defined error (here, 10 (AU)) compared to experimental results. Each line constituted with circles showing the possible changes in *tph-1* expression by v_4 variation at each parameter set. Red triangle indicates that phenotypes of double mutants exist within the allowable range generated by parameter changes from the optimal set (see section 3.4.2 and Fig. 3.9). Black diamonds represent phenotypes of double mutants used not to be within the range by single parameter variation from the optimal set

65

Figure 3.12: The numerical trajectories of number of molecules as a function of time, generated by Gillispie algorithm. Here, we measured the *tph-1* expression levels in *unc-43(gf)* at 25 °C. A total of 100 iterations were simulated

67

Figure 3.13: The histogram of experimental results of *tph-1* expression in *unc-43(gf)* at 20 °C and 25 °C

67

Figure 3.14: a) The histogram of experimental results of *tph-1* expression in *unc-43(lf)* at 20 °C and 25 °C. (Same x-scale in Fig. 3.13 for comparing the genetic influence on target gene expression.) b) zoom-in view of a) to visualize the changes of distribution by temperature

68

Figure 3.15: The histogram based on simulation results of *tph-1* expression in *unc-43(gf)* at 20 °C and 25 °C; the model parameters are roughly optimized to fit the experimental results

69

Figure 3.16: The histogram based on simulation results of *tph-1* expression in *unc-43(lf)* at 20 °C and 25 °C. The profile here also fits the experimental results 69

Figure 3.17: The simulation results of coefficient of variation (CV) in *tph-1* expression at 20 °C and 25 °C by changes of each parameter. Each line indicates the possible changes by each parameter variation. Orange circles represent experimental results of mutant alleles that have negligible temperature dependency based on statistical analysis ($p > 0.01$). Only seven of them exist within the allowable narrow range generated by changes of parameters from the optimal values (see section 3.4.2) 71

Figure 3.18: The histogram of experimental results of *tph-1* expression in wild-type at 20 °C and 25 °C 72

Figure 3.19: The histogram of simulation results of *tph-1* expression in wild-type at 20 °C and 25 °C. The parameters are optimized roughly to consider experimental results of *tph-1* expression 20 °C and (especially) 25 °C 73

Figure 3.20: Preliminary results of temperature shift experiment (20 °C to 25 °C). Animals are initially cultured at 20 °C to become adults; here, we used this as a reference (0hr) before the shift. Every 3 hr after shifting temperature, the expression levels of *tph-1* were measured. b) zoom-in view of a) to visualize the temperature dependent distribution changes 75

Figure 3.21: The histogram of experimental results of *tph-1* expression in double mutants: *unc-2; unc-43(gf)* at 20 °C and 25 °C. This experimental result agrees well with observation by Estevez *et al.* 77

Figure 4.1: Optical micrograph of the high-density array device. The channels were filled with colored dye for visualization. 85

Figure 4.2: The schematics of multi-channel device showing the array of 140 trapping channels connected to the serpentine channel. Zoomed in views of the boxed region showing microfluidic components to enable efficient single-worm loading and continuous media delivery: A, serpentine channel; B, the inlet of trapping channel; C, trapping channel for imaging individual worms; D, restriction channels; E, resistance channels; F, slanted protrusion for fast recovery. White arrows represent the direction of flow which can carry worms and chemicals; specifically, Q_A represents stream flowing along the serpentine channel and Q_B indicates a stream into the trapping channel. 86

Figure 4.3: The Optical photographs showing *C. elegans* loading in the trapping channels. a)-d) Sequential images showing the single worm trapping in a channel in a few seconds. e) Optical photographs of the whole chip loaded with *C. elegans* (97.7% occupancy). Red triangles point at traps successfully loaded with single worms; white triangles at empty channels. 88

Figure 4.4: Loading efficiency optimized with channel geometry, particularly angle between the trapping channel and the serpentine channel (θ). a) The bar graph showing the channel occupancy as a function of channel angle and flow rate. b) The graph representing the loading efficiency of *C. elegans* with 1mM tetramisole to remove worms' mobility. 91

Figure 4.5: The plot of the flow ratio between serpentine and imaging channel at different angles based on COMSOL simulation. 92

Figure 4.6: The orientation of loaded worms depending on flow rates, the mobility of animals, and angles between the trapping channel and the serpentine channel (θ). The bar graphs showing the head-bias of trapped animals a) without and b) with 1mM tetramisole. 93

Figure 4.7: The slanted protrusion enables high-throughput recovery of animals. a) Sequential images showing the efficient recovery of animals. Worms are prevented from swimming into resistance channel while traveling along the serpentine channel. Red star indicate the protrusion feature. b) The bar graph showing the comparison of recovery rates with and without slanted wall. c) Representative image of empty resistance channel showing the successful recovery due to protrusion. d) Optical photograph showing the animals re-trapped to the resistance channel after recovery in the case of no slanted protrusion. e) and f) plots showing the flow stream lines e) with and f) without protrusion wall using COMSOL simulation 95

Figure 4.8: a) Temporal selective chemical delivery in multiple locations (including the channel in the first and last row) in a microdevice as a function of time. Channels were occupied with worms. Different color represents different locations in the device. b) Spatial-selective stimulation caused by tuning of the flow rates from two purple and green stimulants. 97

Figure 4.9: Fluorescent images of ablation on mechanosensory neurons of *C. elegans* in the device. The zoom-in views (20x) of each boxed region showing GFP signals of ALMs and PLMs a) before illumination and b) 24 hours after illumination. Green arrowheads and asterisks represent GFP signals of undamaged neurons and their death, respectively. 99

Figure 4.10: Selective neuronal ablation on the device. a) Fluorescent images of ALMs and PLMs of a single worm showing selective PLMs ablation. PLMs were illuminated for an hour with green light and imaged after one-day culture on the device. Green arrowheads and asterisks point to intact and vanished GFP signals on PLMs respectively; white arrowheads indicate control ALMs which has no changes. b) The bar graph showing relative pharyngeal pumping rates of worms with- (bacterial solution, $OD_{600}=10$) and without- food on chip, normalized to animals on standard agar plate with bacteria lawns (control). The pumping rates were averaged of three individual measurements. 103

Figure 4.11: Time-lapse images of GFP signals of PLMs for 19 hours on two different rows after 1hr PLMs-selective illumination (upper) and without illumination (control, lower). The GFP intensity of illuminated PLMs decreases as a function of time, while all PLM signals have no critical changes without illumination. Arrowheads point PLM bodies and asterisks indicate vanished GFP signals on PLM bodies. 104

Figure 4.12: Functional verification of phenotypic changes by selective neuronal ablation. a) Simplified neural circuit from mechanosensation to behavior. The circuit is connected with synapses and gap junctions between individual neurons. b) Recovered worm failed forward locomotion when touched posterior body and c) its PLMs showing no GFP signals when re-imaged after blind behavior-test. In contrast, d) another recovered worm responded immediately when touched posterior body and e) re-imaging confirming its intact GFP signal on PLMs. 106

Figure 5.1: Design comparison of current version of device (optimized for L4 stage and young adult animals) and device for imaging L1 stage animals. Zoom-in view of trapping channels a) in current device and b) in L1 imaging device. c) Side-view of a-a' in b) representing the two-layered channel. 115

SUMMARY

Organisms respond to environmental conditions and modulate their physiological outcomes through the regulation of neuronal activities. How nervous system senses and interprets the environmental inputs at the molecular and cellular level remains poorly understood. Due to relative simplicity and known neuronal connectivity, *C. elegans* has been extensively used for neuroscience research. The use of this model organism has enabled great discoveries in genetic specification and neurodevelopment as developments of advanced reagents such as transcriptional reporters and optogenetic tools. However, conventional manual microscopy limits the application of *C. elegans* to dissect complex regulatory mechanisms due to the time-consuming and qualitative nature of phenotyping animals. In particular, currently it is still difficult to perform the genetic screens for subtle phenotypic changes and parallel selective stimulation in large scale of animals.

The field of neuroscience of *C. elegans* has recently seen microfluidics emerge as a powerful method for precise worm handling and computer-aided automation. However, although the current microsystems for high-throughput and high-resolution imaging of *C. elegans* has superior performance compared to conventional approaches, most of these systems are often too complex and not convenient for non-expert users. Furthermore, the complex fabrication of microdevices results in non-negligible failure rates and low reliability. Another bottleneck in the current approach in addition to microfluidics is the lack of quantitative analytical tools to phenotype animals, e.g. features of fluorescent markers; it is currently difficult for researchers to identify subtle phenotypes.

This thesis seeks to address the critical bottlenecks of current technologies that have slowed the neuroscience research in *C. elegans*. The objective of this research is to enhance the currently developed systems through the design and construction of simple microdevices and quantitative analytical tools for high-throughput phenotyping *C. elegans* to investigate functions of nervous systems. This thesis is divided into three parts: genetic screening using microfluidic device and quantitative analysis, modeling approach to understand the phenotypic changes in putative mutants, and development of new platform and using this platform for neurodegeneration applications.

First, we developed and used the integrated system combining high-throughput microfluidics and quantitative analytical tools to study the genetic regulation of target gene expression. To overcome the limitations of current microdevices, we developed the user-friendly single-layer microfluidics; the device fabrication is not only simple and fast, but also economically favorable and highly reproducible. Additionally, we developed and utilized analytical tools for quantitative phenotyping. We measured the level of target-gene expression and sorted the putative mutants based on an adaptive algorithm. The algorithm was developed to define screening threshold to achieve the balance between maximizing sorting rate and minimizing false-positive rate. We found several putative mutants based on large-scale screens, which would have previously been too labor-intensive to attempt.

Second, we developed a simple mathematical model that includes both deterministic and stochastic elements and describes the regulation of a target gene expression. Using the model developed, we simulated phenotypical space of hypothetical mutants based on parameter alterations. By analyzing the allowable range in the

phenotypical space and comparing to experimental results, we suggested plausible genetic pathways some isolated mutants may affect. This study may be useful in prioritizing phenotypes of interests for sequencing and further characterization.

Lastly, we developed a high-density multichannel device that regularly positions a large number of animals for parallel experimentation. We used this integrated system to study the neurodegenerative process based on selective ablation using an optogenetic tool, KillerRed. The use of this device enabled parallel selective ablation of multiple animals, which would have been taken at least 1 order of magnitude longer. Additionally, this platform efficiently performs the entire process of illumination, culture, imaging, and ease recovery of animals in large scale. Thus, we observed phenotypic and physiological changes of individual animals without transferring animals between each step, which increase the overall throughput of experiments.

In summary, this thesis contributes to the repertoire of microdevices and quantitative analytical tools to perform *C. elegans* neuroscience research by increasing the experimental efficiency and by allowing certain type of experiments to be performed that were not plausible before. We expect that these developments will greatly facilitate a broad range of fundamental, and application studies including aging, neurodegeneration, circuit and behavior.

CHAPTER 1

INTRODUCTION

1.1 *C. elegans* as a model system

1.1.1 General anatomy and physiology

Caenorhabditis elegans (*C. elegans*), small free-living nematode worm, has been used as a powerful experimental model [1]. It is one of the simplest multicellular eukaryotes and its basic anatomy is simple with about 1000 somatic cells. Animal size is very small; the adult worm is about 1 mm in length. This simple organism has two sexes; hermaphrodites, which clone themselves, are predominant, and males include only about 0.05% of the total population. It is easy to maintain and culture *C. elegans* in controlled experimental environments. *C. elegans* lay a large number of eggs and they are grown on agar plates or liquid media feeding with *Escherichia coli*. This nematode has the short lifespan of approximately 2–3 weeks at 20 °C and generation time of approximately 3.5 days. The developmental changes through four larval (L1-L4) stages or alternative dauer stage are well studied [2-4]. In addition, the ability of frozen in *C. elegans* allows long-term storage.

1.1.2 Using *C. elegans* as a model for neuroscience

C. elegans is appealing to neuroscience research. First of all, *C. elegans*' transparent body makes it easy to observe GFP expression *in vivo* using fluorescence microscopy. [5, 6] Second, *C. elegans* has over 19,000 genes and its genome is completely sequenced for the first time in multicellular organisms[7]. Although there are

obviously significant differences between humans and *C. elegans*, approximately 60-70% of their genes have human homologs. Many of the developmental mechanisms identified in *C. elegans* are conserved in more complex animals including humans. Third, *C. elegans* consists of 302 neurons whose network is completely mapped out.[8] Lastly, the genetic manipulation of *C. elegans* is amenable and many mutants are available. As well in most organisms, the published information on *C. elegans* was collected and easily accessed from the web site, WormBase database (www.wormbase.org). *C. elegans* is an excellent model to characterize regulations of gene expression *in vivo* and it serves as a bridge between simple single-cell organism and higher complex animals. Thus, this organism has been broadly used and enabled great discoveries including programmed cell death and RNA interference.[9-12]

1.1.3 Tryptophan hydroxylase (TPH-1) as a linker between environmental perception and physiological phenotype

It has been known that serotonin regulates neural circuits controlling behavior and metabolic phenotypes such as laying eggs and fat accumulation *in C. elegans* [13-15]. In addition, the role of serotonin as a regulator of insulin/IGF-1 and transforming growth factor- β (TGF- β) pathway was identified [14, 16, 17]. Insulin-like pathway plays an important role in modulating aging in *C. elegans* [18-21] and TGF- β is critical for cell growth, embryogenesis, body size and patterning [22, 23]. To synthesize serotonin *in vivo*, tryptophan hydroxylase (TPH-1) enzyme is required [14]. The expression of *tph-1::GFP* fusion gene provides the evidence that *tph-1* is expressed in serotonergic neurons, NSM, ADF, hermaphrodite-specific HSN, male-

specific CP, and occasionally AIM and RIH (Fig. 1) [14, 24]. NSM are secretory neurons and act in an endocrine fashion by affecting the activity of cells at a distance due to free axonal ending extended into the pseudocoelom [25]. ADF, chemosensory neurons, detect environmental signals and influence the perception of the environments in *C. elegans* [26]. Only *tph-1* in ADF neurons response to the temperature and food level and then change its expression level [15, 17]. This expression change of *tph-1* in ADF neurons revealed its function in connecting environments and metabolic pathways including age-regulated pathway in *C. elegans*.

1.1.4 Gene expression profiling

Genome sequencing in the last decade has seen a large technological advance [27]. Phenotypical analysis based on quantitative imaging has become the rate-limiting step in the field of genetics [28]. It is important to monitor specific gene expression levels to identify the specific features and functions in the regulatory network like those related to development. To characterize gene expression in a specific cell or tissue, usually promoter activity is analyzed in transgenic animals carrying *promoter::GFP* reporters [29, 30]. For example, Dupuy *et al.* analyzed genome-wide promoter activity for the complete set of promoters, each driving the expression of GFP through development. Compared to other conventional methods such as DNA microarray, imaging GFP reporters have very high spatial resolution and can reveal differential expression in different cells or tissues. To image a large population of animals, flow-cytometer adapted for nematodes can be used [29], but to characterize expression at single-cell level, fluorescent microscopy is typically employed to generate and collect the expression pattern in *C. elegans*. Although

single-cell resolution microscopy will benefit in this kind of studies, this analysis is time consuming and labor intensive. To reduce experimental time and human intervention for better data quality, high-throughput technology needs to be developed. Previously fluorescent phenotyping has been developed in a qualitative manner, but it is not suitable to identify the subtle phenotype. Quantitative analysis can identify reduction or increase in fluorescent intensity and subtle modification as well as location and timing of appearance of a reporter.

1.1.5 Genetic screening

In general, genetic screening requires a great number of animals from a mutagenized pool to identify the function of genes that are involved in a specific process. Screen in *C. elegans* can be performed in either forward or reverse ways. More standard, forward screen induces random mutations into genomes of worms to eliminate gene functionality. Typically UV irradiation or chemical compound such as ethyl methane sulphonate (EMS) is used as a mutagen to produce random mutations. In particular, EMS is often used because of its ease of use because of its relative efficiency and low toxicity [31]. Once mutated, animals are examined to find phenotype of interested and then sequenced to identify the gene and its function. The reverse genetic method uses interference RNA (RNAi) to stop express target gene and successfully used in *C. elegans* [9]. Compared to forward genetics method, RNAi screen does not affect the gene itself and is relatively simple. However, this method requires genomic information and a large number of plasmids in advance.

For screening applications, in addition to system requirement, another

important element of quantitative screens is the sorting criterion, particularly in image-based ones. It is important to set a balanced criterion to sort putative mutants in screening: too relaxed criterion means large false positive rates and would unnecessarily increase the number of candidates to be scored to confirm positive hits, while a too strict threshold may result in missing mutants. Target mutants are sorted usually based on the changes of certain morphological markers, such as GFP transcriptional reporters. This selection in some scenarios is straightforward, but some changes are too subtle to be characterized even at high magnification. For example, changes in specific location or pattern of GFP expression are easier to be identified rather than changes in expression intensity in a single cell.

1.1.6 Cell ablation using optogenetic tool, KillerRed

Neuroscience often addresses the questions of how neural circuits are specified and functionalized to regulate the physiologies including behavior, learning, and memory in animals.[32, 33] Neuronal and axonal damages are associated with many neurodegenerative diseases including Parkinson's, Alzheimer's, and Huntington's.[34]

One way to investigate the function of a specific neuron is to kill the cell and analyze the phenotypical and physiological changes.[35, 36] To ablate cells, laser ablation technique has been widely used because the operations can be performed in any kind of cellular features within a short period of time. Recently, another optical technique using photosensitizer was introduced to mimic the slow biological degenerative process without expensive laser setup. The genetically-encoded photosensitizer, KillerRed (KR), is activated upon exposure to green light (540-590

nm) and allows the selective ablation by producing excessive reactive oxygen species (ROS) without secondary damage to neighboring cells and tissues.[37-39] It takes about 18-24 hrs after illumination to observe morphological damages of illuminated neurons. To stimulate targets and observe their phenotypic changes in large number of animals, high-throughput stimulation, long-term culturing and imaging are required.

However, commonly used manual handling has limitations to fulfil these requirements in a high-throughput way because of time-consuming sequential manipulation of animals; animals are placed onto agar pad on a slide glass for illumination, moved to bacterial lawn for culture (>24 hrs), transferred back to the microscope slides for observation, and/or recovered from the slides for physiological characterization (e.g. behavior test). In addition to the repetitive and labor-intensive processes, manual handling requires extra immobilization process (e.g. anesthetics), which can affect developmental processes. In addition, manual method makes it difficult to track the time-dependent changes of individual animals due to repeats of labor-intensive processes and anesthetics usage.

1.2 System for neuroscience research using *C. elegans*

1.2.1. Conventional methods for imaging *C. elegans*

Manual microscopy is the most common method to image worms with subcellular resolution [40]. This method uses anesthesia to immobilize *C. elegans*, before they are mounted on a microscope slide. After recording orientation and position of animals, each worm is imaged at multiple focal planes to obtain 3D images with high-resolution. For screening animals of interest, the coverslip is carefully slid off and the animals of

interest are transferred onto a new agar plate. However, this manual handling is labor-intensive and time-consuming, which limits experimental throughput. In addition, used anesthetics may disrupt neuronal signaling and change physiology significantly [41, 42].

To handle small organisms, the only existing commercial high-throughput system with automation is complex object parametric analyzer and sorter (COPAS) from Union Biometrica. COPAS generates fluorescent expression patterns and sort animals based on this optical analysis upto ~100 animals/sec. This system is successfully used in large-scale quantitative analysis of GFP expression along the anterior-posterior axis of *C. elegans* [29]. However, this Biosorter provides only 1D resolution with tissue-level, which limits its application when single-cell and subcellular resolution is required. For instance, for my applications, COPAS will not be able to identify two ADF neurons, and moreover 1D-based intensity calculation may not correctly measure the 3D neuronal expression level. Therefore, new methods have to be developed to accurately quantify the gene-expression level at single-cell imaging resolution.

1.2.2 Microfluidics for gene-expression profiling in *C. elegans*

Microfluidics refers to techniques to manipulate small amount of liquid inside of microstructures with dimensions of a few to hundreds of microns. Since the 1980s, microfluidics has been applied to various technologies due to several advantages in miniaturization [43, 44]. Flow in microsystem is usually laminar because flow in micron-channel size has low Reynolds number, which is predictable and thus easy to manipulate chemical and biological samples in flow. Another benefit of microfluidics is integration to perform multiple functions, which can enable the parallel processing of samples to

save analysis time. In the last few years, a few microsystems have been developed to image *C. elegans* [45-51]. The *C. elegans*' small size and its ability to live in liquid media are adequate for microfluidic application [28]. From the microfluidic development with sophisticated its design, quality and speed of data analysis, biologists can tackle a large number of complex problems.

Recently, automated microsystem for high-throughput and high-resolution phenotyping and sorting of *C. elegans* has been developed in our group [50]. This microfluidic device is fabricated with multilayer soft lithography [52] and can be combine with a microscopy setup with software control. During operation, each *C. elegans* is automatically loaded into a single small channel and released/sorted after imaging and phenotyping. This device uses partially-closed on-chip valve as a passive loading regulator to allow only one worm loading in the imaging zone. Once worm are loaded into the imaging zone, they are automatically positioned in the identical position in the chip, which minimize the image processing time. For high-resolution imaging, worm is reversibly immobilized by gentle cooling (~ 4 °C). This microsystem minimizes not only enables high-throughput screening but also minimizes human intervention to achieve reliable quantitative analysis with high-resolution imaging. Despite its superior ability, the small channel fitting to worm size has high likelihood of clogging and limits loading of animals with size variations resulted from mutagenesis. In addition, cooling is sensitive to the membrane thickness and complicated to control heat transfer. Another simplified microchip was developed in our group [51]. Since this device does not completely immobilize nematodes, the application is limited in imaging with bright marker with lower magnification.

Other developed microfluidic systems use trapping channel which is adjustable to the worm size [48, 49]. This wide channel minimizes the possibility of clogging and allows immobilization of worms at various sizes due to difference developmental stages or mutations. However, worm position in the imaging zone is not constant, which requires the travel of the motorized stage to locate the worm of interest and thus increase the processing time. These systems are also difficult to automate because the rate of worm loading in these systems is not constant and hard to be regulated. Because of the manual control of the system, the throughput in this system is low. Moreover, these devices use membrane deflection to immobilize the worm under the valve, but this squeezing may change the phenotype of worms.

1.3 Thesis objective

The purpose of this thesis is to advance technologies for phenotyping *C. elegans* to investigate the function of nervous systems efficiently and quantitatively. The specific research objectives of this thesis are:

(1) The development of the simple and robust single-layer microfluidic device for research in *C. elegans* neuroscience: specifically, (1-1) a microdevice for imaging and sorting *C. elegans* in a high throughput manner in Chapter 2, and (1-2) a high-density multichannel device for parallel stimulating and long-term monitoring animals in Chapter 4.

(2) The design and use of the quantitative analytical tool for characterizing targets of interests: (2-1) phenotyping subtle changes in fluorescent intensities, (2-2) isolating targets with minimizing efforts in following confirmation and sequencing steps in

Chapter 2, and (2-3) interpreting phenotypic changes in mutations in specific pathways to understand how target gene expression is regulated by genetic and environmental (temperature) factors in Chapter 3.

(3) Studies of the genetic regulation on target-gene expression by performing the screening in Chapter 2, and characterization of ROS-dependent degenerative process based on selective ablation using an optogenetic tool in Chapter 4. Here, we demonstrated the abilities of the platform for specific studies, but, it would be valuable for any study based on imaging, stimulating, and culturing a large number of animals in neuroscience of *C. elegans*.

CHAPTER 2

DEVELOPMENT OF HIGH-THROUGHPUT SYSTEM FOR QUANTITATIVE SCREENING

Much of the work presented in this chapter was originally published in *Integrative Biology*: Lee *et al.*, “Quantitative screening of genes regulating tryptophan hydroxylase transcription in *C. elegans* using microfluidics and adaptive algorithm”, *Integrative Biology*, 2013, 5, 372-380, and Chung, Lee and Lu, “Multiplex pressure measurement in microsystems using volume displacement of particle suspensions”, *Lab chip*, 2009, 9, 3345-3353. This work is performed in collaboration with Matthew Crane and Kwanghun Chung in Dr. Lu’s group.

2.1 Overview

Forward genetic screen via mutagenesis is a powerful method for identifying regulatory factors in target pathways in model organisms such as the soil-dwelling free-living nematode *Caenorhabditis elegans* (*C. elegans*). Currently manual microscopy is the standard technique for conducting such screens; however, it is labor-intensive and time-consuming because screening requires imaging thousands of animals. Recently microfluidic chips have been developed to increase the throughput of some of such experiments; nonetheless, most of these chips are multilayer devices and complicated to fabricate and therefore prone to failure during fabrication and operation. In addition, most sorting decisions are made manually and the criteria used for sorting are subjective. To overcome these limitations, we developed a simple

single-layer microfluidic device and an adaptive algorithm to make sorting decisions (Fig. 2.1). The one-layer device greatly improves the reliability, while the quantitative analysis with adaptive algorithm allows for the identification of mutations that generate subtle changes in expression, which would have been hard to be detected by eye. The screening criterion is set based on the mutagenized population, not separate control populations measured prior to actual screening experiments, to account for stochasticity and day-to-day variations of gene expression in mutagenized worms. Moreover, during each experiment, the threshold is constantly updated to reflect the balance between maximizing sorting rate and minimizing false-positive rate. Using this system, we screened for mutants that have altered expression level of tryptophan hydroxylase, a key enzyme for serotonin synthesis in a CaMKII gain-of-function background. We found several putative mutants in this screen. Furthermore, this microfluidic system and quantitative analysis can be easily adapted to study other pathways in *C. elegans*.

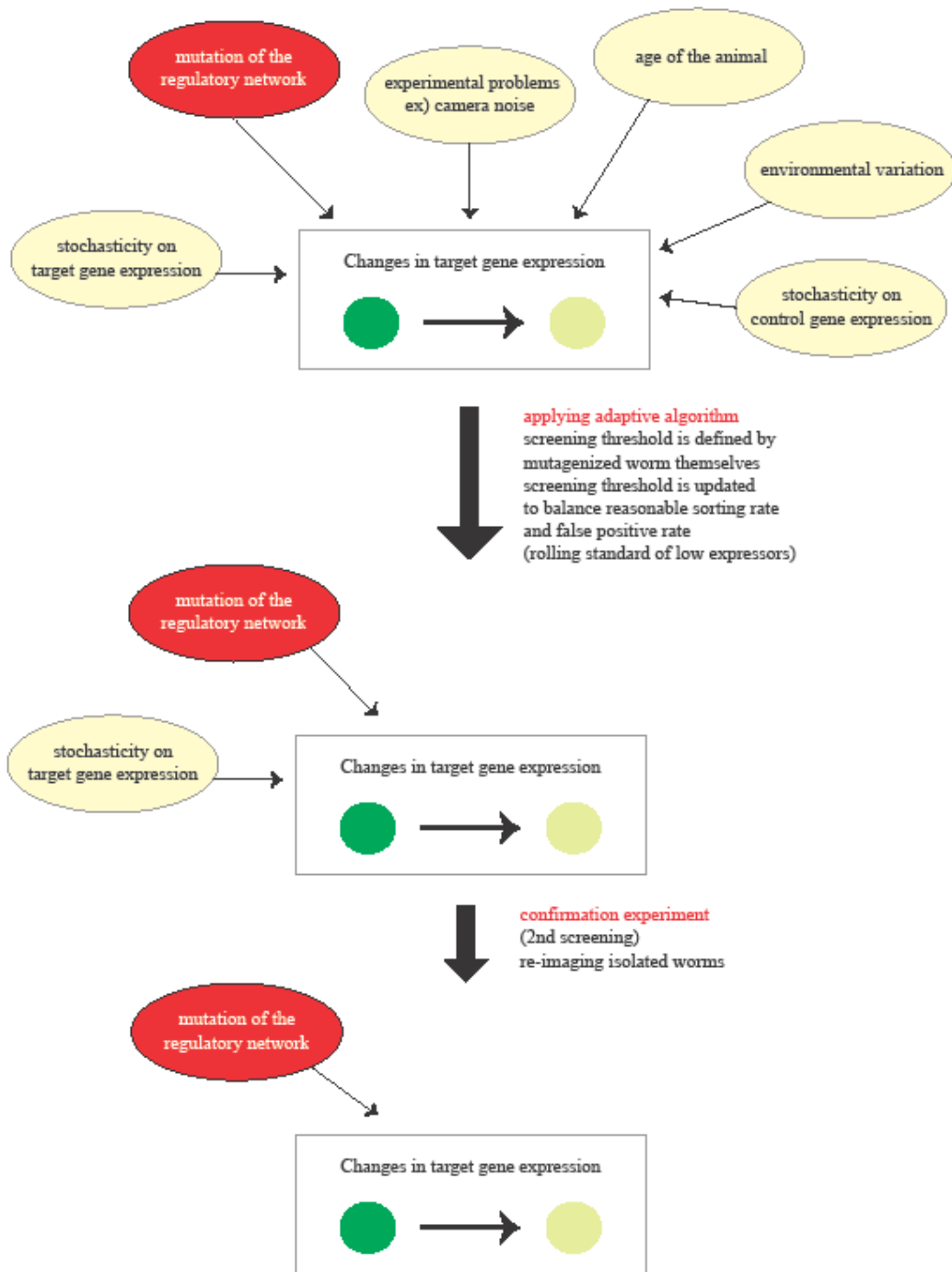


Figure 2.1 Schematics of screening strategy based on adaptive algorithm

2.2 Motivation and limitations of current microfluidic devices

Recent development of microfluidic systems has increased the throughput of imaging experiments in high resolution.[45, 47, 50, 51, 53, 54] For example, Chung *et al.* reported automated microfluidic system with a sorting speed of 150 - 900 worms/hr depending on the magnification used and complexity of the screens.[50] This system showed the ability to perform screens based on cellular and subcellular phenotypes. Some studies also reported the ability to perform laser ablations and sort the animals using microfluidic devices.[49, 55, 56] However, most devices require a design with multiple layers, usually fluid and control layers, and thus the fabrication is complex, especially for non-expert end-users.

There are some single-layer devices developed for *C. elegans*.[45, 47, 54, 57, 58] Hulme *et al.* developed the array device to trap and image *C. elegans*, which is simple to make and easy to operate.[47, 57] However, valve control to load and release worms cannot be automated in this device and thus it is not suitable for high-throughput imaging and sorting.[59, 60] Additionally, Chronis *et al.* reported the single-layer device to image neuronal and behavioral responses in *C. elegans*.[45, 54] This device is designed to record responses from target neurons to odors, and a single outlet, thus not applicable to screening applications.

2.3 High-throughput one-layer microfluidic device for a robust and reliable performance

In order to perform the screen in a high-throughput manner, we developed a simple single-layer microfluidic device that can be operated robustly over long

periods of time. This device has two outlets, and has the flow, control and cooling channels in the same layer (Fig. 2.2). Most microfluidic methods for imaging and sorting *C. elegans* use multilayer soft lithography to create complex microfluidic control components.[50, 51, 53] Multilayer soft lithography is a typical fabrication method where layers of patterned elastomeric are aligned, stacked and bonded for three-dimensional (3D) microstructures,[52, 61] and enables completely closed valves.[50] In comparison, our device uses partially closed side-valves that still allows fluid flow but stops the animals from passing. This single-layer design minimizes the complexity of the system. In the imaging zone, this small space remaining between the valves fits the worm's head well and helps to position each worm in an identical location. Moreover, the fabrication process does not require any alignment process, and thus it enables fast fabrication with dramatically lowered failure rate and higher reliability than its multilayer counterpart (Tab. 2.1). These advantages allow the device to be easily replicated by users, especially by non-experts of microfluidics.

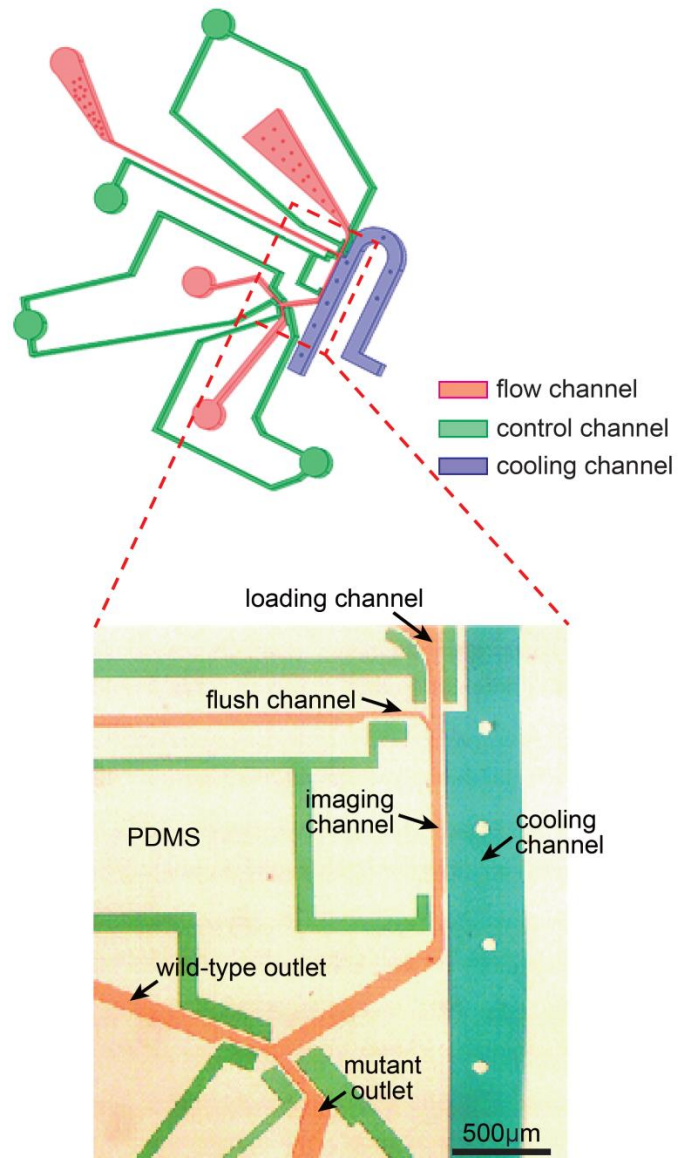


Figure 2.2 3D image of single-layer device (top) and optical micrograph of the imaging zone in a microdevice (bottom). The channels were filled with color dye to visualize features: blue, cooling channel; green, control valves; and red, sample flow channel.

Table 2.1 Comparison between single-layer and double-layer devices.

	Two-layer device	Single-layer device
Alignment	Required	Not required
Failure rate	High	Low
Reliability	Low	High
Fabrication time	Long	Short
Equipment cost	~\$10k	<\$1k
Device to device variation	High	None
Complete sealing	Possible	Impossible (not required for some applications)

2.3.1 Device fabrication

Soft lithography was used to fabricate all single-layer devices in polydimethylsiloxane (PDMS) (Dow Corning Sylgard 184, Midland, MI).[62] To make the masters, the conventional UV photolithographic processes were used to transfer features on transparency. The 50 μm -thick mold was fabricated using SU-8 2025 (Microchem) and the wafer surface was treated with tridecafluoro 1,1,2,2-tetrahydrooctyl-1-trichlorosilane vapor (United Chemical Technologies, Inc, Bristol, PA) to prevent the PDMS from adhering to the master. On top of the mold, the first layer (~1 mm; part A and B in a 20:1 ratio) was partially cured at 70 $^{\circ}\text{C}$ for 10 min. Then, for mechanical integrity, the second layer (~5 mm; 10:1) was poured on the first layer and cured at 70 $^{\circ}\text{C}$ for 2 hr. Finally, the whole PDMS layer was peeled off, cut into shape,

punched for holes, and bonded onto a cover glass for complete devices. The entire procedure is described in Fig. 2.3.

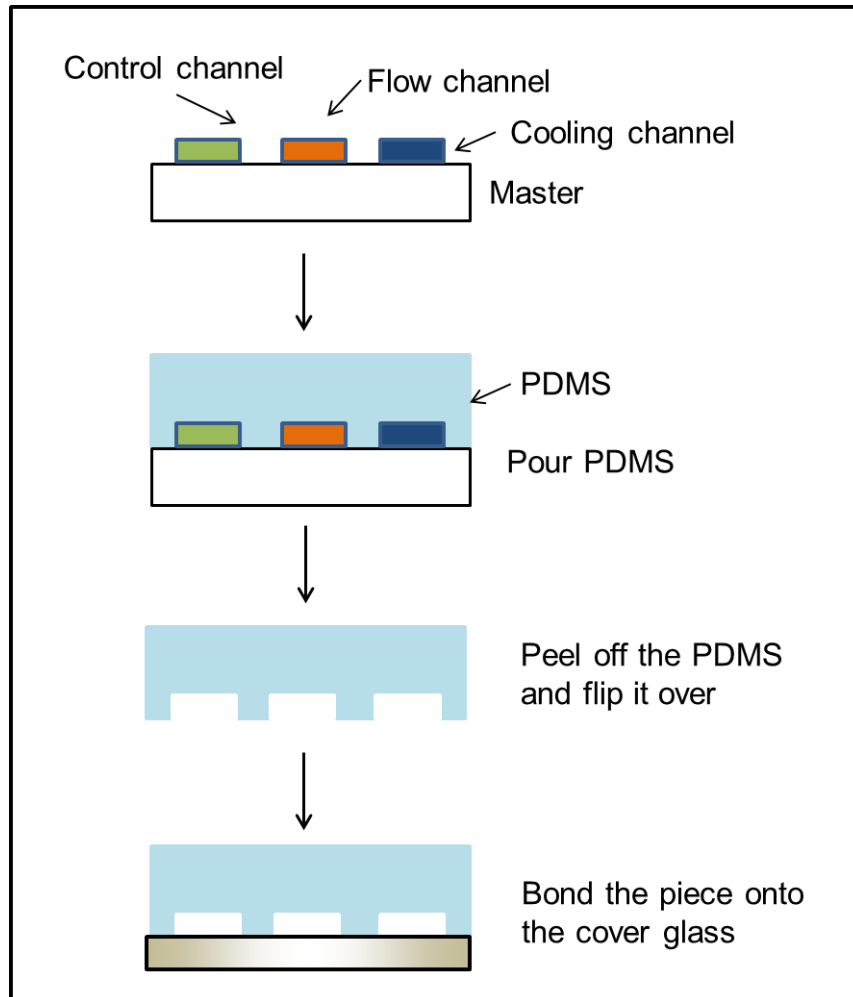


Figure 2.3 The fabrication process of the single-layer microchip

2.3.2 *C. elegans* culture, sample preparation, and isolation of putative double mutants

Strains of *C. elegans* used include GR1333 [*yzIs71(Ptph-1::gfp; rol-6(d))*], and mutant ZC5 [*unc-43(n498); yzIs71(tph-1::gfp; rol-6(d))*]. All worms were fed with *E.*

coli OP50 and grown according to standard protocols at 20 °C or 25 °C.[63] For each experiment, age-synchronized L4 or adult worms were suspended in M9 solution containing 0.02 wt% Triton X100 for imaging. To perform screening for factors in the CaMKII-mediated regulation of *tph-1*, animals that express an integrated reporter *Ptph-1::gfp* in the *unc-43(gf)* mutant background were mutagenized (P0 generation) using ethylmethane sulfonate (EMS) with a standard mutagenesis protocol.¹ Approximately 4,000 adult F2 progeny cultured at 20 °C were scored for reduction of TPH-1::GFP in the ADF neurons.

2.3.3 Device operation

Device operation is similar to previous work.[50, 51] Worms were loaded by pressure-driven flow and reliably positioned in the imaging zone by controlling the side valves. Once worms were loaded, they were immediately cooled because of the side cooling channel, then remain immobilized for <5 sec during the imaging process.[50] To cool down only worms in the imaging zone, the cooling channel is designed to be close to the imaging channel; in contrast, there is enough distance to other parts of devices such as the input chamber and outlets so that their temperatures are not affected by the presence of the cooling channel. After being completely immobilized, the z-stack (2- μ m steps) images of worms were obtained at 20X objective using an EM CCD camera (Hamamatsu C9100-13). Then, images were quantified for their expression level of a target gene (in this case *Ptph-1::gfp*). Based on the phenotype of the animal, it would be sorted as either mutant of interest (i.e., double mutant whose *tph-1* expression level is lower than that of *unc-43(gf)* in here),

or waste. This unloading process is very efficient and fast because of the use of the flushing channel.[54] This sequence of operation is automated by a program developed in MATLAB. This yields a high throughput (up to 500 worms/hr, which is comparable with other microfluidic devices previously developed for imaging *C. elegans*[50, 51] and 1-2 orders of magnitude higher than conventional microscopy), and facilitates the screening performance for the regulation of a target gene. In general, the system can be easily integrated for any screening or imaging a large number of *C. elegans*.

2.3.4 Numerical model for characterizing the deformation of the membrane for valve operation

To aid the design of the microdevices, three-dimensional deformation model of a thin PDMS membrane was developed using a structural mechanics module of the finite element modeling software, COMSOL (Stockholm, Sweden). The membrane of valve simplified to a disk with 80 mm radius and 15-30 mm thickness. In the simulation, the value of Poisson ratio was ~ 0.5 and the Young's modulus was chosen to be 0.1 or 1 MPa; both values matched well with those in the literature.[51, 64] The side surface of the membrane was assumed to have either no displacement in any direction or 5 μm in all directions, and the applied pressure was 0–10 psi, uniformly distributed along the bottom surface of the membrane. Fig. 2.4 shows dome-like deformations of the membranes when two different pressures are applied; as expected, lower pressure produces less deformation (front left membrane). At each pressure, the deformation of the membrane (Fig. 2.4a) was quantified by reading the normalized

cross-sectional diameter of the deformed membrane (defined as cross-sectional diameter of the deformed membrane divided by the original diameter) at a particular vertical position, 24 μm above the membrane's resting position (Fig. 2.4 b, c).

The membrane deformability is largely determined by two parameters: Young's modulus and the dimensions of the membrane.[64-67] Experimentally, Young's modulus of PDMS can be varied easily by changing the mixing ratio of prepolymer to curing agent, curing temperature, and curing time.[64, 65] We optimize mixing ratio to part A and B in a 20:1 ratio. In addition to the mechanical properties of the membrane material, we examined the effect of membrane thickness on the membrane deformability. The thinner membrane is more flexible and easy to deform. To maximize the flexibility, we need to minimize PDMS membrane thickness between control and flow channel. To maintain the membrane integrity, here we designed membrane thickness around 25-30 μm . In addition, the aspect ratio of channel height and contacting width is critical to determine the membrane deformability. Thus, we designed the aspect ratio as always larger than 1:2 for optimal operation.

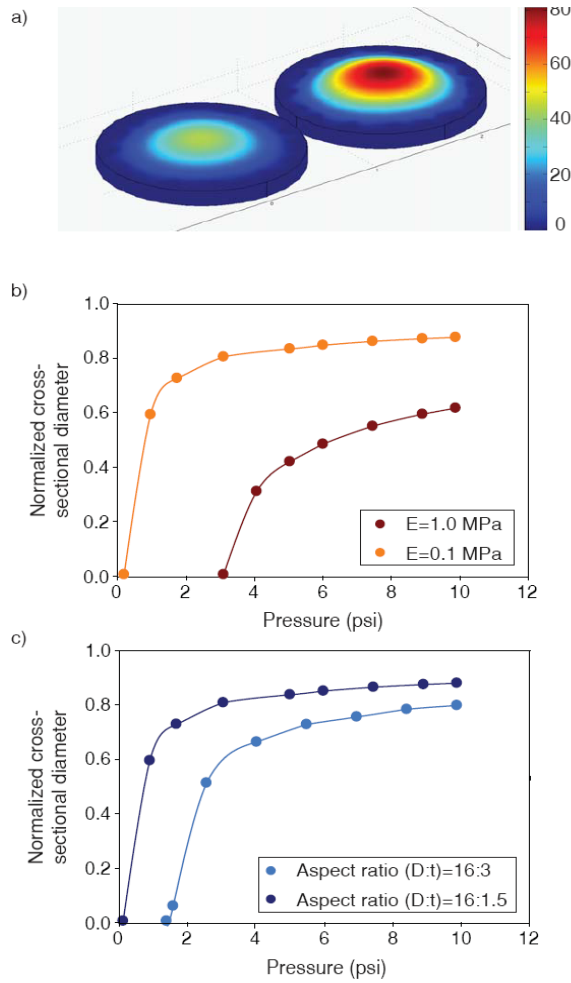


Figure 2.4 Numerical models of membrane deformation. (a) The deformation of the disk-shaped membrane is a strong function of pressure. At a low pressure (5 psi, left/front), the membrane has a smaller deformation, as compared to a higher pressure (10 psi, right/back). Color scale represents the vertical displacement of the membrane in microns (μm). (b) and (c), The normalized cross-sectional diameter of the dome-like deformed membrane also depends on membrane properties, including the Young's modulus (b) and aspect ratio as defined by ratio of diameter to thickness (c). The solid squares and circles represent data for sensors with the membrane edge anchored. The hollow squares and circles are data for sensors with $5 \mu\text{m}$ edge displacement in the membrane.

2.4 Quantitative Screen of target of interest

Using the system developed here, we performed the screening to identify genetic factors that regulate *tph-1* expression to understand environmental responsive physiologies or serotonin-deficient diseases. Currently it is known that stress, such as high temperature, stimulates calcium signaling pathway including CaMKII encoded by *unc-43*, in ADFL/R and up-regulates *tph-1* expression level (Fig. 2.5).[68, 69] To look for additional genetic players in the *unc-43*-dependent *tph-1* regulation pathway, we performed a forward genetic screen with mutagenized worms having *unc-43(gf)* background. Double mutants showing different phenotype from *unc-43(gf)*, i.e., low expression of *tph-1*, were sorted for further analysis. In other words, screening target has similar *Ptph-1::gfp* expression phenotype as wild-type.

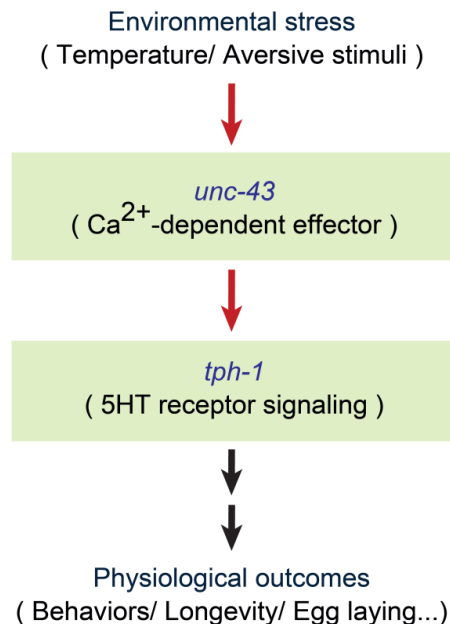


Figure 2.5 Simplified mechanism for CaMKII-dependent regulation of *tph-1* in ADF neurons

2.4.1 Necessity of quantitative analysis

We need to use quantitative analysis to define the expression level of *tph-1* to reduce the false-positive rate and post-processing such as re-imaging the selected putative mutants as population. Previously some genetic screens for *tph-1* regulatory factors in ADFL/R were performed using a dissecting microscope based on its relative intensity.[68, 70] From these previous screens, several genetic regulators were identified. However, generally, qualitative screens are low throughput because identifying subtle differences of *tph-1* expression in each worm is difficult and it introduces significant false positive rates. For example, by comparing Fig. 2.6 b/c to Fig. 2.6 d/e, it is easy to distinguish between strong and weak *tph-1* expressions. Also, it may be possible to compare the relative expression levels of *tph-1* among worms having low expressions in Fig. 2.6 b or c. However, from a single image (as during a screen in real time), it is not reliable to define a target whose expression level is lower than the threshold of difference. Thus, we can conclude that quantitative imaging is necessary and effective to find genetic regulators of *tph-1*.

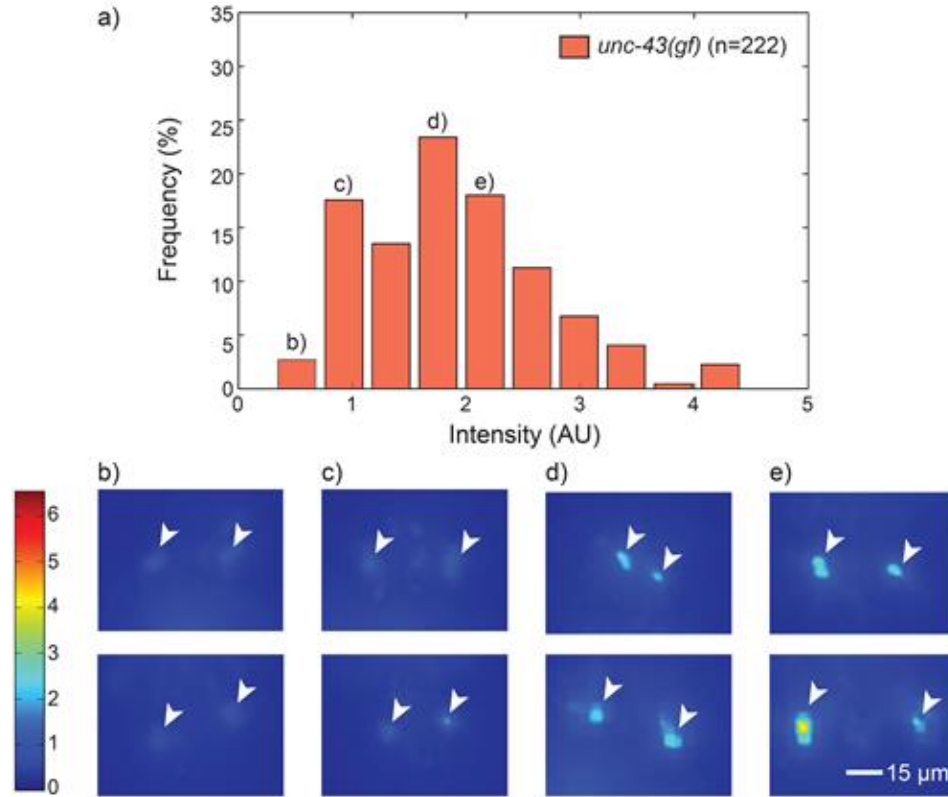


Figure 2.6 Stochasticity in gene expressions in a genetically identical population. (a) Probability histogram of *tph-1* expression levels in single mutant (*unc-43*). The n value represents number of worms imaged. (b-e) Representative images of *tph-1* expressions in ADF neurons in *unc-43(gf)*, which correlate with each quantified bar in histogram (a). All fluorescent images are revised as a heat map for clarity. The color bar on the left represents the average intensity of target neurons, ADFL/R, which correlates with the expression levels of *tph-1*.

2.4.2 Image analysis

To quantify the GFP intensity levels, we used software code developed in MATLAB® to flatten *z*-stack by computing the maximum projection of each stack (Fig.

2.7). From maximum-projection images, we selected the region of interest and the software automatically calculated the average intensity of target neurons with the following procedure: (1) nine pixels enclosing the center of each neuron were automatically selected, (2) their intensities were summed, (3) the intensities of background where TPH-1::GFP were not expressed were subtracted, And (4) the intensities of the two ADF neurons were averaged. This quantitative analysis is fast and simple to use, and can be easily translated to analyze any other neuron intensities.

As a proof of validation, we compared our method to another method. In Fig. 2.8, we compared expression levels of *tph-1* in various targets quantified by our analysis (method 1) to another method (method 2). Method 2 uses larger area (5041 pixels) that includes both ADF L/R neurons in a single ROI and background intensities (which are) defined by k-means clustering. We observed the good correlation which means our method is reasonable to determine the levels of target-gene expression especially for relative comparison of high and low expression.

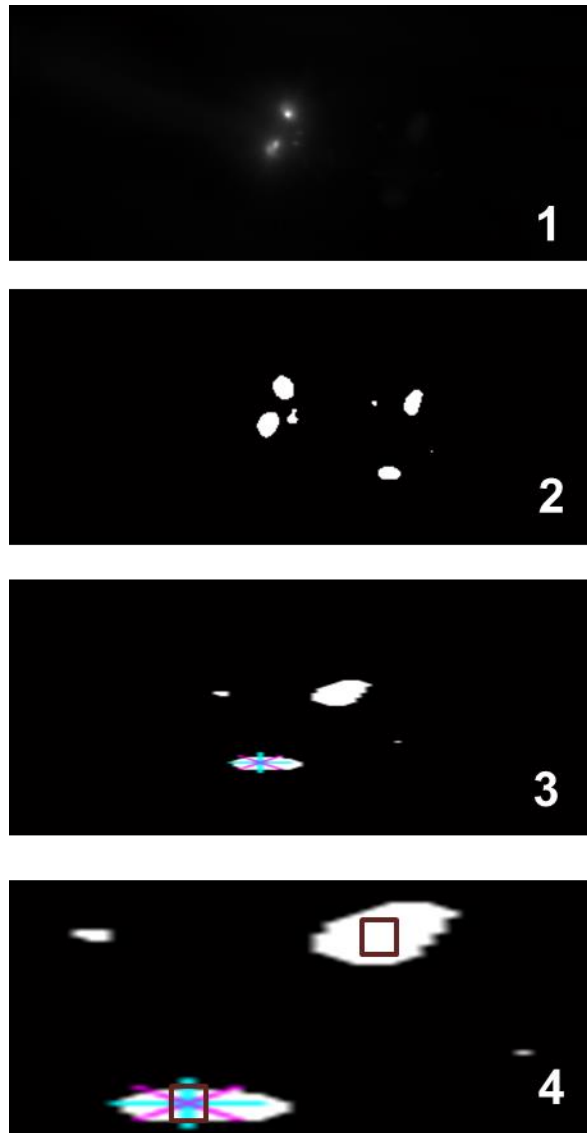


Figure 2.7 Quantitative analysis for expression levels of *tph-1* in ADF neurons with 1) Flattening *z*-stack images, 2) Thresholding images for ADF neurons identification, 3) Localization of neuron centers, and 4) Summing and averaging all pixel intensities within a define ROI.

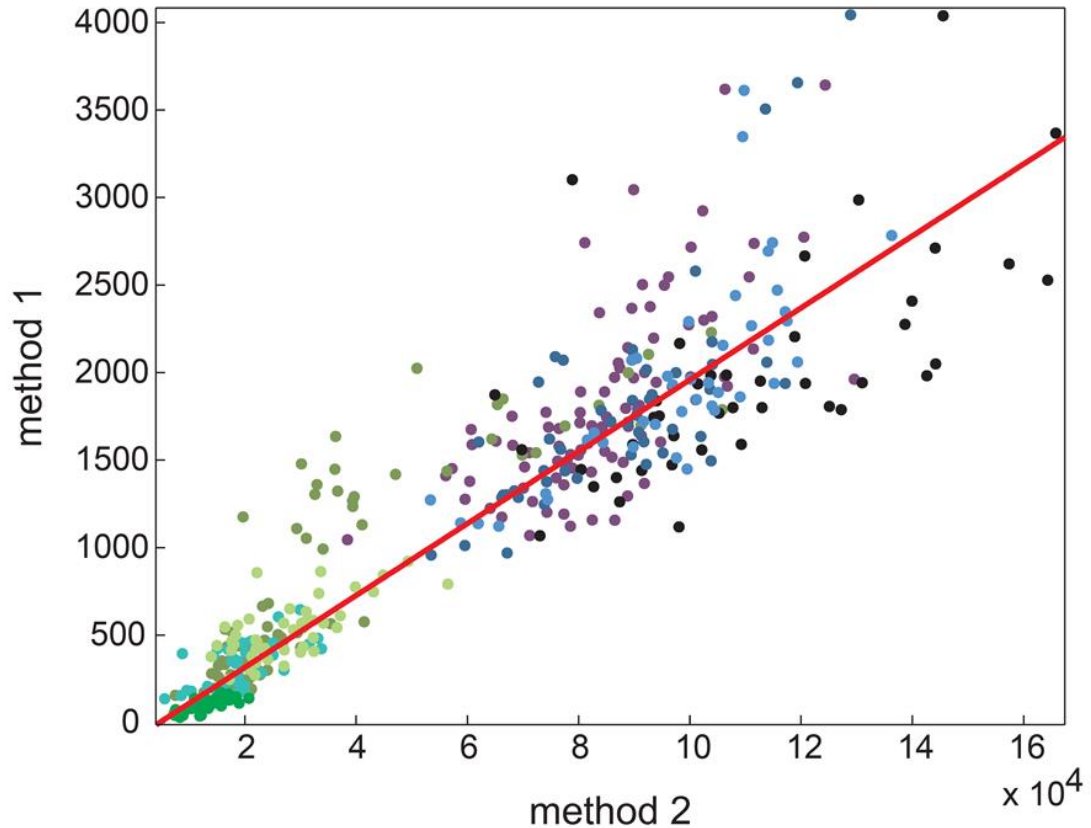


Figure 2.8 Comparison of two quantitative analyses. Various targets (ADF and NSM neurons in wild-type and mutants at either 20 °C or 25 °C) are represented in different color. Red fitting curve shows a linear correlation with $R^2=0.8449$.

2.5 Challenges of this screening

2.5.1 Stochastic effects

There are several challenges in performing this screen. The first, but toughest, challenge of this screening is the stochastic effects on gene expression levels. To define the screening criterion for target selection, we imaged wild-type and *unc-43(gf)* worms having *Ptph-1::gfp* cultured at 20 °C. As seen in the histogram in Fig. 2.9, the average expression of *tph-1* is lower in wild-type and higher in *unc-43(gf)*; however, because the

histograms overlap significantly, it is virtually impossible to pinpoint the genetic identity of individual worms and to have a threshold criterion to distinguish the two genotypes (Fig. 2.9, and Fig. 2.10). Any pre-determined threshold to sort targets would result in an appreciable false positive rate (Fig. 2.10, Fig. 2.11 and Tab 2.2). Practically, we needed to set a relatively low intensity value as a screening threshold instead of performing control experiment to compare wild-type and *unc-43(gf)*.

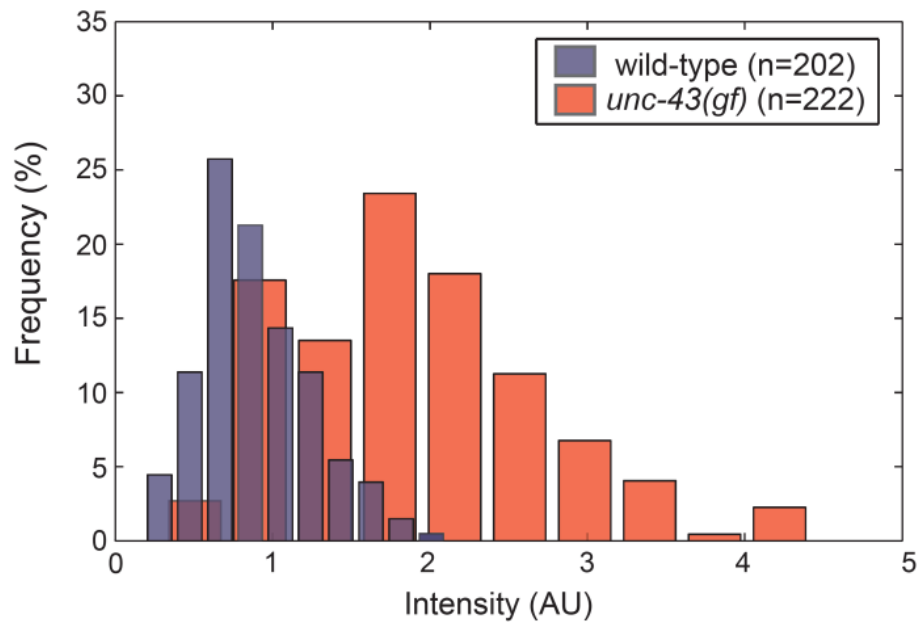


Figure 2.9 Probability histogram of *tph-1* expression levels in between wild-type and single mutant (*unc-43(gf)*).

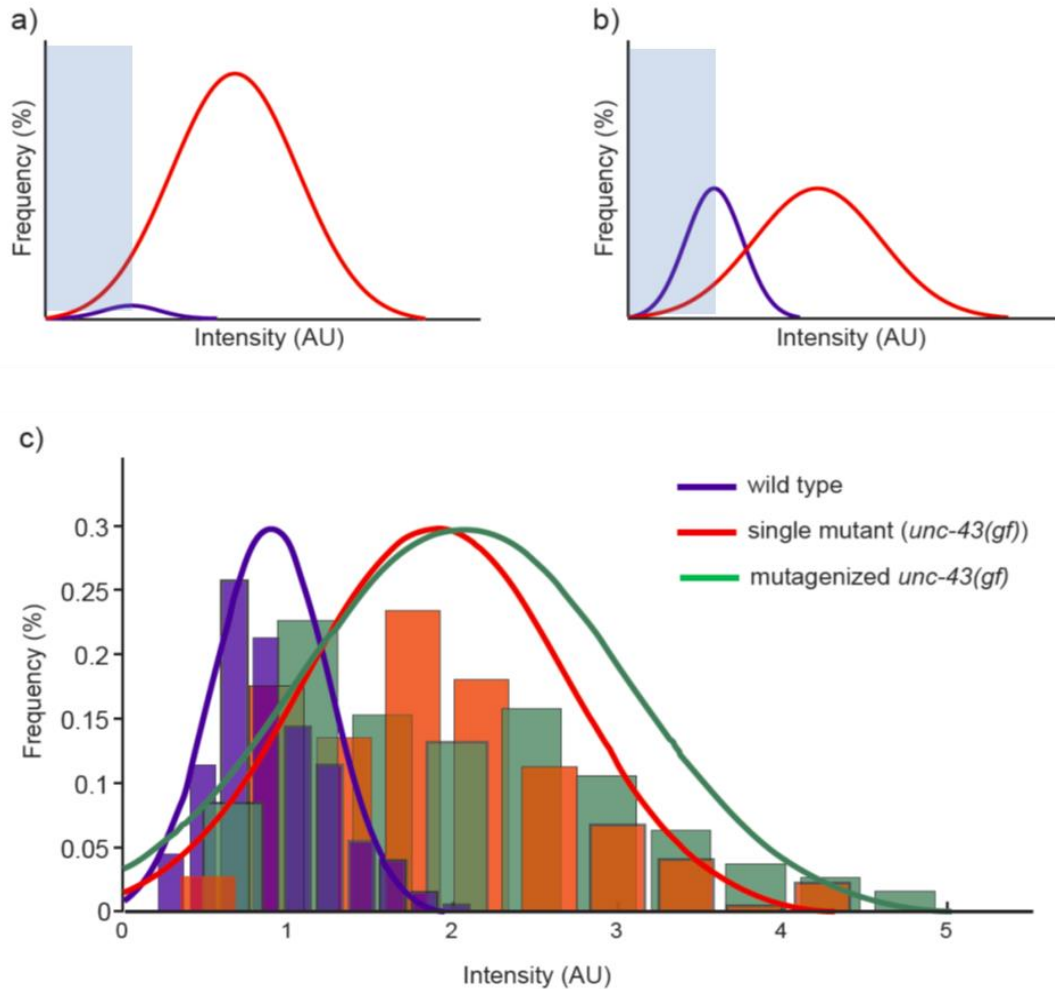


Figure 2.10 a), b) Occurrences of true positives (blue curve) among all sorted positives (blue shade) depend on the occurrences of the desired population among all animals. c) Overlaying the wild-type population, the *unc-43 (gf)* population, and the mutagenized population expression profiles. This demonstrates that the expression profile of the mutagenized population, which contains desired double mutants, is shifted from the *unc-43 (gf)* single mutants as expected. This also demonstrates that there are significant overlaps among the three populations such that any sorted mutants will need to be verified in secondary clonal imaging to be sure that they are true double mutants, rather than single mutants that stochastically show low expressions.

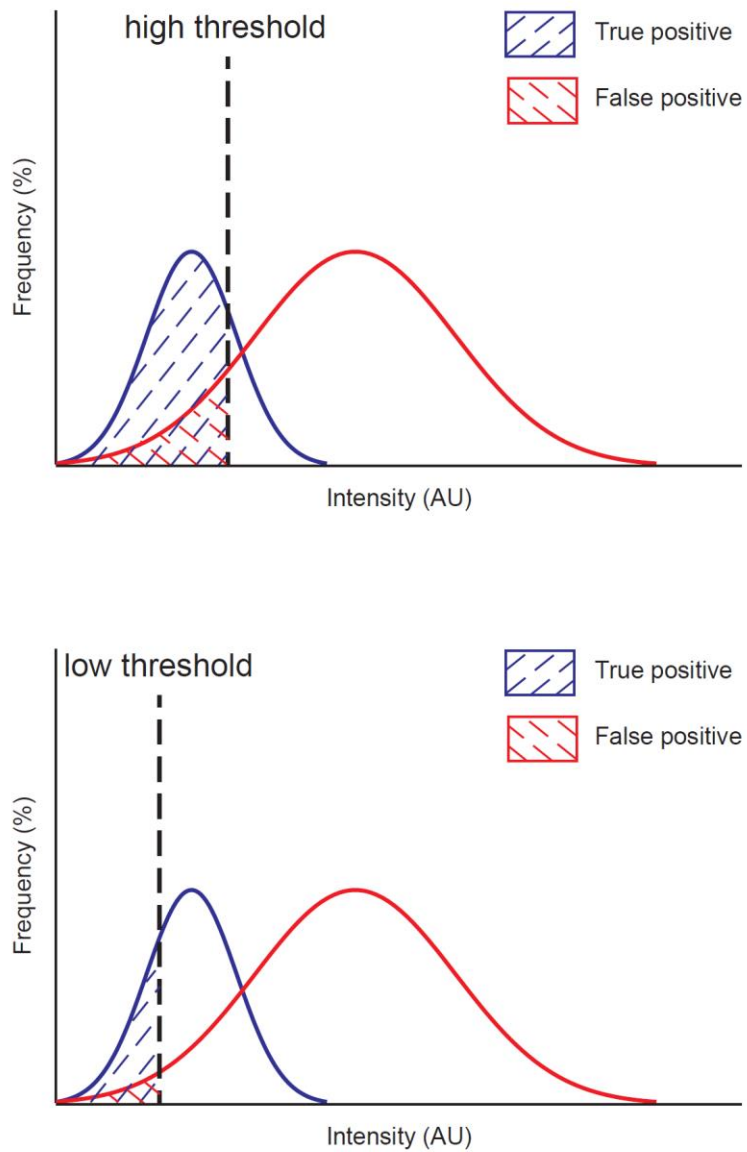


Figure 2.11 Applying different thresholds to the same mixed populations will result in either higher chance to find true positives but at a cost of higher false positives, or smaller false positive rates but at a cost of possibility of missing some true positives.

Table 2.2 Characterization of the sorting algorithm using wild-type (as a surrogate of the double mutant) and *unc-43 (gf)* mutants. Mixing different percentages of WT in *unc-43 (gf)* and choosing different threshold give different levels of enrichment. The false positives are a result of the stochasticity in gene expressions (as illustrated in previous figures), rather than a result of the algorithm. In the actual screen, it is difficult to know what the true occurrence of double mutants are; we arbitrarily chose 2% as screening threshold, but verified that 43 of all the mutants selected are true mutants with a secondary clonal expression profiling (see text and Fig. 2.1, Fig. 2.10, Fig. 2.12).

	Mix of 5% WT and 95% <i>unc-43 (gf)</i>		Mix of 10% WT and 90% <i>unc-43 (gf)</i>		Mix of 50% WT and 50% <i>unc-43 (gf)</i>	
	2% selection	5% selection	2% selection	5% selection	2% selection	5% selection
True positives (n)	1	4	4	8	7	13
False positives (n)	3	5	2	4	0	1
Enrichment (%)	530	941	710	710	200	186

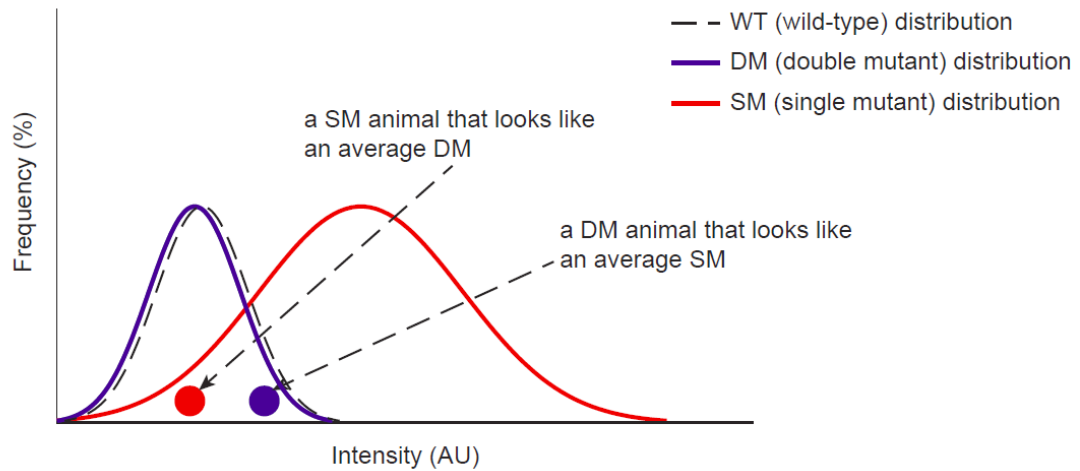


Figure 2.12 Illustration of the stochastic effect of gene expression resulting in overlaps in the expression profiles of isogenic populations. Because of this effect, wild-type or double mutant animals may have a higher expression than single mutant animals, and this effect results in an ultimate limit of enrichment for separations (depending on the size of the subpopulations).

Furthermore, the putative mutant animals that we selected during the screen might have a fluorescent intensity that is above or below the average for the genotype, i.e. they may not represent the population average. Therefore it is very likely that half of the animals isolated are actually false positives even if we follow a stringent selection criterion (Fig. 2.11). Thus, after the first round of screen, we need to re-image the selected putative mutants as populations and confirm the population average is indeed below the *unc-43(gf)* expression. This re-screen is very time consuming since populations would have to be reimaged; to minimize the workload, it is critical to minimize the false positive rate.

2.5.2 Day-to-day variation

Lastly, we need to compensate for the day-to-day variation. First, noises from equipment could interfere with accurate measurement of target GFP intensity. These external noises can be tuned by control bead measurement but additional preparation steps and measurement are required. Furthermore, the gene expression itself may be variable due to certain environmental fluctuations such as culture temperature and bacterial food conditions. Moreover, the worm age affects the expression level of the target gene and age synchronization is often not perfect. For instance, two wild-type cultures at the same conditions for the same period time show large difference in *tph-1* expression, despite negligible external equipment noises, which has been confirmed with control bead measurement (Fig. 2.13). In the case of *unc-43(gf)*, two cumulative distribution functions are similar but not identical, which is enough to affect the screening performance because mutant selection is very sensitive to the intensity. Thus, to look for mutants with subtle quantitative changes, a simple threshold of GFP intensity is insufficient to generate an acceptable small number of false positives.

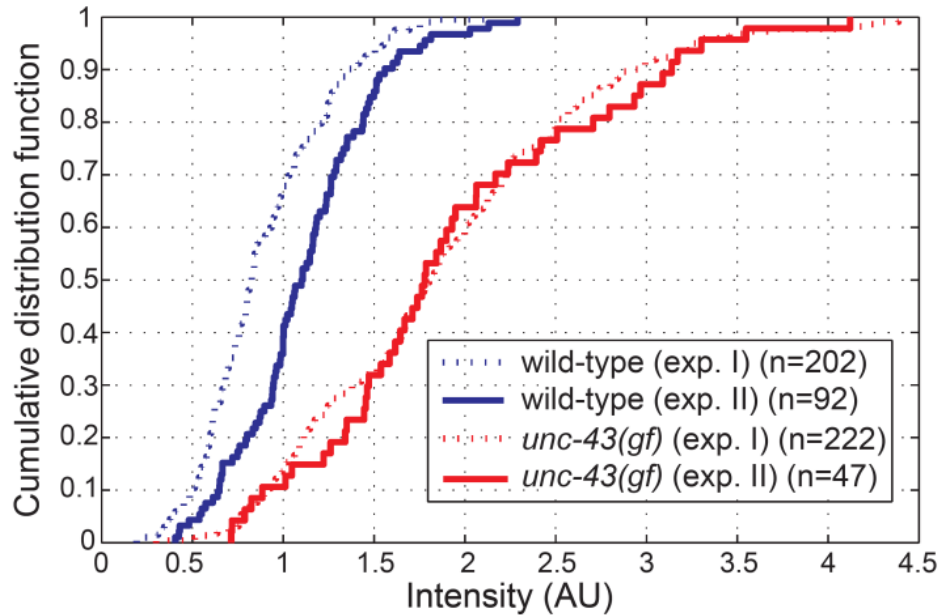


Figure 2.13 Empirical cumulative distribution functions of *tph-1* expression for a different set of worms, which illustrate day-to-day variations. Then value represents number of worms imaged.

2.6 Screening with adaptive algorithm

2.6.1 Use of an adaptive algorithm for sorting mutants

Since a simple threshold based on GFP intensity is not sufficient to select putative mutants due to fluctuations in gene expressions or instrumental noise, we used an adaptive algorithm for sorting mutants. In the adaptive algorithm, the screening threshold was defined and updated by values of mutagenized worms themselves, not by the comparison of wild-type and *unc-43(gf)* (Fig. 2.14 and 2.15). This selection based on rolling minimum intensities is advantageous because no positive or negative controls are

required before the start of the screen, and therefore insensitive to the many variations discussed before.

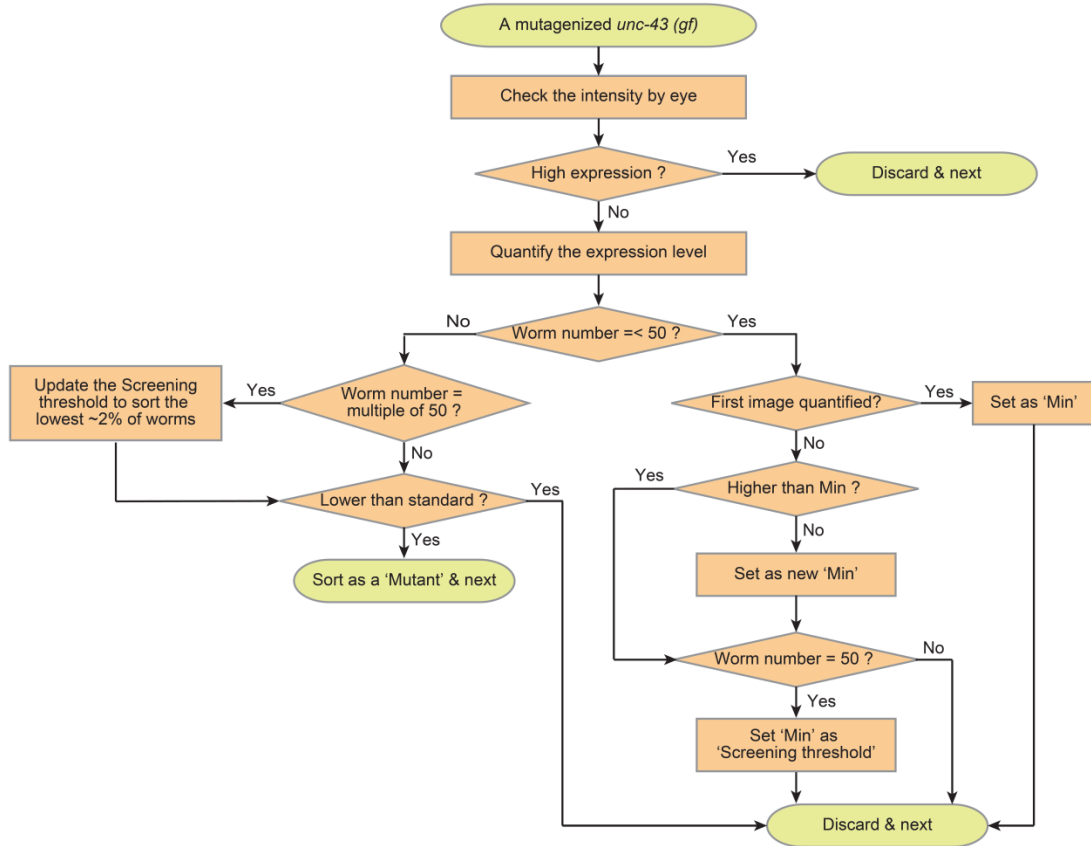


Figure 2.14 Schematics of adaptive screening algorithm for a single worm. Quantitative analysis is only applied to worms having dim TPH-1::GFP. The screening threshold is heuristically updated by every 50 images and possible double mutant is sorted based on threshold.

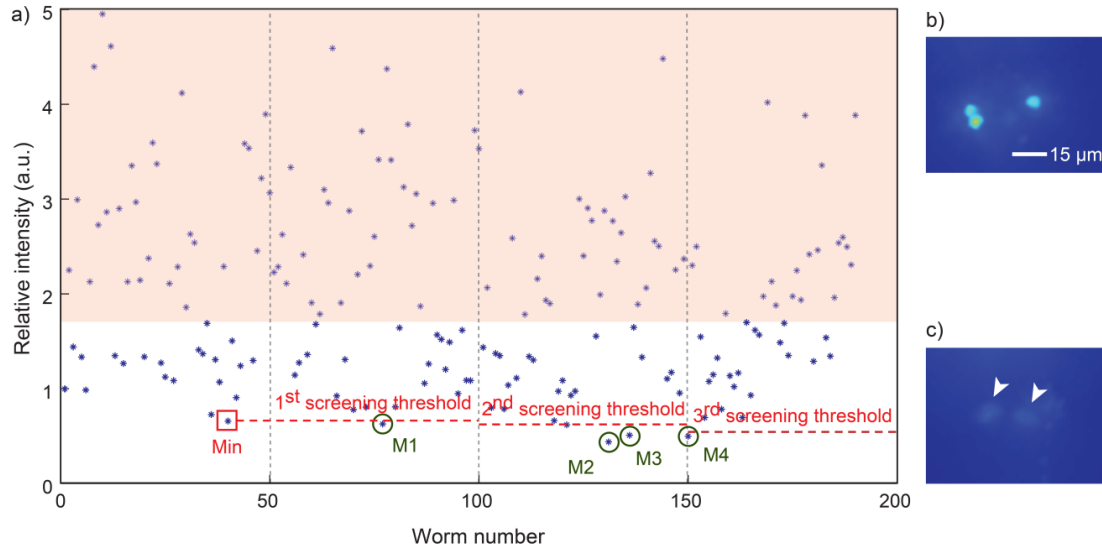


Figure 2.15 Quantitative screening with the adaptive algorithm. (a) The scattered plot showing *tph-1* expression levels in mutagenized *unc-43* worms. Each circle represents single worm intensity (average of two ADF neurons). Worms in shaded regions are bright enough to be identified by eyes due to high expression level of *tph-1*, which is above a certain threshold, and thus, it does not require to be quantified during actual screening. An example of high (b) and low (c) *tph-1* expression in ADF neurons. Mutant (M) selection in quantitative screening with flexible thresholds which are updated after every 50 worms. The first screening criterion is set based on minimum value (Min) of first 50 images.

2.6.2 Isolation of putative mutants

In the adaptive algorithm, first, we imaged fifty mutagenized *unc-43(gf)* worms, and the minimum value of target reporter expression in this group was set as a screening criterion. Putative mutant worms having lower expression level compared to the sorting

threshold were isolated. The sorting criterion was updated after each 50 additional worms passed through and were imaged. We assume that the rate of finding relevant mutant is low (i.e. lowest ~2% of worms). After hundreds of mutants, the screening criterion usually settles to a stable value and does not require more adaptations. This algorithm is easy to implement by modifying target selection rate depending on the expected hit rate with minimized efforts for verifying selected targets.

Using the algorithm and the single-layer microfluidic device, we performed quantitative screening of a mutagenized *unc-43* population (Fig. 2.15). When the intensity of TPH-1::GFP in ADF neurons is higher than a certain threshold, we can easily eliminate the worms having high expression of *tph-1* without quantification (Fig. 2.15b). Thus, there was no need to analyze the high expressing worms, i.e. those in the shaded region in Fig. 2.15a during actual screening. This rough estimate eliminates many worms quickly, and increases the overall throughput of screening. If the initial evaluation of the intensity is low, as shown in Fig. 2.15c, we quantified their expression levels and followed the adaptive algorithm to isolate the putative double mutants (Fig. 2.15a). For example, 0.66 (AU) was set to the first screening threshold and one worm with an intensity value of 0.63 was sorted. Subsequently, the threshold was updated as 0.64 and three worms whose intensities are 0.44, 0.51, and 0.50 were sorted. After hundreds of mutants, usually, the screening threshold stabilized to a value between 0.5 and 0.7 and does not require more adaptations. In total, we screened ~4000 mutagenized F2 *unc-43(gf)* worms and selected 95 putative mutants. Moreover, the usage of high-throughput microfluidic system enabled this screening within 25 hr, which would have taken longer

time (many days or possibly months) with manual conventional methods because of the quantitative requirement of this screen.

2.7 Statistical analysis to characterize putative mutants

After screening, we clonally cultured all the sorted putative F2 double mutants and re-imaged their progeny to eliminate false-positive strains. We compared the intensities of the putative double mutants to those of *unc-43(gf)* and eventually verified that 43 of the sorted populations had lowered *tph-1* expression than *unc-43(gf)* when cultured at 20 °C (Fig. 2.16). These differences are all significant by Student's *t* test and Kolmogorov–Smirnov test (KS-test) ($p < 0.01$). Among the 43 isolates, two (a156 and a157) have no *tph-1* expression. We further characterized the rest of the strains and compared them with the wild-type: 19% of them showed expression levels similar to the wild-type at 20 °C and some showed higher and the others showed lower average expression than the wild-type.

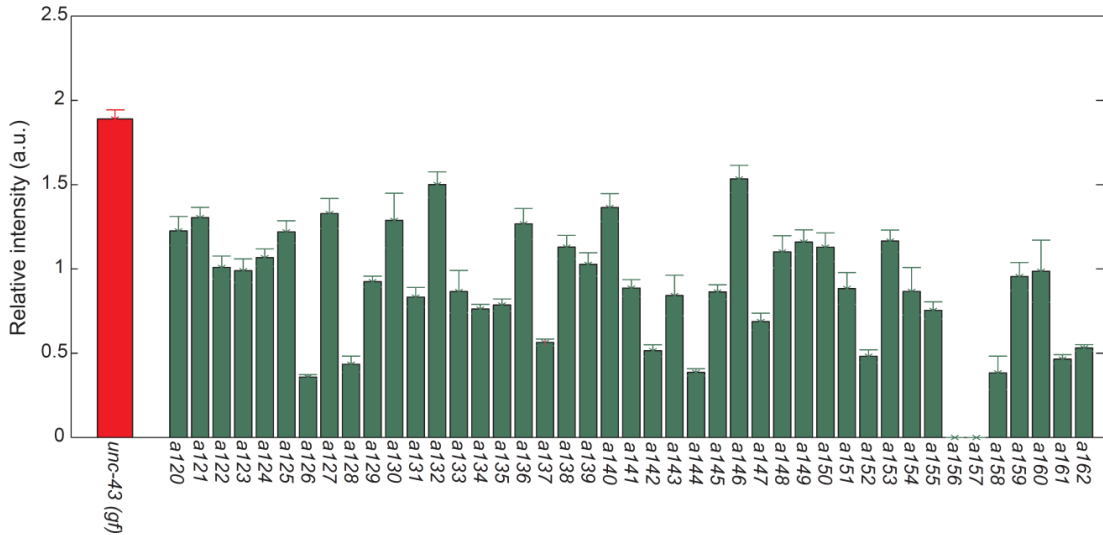


Figure 2.16 The average expression levels of *tph-1* in all progenies from isolated putative mutants were compared to *unc-43(gf)*. Statistically all mutants showed significant differences from *unc-43(gf)* ($p < 0.01$).

2.8 Phenotypical groupings based on probability distribution fitting

Interestingly, fourteen of the mutants have temperature-dependent expression in ADF L/R, similar to the wild-type (Fig. 2.17a). These temperature-dependent changes in the expression level are all statistically significant by Student's *t* test and KS-test. It is likely that the genetic lesions in these mutants do not disrupt the *tph-1::gfp* reporter itself. Thus these 14 strains could be useful to identify new regulatory genes in *tph-1* expression, particularly in the temperature-dependent responses. Furthermore, the actual distributions (histograms) of the expression levels can be informative. For all 14 strains, a Poisson distribution is not appropriate to fit the data since the Fano factor (σ^2/μ where σ is the variance and μ is the mean) of the reporter expression level is less than one. We considered both Gaussian and gamma distributions to describe the data. A Gaussian

distribution was used to fit symmetric distributions and gamma the asymmetric ones. In the cases that the data appear to be bimodal, we used double Gaussian distributions. Examples and categorizations of the mutants are shown in Fig. 2.17b–d. We hypothesize that these phenotypical groupings are possible results from the mutations happening in different specific pathways.

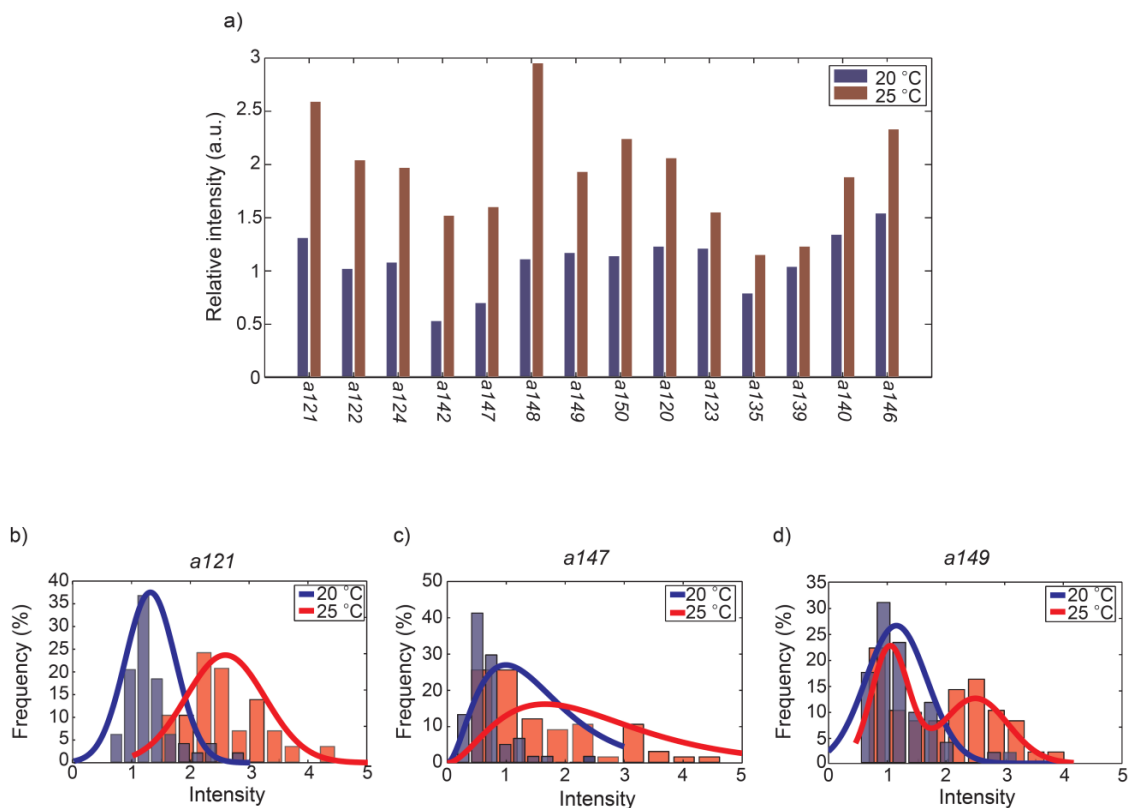


Figure 2.17 The Characterizations of putative mutants. (a) 13 putative mutants have temperature-dependent changes in *tph-1* expression. (b-d) Three types putative double mutants that have temperature-dependent phenotype of *tph-1* expression in ADF neurons. Each probability histogram of *tph-1* expression levels fits with either Gaussian (b), Gamma (c), or double Gaussian distribution (d).

2.9 Conclusions

In summary, we present a quantitative screen based on a simple adaptive algorithm using a single-layer microfluidic device. The fabrication of the microdevice is simple, giving a low failure rate and a robust and reliable performance. Since all control and fluid channels are in the same layer, optimizing space between the channels when designing the system is necessary. Moreover, to make a flexible control wall, proper aspect ratio was considered. In addition to the device, quantitative analysis with an adaptive algorithm was validated by performing the screening of mutated *unc-43(gf)* worms.

Using this system, we successfully performed a forward screen that identified *tph-1* regulators in less than 25 h and isolated 43 putative double mutants. The system developed here is flexible, and thus can be readily integrated with other studies for screening or imaging *C. elegans*; this system can also be applied to genome-wide RNAi screening and drug screening, to look for genes that alter/regulate tempo-spatial expression patterns of target genes in response to various conditions such as aging, food level, and pathogens.

CHAPTER 3

MODELING ANALYSIS OF POTENTIAL UNC-43/CAMKII-DEPENDENT REGULATORS OF TPH-1 EXPRESSION

3.1 Overview

To identify such UNC-43-dependent factors in *tph-1* (*tryptophan hydroxylase*) regulation, we performed the quantitative screening and found some putative mutants (results shown in Chapter 2). By imaging on the clonal populations (i.e. taking the progeny of the initially sorted mutants) and using statistical analysis to confirm the phenotypic characteristics of *tph-1* expression, we identified many “true” mutants. However, it is not clear that these mutants are physiologically relevant, i.e. whether the mutations act in the *unc-43* pathway. We developed a simple model in this section to compare the modeling results and the population imaging data to categorize the putative mutants. CaMKII encoded by *unc-43* is one of the major effectors of *tph-1* expression in ADF neurons. In the model, we included signaling upstream from *tph-1* promoter activities in ADF, and we analyzed the transcriptional activity of *tph-1*. The model assumes two transcriptional factors in *tph-1* regulation: one inhibitor and one activator. These transcriptional factor activities are regulated by phosphorylation from signal transduction network. We optimized parameters by fitting to experimental results of *tph-1* expression in three strains cultured at 20 °C or 25 °C. There are, however, uncertainties in parameter estimation due to the lack of details of the pathway and more importantly experimental data to further constrain the parameters. We showed that the model system is highly sensitive to differences in parameter changes. Thus, we performed the

robustness test by generating multiple random parameter sets. While the deterministic and stochastic signatures from the model can partially help us formulate further hypotheses about the regulatory process, we suggest that future experiments be carried out to further validate and embellish the model.

3.2 Background

We performed quantitative screening for mutants in the transcriptional regulation of tryptophan hydroxylase (TPH; *tph-1*) in *C. elegans* in Chapter 2. TPH-1 is a rate-limiting enzyme for the synthesis of neurotransmitter serotonin, which is known to integrate environmental signals and modulate various neural functions such as mood, feeding, and aggression.[1] Deficiency of serotonin signaling is associated with various mental disorders such as depression.[2, 3] Moreover, deficient serotonin signaling leads to diseases like migraine, an episodic pain disorder, possibly through abnormal activity of calcium channel.[4, 5] For therapeutic interest or general inquiry to understand how environmental perception is mediated to change physiology, it is significant to identify the regulatory mechanism of serotonin production.

The tryptophan hydroxylase gene, *tph-1*, is expressed in several serotonergic neurons, mainly NSM and ADF.[1, 6] Among serotonergic neurons where the *tph-1* are expressed, we focus on ADFL/R in this study, since stressful environmental conditions such as starvation, aversive stimuli like pathogens, and high temperature increase the *tph-1* expression in the ADF neurons, and not in other serotonergic neurons.[5, 7, 8] In addition, we only consider temperature-dependent regulation of *tph-1* expression; we assume that all animals are cultured under normal conditions (in terms of food and stress)

except temperature. Experimentally, we can roughly satisfy this condition by controlling culture condition such as food level and food quality. Here, all animals were fed with abundant amount of *E. coli* OP50 and grown according to standard protocols at 20 °C or 25 °C.[9]

Moreover, the worm age affects the expression level of the target gene as described in Chapter 2. We focused on Day 1 adult animals. It is important to control worm age because it affects the expression level of the target gene and developmental rate significantly. To obtain Day 1 adults worms, we cultured *C. elegans* for about 60 hr at 20 °C and about 46 hr at 25 °C.

We experimentally confirmed that ADF neurons only respond to rearing temperature. The imaging method was described in Chapter 2. In Fig. 3.1, we analyzed the expression levels of *tph-1* in ADF (a) and NSM neurons (b) in three strains at 20 °C or 25 °C. For clear comparison, we performed the statistical analysis by applying a two-tailed Students' *t* test. Here, we confirmed the literature result that ADF shows large temperature-dependent phenotype changes ($p < 10^{-20}$) in wild-type compared to NSM that does not have any significant differences at different temperatures.

Many genetic factors including insulin-like peptides, transforming growth factor beta, and calcium signaling pathways are involved in regulating *tph-1* expression in ADFL/R.[1, 5, 10, 11] However, it has been assumed that Ca^{2+} /Calmodulin-dependent protein kinase (CaMKII) is a critical mediator of temperature-dependent regulation in ADF.[5, 10-12] This is because 1) CaMKII-dependent *tph-1* regulation is ADF-specific (no effect on other serotonergic neurons), and 2) the mutant of *unc-43*, a gene that encodes the CaMKII in *C. elegans*, has no significant temperature-dependent changes in

tph-1 expression.[11] Our experimental results also agree with their observation (Fig. 3.1). A gain-of-function (*gf*) mutant of *unc-43* increases *tph-1* expression in ADFL/R and a loss-of-function (*lf*) mutant of *unc-43* decreases it. However, *tph-1* expressions in NSM neurons are statistically similar among wild-type and *unc-43* mutants. Also, *unc-43* mutants show very little changes at different temperatures (significance in Student's *t*-test, $p=0.064$ for *unc-43(gf)*, and $p=0.0026$ for *unc-43(lf)*).

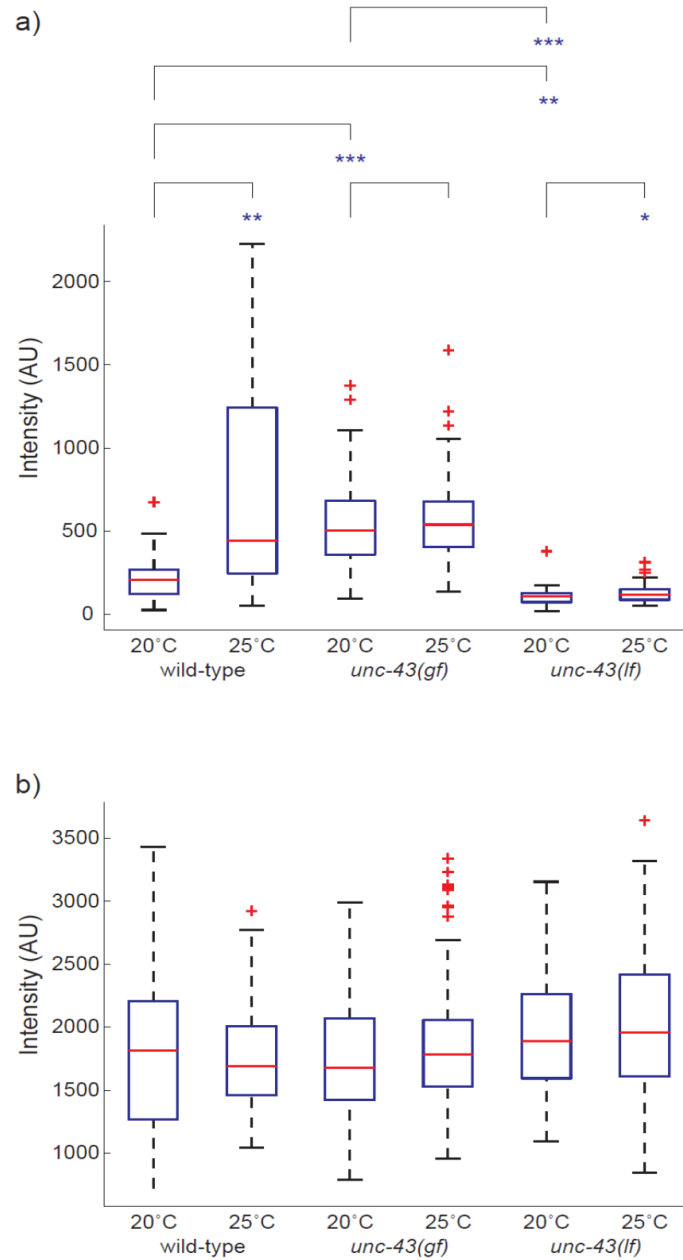


Figure 3.1 Boxplot of *tph-1* expression in a) ADF and b) NSM neurons in wild-type (GR1333, n=64 and 89 respectively), *unc-43(gf)* (ZC5, n=105 and 153 respectively), and *unc-43(lf)* (ZC3, n=93 and 66 respectively), at 20 °C or 25 °C. Differences between culture temperature in each strain, and differences induced by genetic factors in 20 °C were analyzed statistically for both ADF and NSM neurons. Statistical significance are marked as followed (***: $p < 10^{-20}$, **: $p < 10^{-10}$, *: $p < 0.05$).

In addition to UNC-43/CaMKII, we include the activity of Calcineurin (CaN), which is a known partner/competitor of CaMKII in model network.[12] Initially, we assumed to exclude the contribution of CaN; however, in such case, we could not fit modeling results to experimental results with any parameter set. Thus, to mimic the temperature-dependent response in *unc-43* single and especially in some of double mutants, CaN activity needs to be considered. It also has been known that CaN is also regulated by Ca^{2+} /Calmodulin activity.

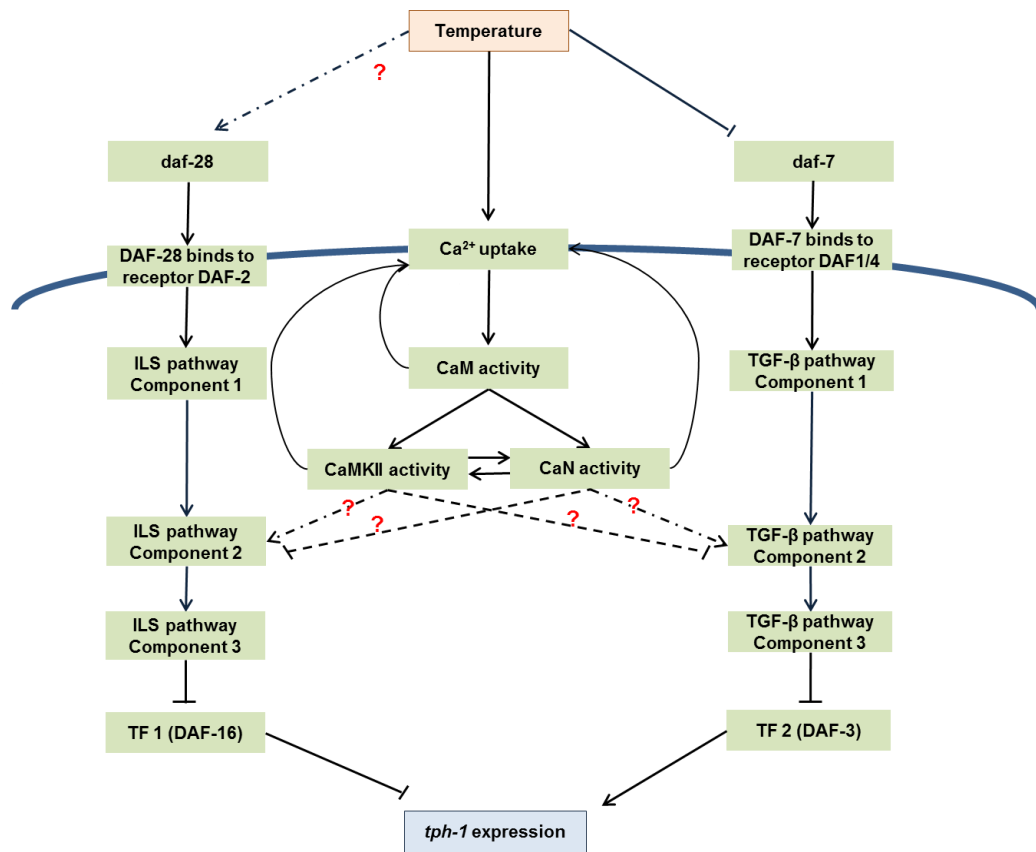


Figure 3.2 The currently known temperature-responsive regulatory pathways of *tph-1* expression in ADF neurons with some putative details (arrows) still to be experimentally confirmed. ILS, TGF- β , and Ca^{2+} signaling pathways are involved in this regulation.

3.3 Model development

We simplified the pathway in Fig. 3.2 according to following assumptions. All assumptions we made are summarized below:

- 1) According to Wan *et al.*,[13] CaN and UNC-43/CaMKII in the horn neuron of rats behave like switches, in that CaMKII activity is higher than CaN at high Ca^{2+} levels and CaMKII activity is lower than CaN at low Ca^{2+} levels. This switch-like behavior is also validated by biochemical model and experiments.[14] Graupner *et al.* showed that CaMKII has high association constant of Ca^{2+} when Ca^{2+} level is high. In contrast, CaN is easy to bind Ca^{2+} and become active when Ca^{2+} level is low. We assume that these molecules behave similarly in ADF in *C. elegans*. This implies that in the model, CaMKII activity increases and CaN activity decreases as a function of temperature.
- 2) CaMKII and CaN are known to exert reciprocal influences on the response.[12, 15] Thus, we assume that active CaN inhibits *tph-1* expression.
- 3) Estevez *et al.* hypothesize that DAF-16 may function as the ultimate downstream effector regulating the level of *tph-1* expression through insulin-like signaling (ILS) pathway although other downstream effectors may also contribute to the overall regulation of *tph-1* (such as DAF-3).[5, 10] This means that downstream of CaMKII and CaN does not independently regulate *tph-1* expression. In this

model, we assume CaMKII and CaN regulate *tph-1* expression through both ILS and TGF- β pathways.

Based on the above assumptions, we reduced the pathway in 3.2 to that in 3.3 and constructed the model network. Here, we are more interested in output levels (*tph-1* expression) in steady state rather than dynamic responses. Moreover, in this model, we do not consider how many molecules are involved in specific pathway and how exactly each molecule behaves. Thus, we lumped multiple parameters and components together into a single representative component in a specific pathway. The simplified network is shown in Fig. 3.3. *tph-1* expression is assumed to be regulated by two transcriptional factors; *I* (assumed to be DAF-16) is an inhibitor and *A* (possibly DAF-3) is an activator.[6] These transcriptional factor activities are regulated by phosphorylation from signal transduction network (kinase cascade). All transitions between states obey mass-action kinetics.[16-18] If transcriptional factors are phosphorylated, they cannot remain in the nucleus area and cannot bind to the promoter of *tph-1*. ILS_{up} increases *tph-1* expression by making inhibitor (*I*) inactive but $TGF\beta_{up}$ inhibits *tph-1* expression. They are activated when specific ligands binds to the target receptors (DAF-2 and DAF-1/DAF-4 in Fig. 3.2). In addition, CaMKII and CaN that are regulated by temperature affect both transcriptional factor activities antagonistically.

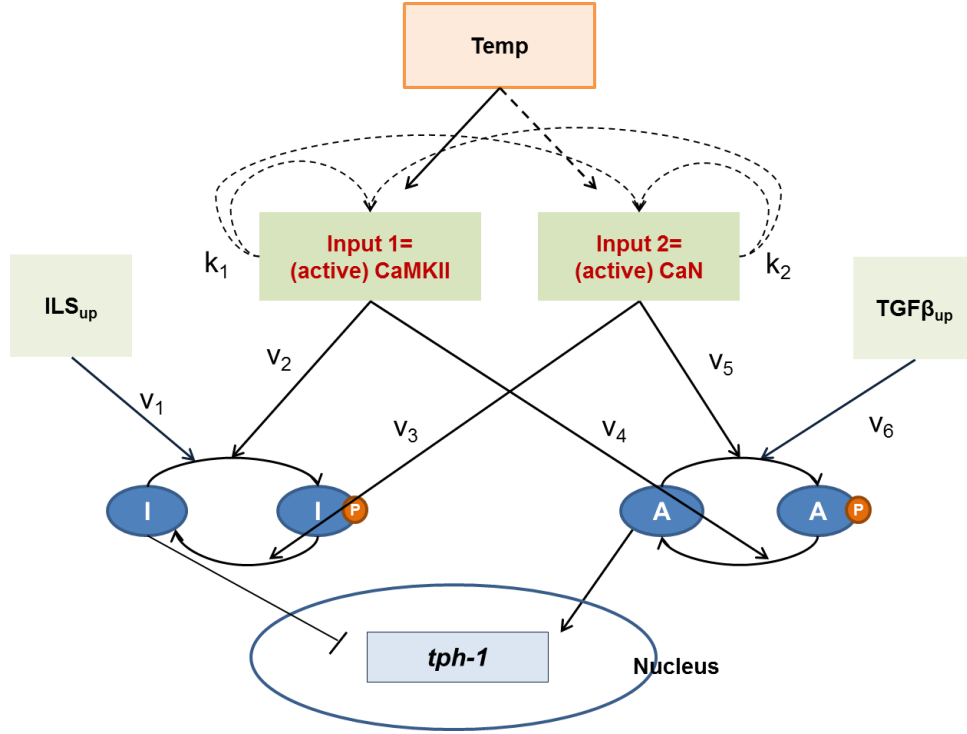


Figure 3.3 The schematic of simplified model network of *tph-1* transcription in ADF neurons. Parameters v_1 - v_6 are kinetic parameters in phosphorylation pathway. k_1 - k_2 are threshold for feedback regulation of CaMKII and CaN respectively. Two transcriptional factors regulate *tph-1* expression: inhibitor *I* and activator *A*. Due to lumped components, *I* can be regarded as ILS downstream component, and *A* represents TGF- β downstream regulator as well. Active CaMKII (either Ca^{2+} -bound CaMKII or *unc-43(gf)*) increases *tph-1* expression level by inhibiting *I* (through v_2) and activating *A* (through v_4).

3.4 Model formulation of *tph-1* regulation in ADF neurons

3.4.1 Model equations

First, based on Alon's analysis,[16, 17] we derived two ordinary differential

equations (ODE) (Eqn. 1 and 2) to describe phosphorylation pathways: one for inhibitor and the other for activator. The inhibitor activity is determined by both CaMKII and CaN via each rate strength v_2 and v_3 (Eqn. 1 and Eqn. 2). For activator activity, we considered CaMKII- and CaN- dependent regulation as well via v_4 and v_5 . After deriving these equations, the fraction of active factors is obtained to study steady-state behavior of these transcriptional factors (Eqn. 3 and Eqn. 4).

$$\frac{dI}{dt} = -v_1 \cdot I \cdot ILS_{up} - v_2 \cdot I \cdot CaMKII + v_3 \cdot (I_{tot} - I) \cdot CaN + \alpha(I_{tot} - I) \quad (1)$$

$$\frac{dA}{dt} = -v_6 \cdot A \cdot TGF\beta_{up} - v_5 \cdot A \cdot CaN + v_4 \cdot (A_{tot} - A) \cdot CaMKII + \alpha(A_{tot} - A) \quad (2)$$

$$I = \frac{I_{tot}(v_3 \cdot CaN + \alpha)}{v_1 \cdot ILS_{up} + v_2 \cdot CaMKII + v_3 \cdot CaN + \alpha} \quad (3)$$

$$A = \frac{A_{tot}(v_4 \cdot CaMKII + \alpha)}{v_6 \cdot TGF\beta_{up} + v_4 \cdot CaMKII + v_5 \cdot CaN + \alpha} \quad (4)$$

$$\frac{d(tph1)}{dt} = \sum_{i=1}^6 P_i \cdot \beta_i - \alpha \cdot tph1 \quad (5)$$

where

$$P_1 = P(I)^2 \quad (6)$$

$$P_2 = 2 \cdot P(I) \cdot (1 - P(I)) \cdot (1 - P(A)) \quad (7)$$

$$P_3 = 2 \cdot P(I) \cdot (1 - P(I)) \cdot P(A) \quad (8)$$

$$P_4 = (1 - P(I))^2 \cdot (1 - P(A))^2 \quad (9)$$

$$P_5 = 2 \cdot P(A) \cdot (1 - P(A)) \cdot (1 - P(I))^2 \quad (10)$$

$$P_6 = P(A)^2 \cdot (1 - P(I))^2 \quad (11)$$

$$\beta_1 = 2\beta_0 \quad (12)$$

$$\beta_2 = \beta_0 + \beta_1 \quad (13)$$

$$\beta_3 = \beta_0 + \beta_2 \quad (14)$$

$$\beta_4 = 2\beta_1 \quad (15)$$

$$\beta_5 = \beta_1 + \beta_2 \quad (16)$$

$$\beta_6 = 2\beta_2 \quad (17)$$

Next, we analyzed how these active transcriptional factors regulate *tph-1* transcription. In general, the average production rate is a combination of rates given the occupancy status of the binding site. The dynamics of *tph-1* expression can be simply represented in Eqn. 5. The fraction of active (un-phosphorylated) inhibitor *I* and activator *A* determine this probability (Eqn. 6-11). We assume that *I* is the dominant factor, which means promoter activity of *tph-1* is weak (β_0) when *I* is bound regardless of *A* activity. Once inhibitor binds to the promoter, we assume that target protein cannot be produced. If there is no bound inhibitor, the target protein production can be strong or basal depending on the activator bind. Since the strain we used for experiments contains a multi-copy transgene, here, we consider two copies, which are the average copy numbers of target DNA. We derived the production rate at occupancy status of two promoters (Eqn. 12-17, Tab. 3.1). For example, production rate is $\beta_0+\beta_1$, when one promoter is bound with *I* and the other promoter is not bound with any regulator.

Table 3.1 The production rate given the combination of each occupancy status of promoter site in first and second copy

Copy #1	Copy #2	A +		A -	
		A +	A -	A +	A -
I +	I +	$\beta_0 + \beta_0$	$\beta_0 + \beta_0$	$\beta_0 + \beta_0$	$\beta_0 + \beta_0$
	I -	$\beta_2 + \beta_0$	$\beta_1 + \beta_0$	$\beta_2 + \beta_0$	$\beta_1 + \beta_0$
I -	I +	$\beta_0 + \beta_2$	$\beta_0 + \beta_2$	$\beta_0 + \beta_1$	$\beta_0 + \beta_1$
	I -	$\beta_2 + \beta_2$	$\beta_1 + \beta_2$	$\beta_2 + \beta_1$	$\beta_1 + \beta_1$

3.4.2 Parameter optimization with experimental data

There is no measurable kinetic information for this system from the literature. Nonetheless, this model can be helpful to investigate general behaviors of the

phenotypic changes induced by specific genetic perturbation compared to the starting genotype in our suppression screen - (*unc-43(gf)* single mutant. In other words, we do not need to know exactly how much each component (ILS, TGF- β , CaN, CaMKII, and so on) exists in ADF cells; a relative amount can be informative of putative mechanisms. Thus, we assume some of parameters are not perturbed in this system. Also, we defined CaMKII and CaN activity according to following assumptions. All assumptions we made are summarized below:

- 1) Based on Lisman *et al.*, CaMKII in *unc-43(gf)* does not bind to Ca^{2+} . [19] Since activity of CaMKII does not depend on Ca^{2+} levels, we assume that CaMKII has constant activity at any temperature, which is different from wild-type behavior. This means we assume that $\text{CaMKII}=1$ in *unc-43(gf)* and $\text{CaMKII}=0$ in *unc-43(lf)*.
- 2) Also, Lisman's observation can lead to the second assumption that activities of CaMKII and CaN in *unc-43* mutants are different from those of wild-type. However, their activity in *unc-43(gf)* is assumed to be similar with that of *unc-43(lf)*. Thus, we assume CaN activity at 25 °C is 0.5. Note that CaN activity at 20 °C is assumed to be increased based on the first assumption in section 3.3.

Since we assumed that some of parameters are not perturbed, we can thus optimize the other parameters relatively to fit with the average expression levels of *tph-1* in *unc-43* mutants at each temperature. For the parameter optimization, we generated the large allowed parameter space ($> 10^8$) based on random sampling, and

then selected the parameter sets (β_{1-3} and v_{2-4}) that result in minimum difference of average expression levels of *tph-1* with that of experimental data in *unc-43(gf)*, and *unc(lf)* at 20 °C and 25 °C. The obtained parameters are summarized in Tab. 3.3. We caution here that more parameter optimization with further experimental data should be done in the future.

Table 3.2 Parameters assumed not to be perturbed

α	1
ILS_{up}	0.5
v_1	1
$TGF\beta_{up}$	0.5
v_6	1
CaMKII in <i>unc-43(gf)</i>	1
CaMKII in <i>unc-43(lf)</i>	0
CaN at 20 °C	0.5

Table 3.3 Parameter set obtained by optimization with experimental data of average expression level at each temperature through deterministic steady state model.

β_1	104
β_2	784
v_2	1.2472
v_3	3.3170
v_4	8.0686
v_5	1.8582
CaN at 20 °C	0.554

3.5 Perturbing model parameters

3.5.1 Sensitivity analysis

Using the model developed, here we explored the possible changes in average *tph-1* expression levels by parameter variations. To do that, we performed the

sensitivity analysis on steady-state model. Sensitivity analysis usually quantify the change in model behavior as a certain parameter x varied from their optimized value x^* . [20-22] Here, we systematically changed any single parameter in the model network and measured the changes in average *tph-1* expression levels at 20 °C and 25 °C. Each parameter is changed by multiplying 10^x (where x is taken from a normal distribution with mean 0 and standard deviation 1). [23] Some results are represented in Fig 3.5-Fig.3.7. We observed that the changes in output (the average expression level of *tph-1*) is highly sensitive to single parameter variations.

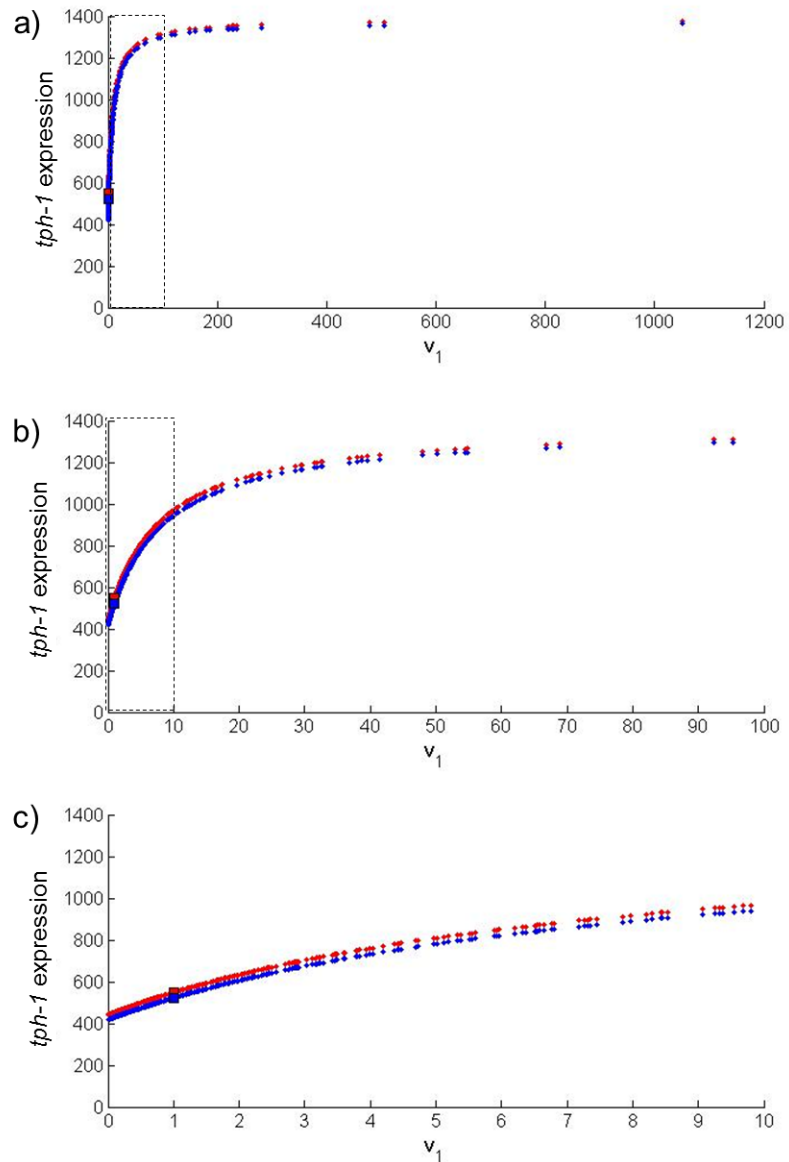


Figure 3.5 a) Changes of average *tph-1* expression in *unc-43(gf)* at 20 °C (blue) and 25 °C (red) by v_1 (see Fig. 3.3) variation. Squares represent average *tph-1* expression in *unc-43(gf)* at 20 °C (blue) and 25 °C (red) with the optimal parameter (v_1 is assumed to be a constant, 1). b) Zoomed in image of the boxed region in a. c) Zoomed in image of the boxed region in b. A total of 500 variations were simulated.

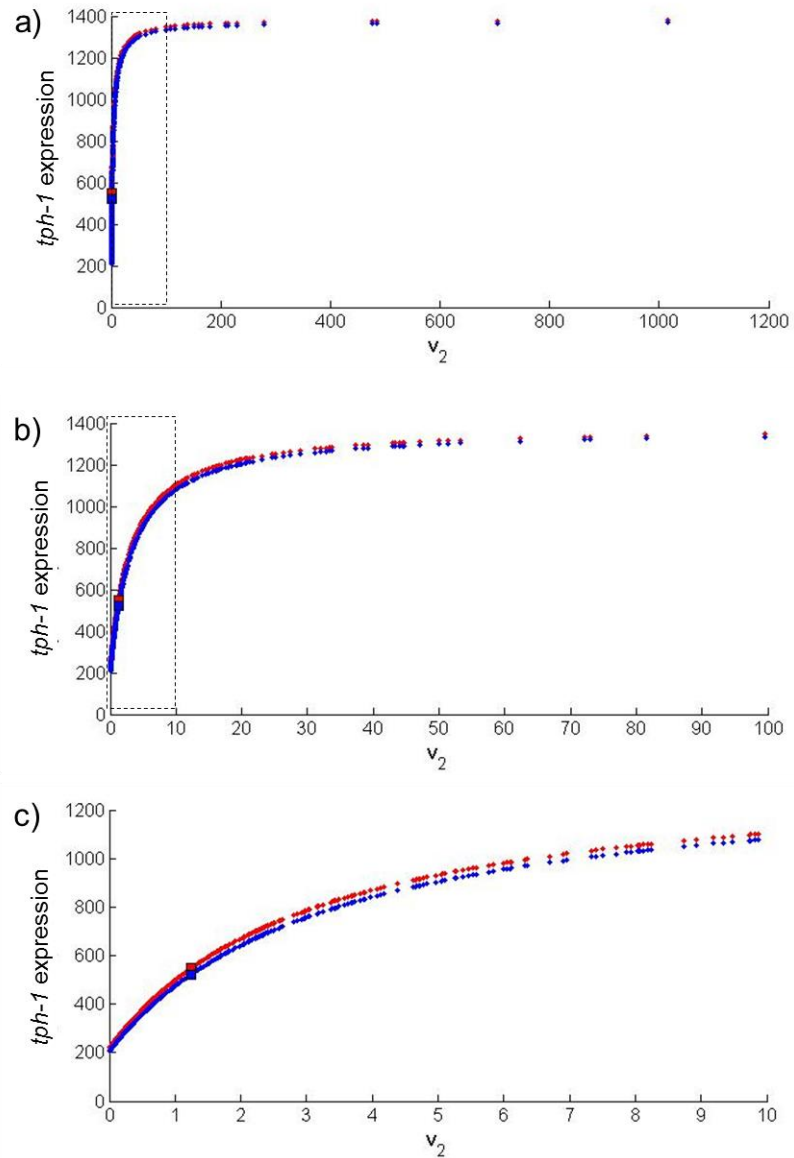


Figure 3.6 a) Changes of average *tph-1* expression in *unc-43(gf)* at 20 °C (blue) and 25 °C (red) by v_2 (see Fig. 3.3) variation. Squares represent average *tph-1* expression in *unc-43(gf)* at 20 °C (blue) and 25 °C (red) with the optimal parameter (v_2 is optimized as 1.2472). b) Zoomed in image of the boxed region in a. c) Zoomed in image of the boxed region in b. A total of 500 variations were simulated.

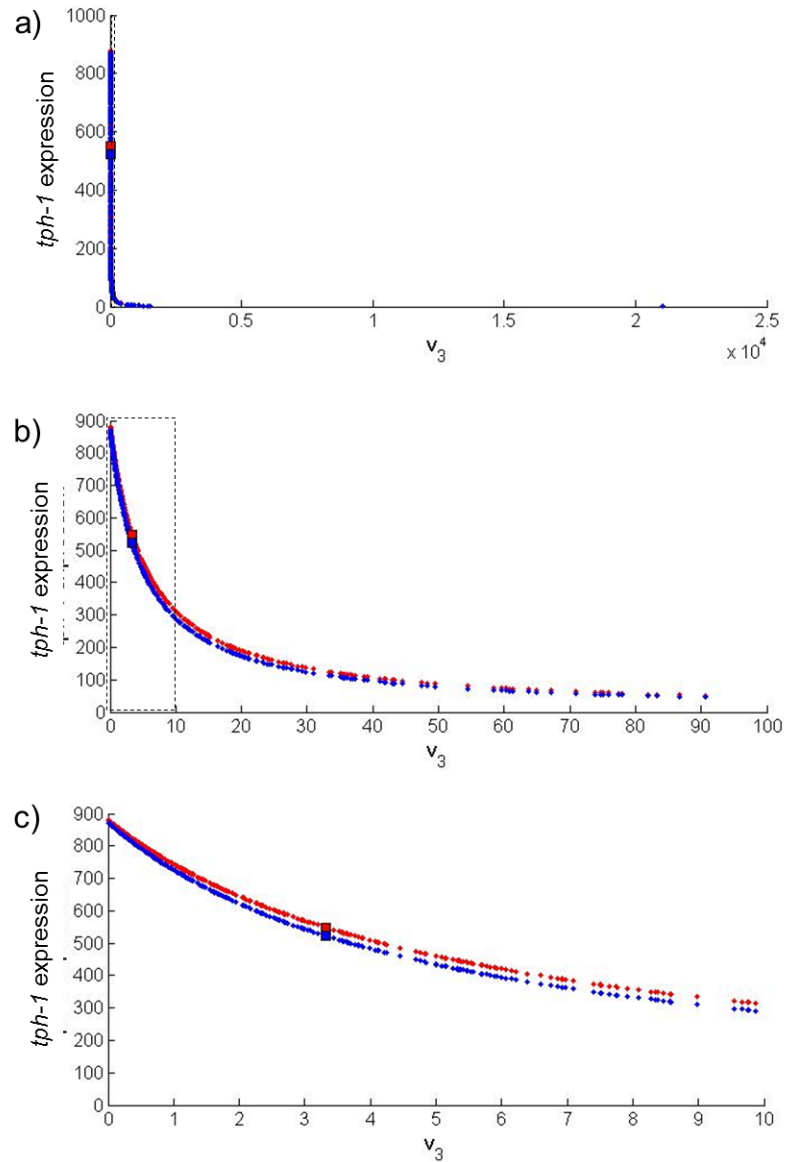


Figure 3.7 a) Changes of average *tph-1* expression in *unc-43(gf)* at 20 °C (blue) and 25 °C (red) by v_3 (see Fig. 3.3) variation. Squares represent average *tph-1* expression in *unc-43(gf)* at 20 °C (blue) and 25 °C (red) with the optimal parameter (v_3 is optimized as 3.317). b) Zoomed in image of the boxed region in a. c) Zoomed in image of the boxed region in b. A total of 500 variations were simulated.

3.5.2 Possible candidates from isolated mutants for UNC-43-interacting factors

We assume that changes in parameters correspond to actual changes in molecular behavior. Thus, we analyzed the phenotypic changes in model system by parameter variation and compared to the experimental results of the average *tph-1* expression levels in isolated mutants. Since we do not know how much exactly this parameter would be changed, we considered all possible variation of each parameter using sensitivity analysis and created the phenotypical space of hypothetical (double) mutants. Note that we only need to consider *tph-1* expression level in putative double mutants lower than its expression in *unc-43(gf)* at 20 °C (which is the goal of the screen detailed in Chapter 2 and section 3.2). Thus, we neglected some variations of parameters if they induce the elevated expression level of *tph-1*. For example, we considered followings only 1) the increases of some parameters: $TGF\beta_{up}$, $ILS_{down}/inhibitor (I)$, v_3 , v_5 , and 2) decreases of the other parameters: ILS_{up} , $TGF\beta_{down}/activator (A)$, v_2 , v_4 (see model network in Fig. 3.3).

For better visualization, we re-plotted all sensitivity results and compared the *tph-1* expression level at 20 °C (*x-axis*) to differences in between expressions at two different temperatures (*y-axis*) in Fig. 3.8. We observed that changes in parameters downstream of CaMKII and CaN can possibly generate only small differences of *tph-1* expressions at the two temperatures. Among 43 putative mutants, eight mutant alleles are in the phenotypical space created by varying model parameters in Fig. 3.9. We suggest to sequence the eight mutants that have small *tph-1* temperature effect since they have a higher likelihood to be downstream of CaMKII and CaN pathways.

The other mutant alleles showed larger expression difference resulted from

varying temperature experimentally. Because the model cannot account for these variations, we hypothesize that regulations upstream of CaN (and CaMKII) and possibly additional feedback need to be considered to understand all phenotypic characteristics of double mutants. We discuss more details in section 3.6.

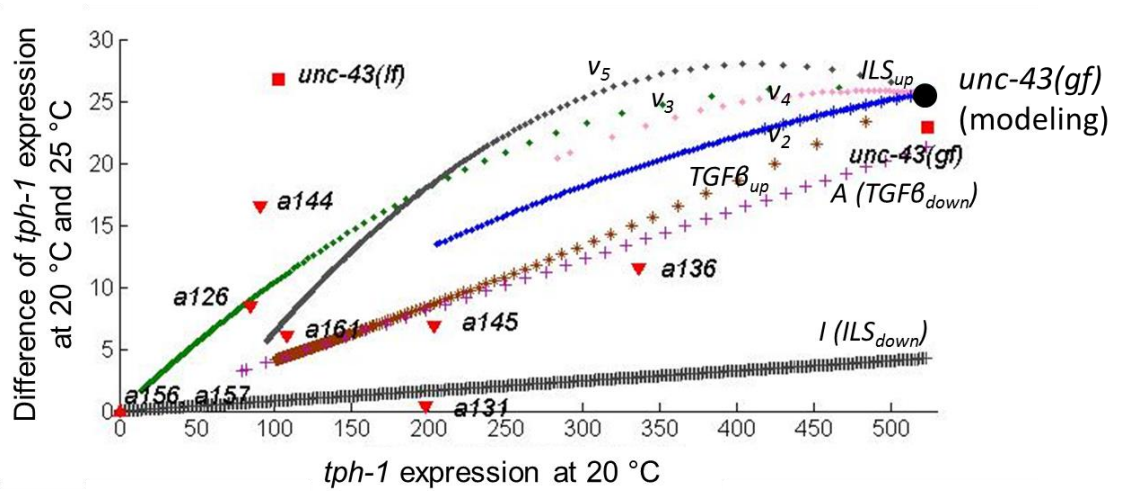


Figure 3.8 Allowable range of *tph-1* expression generated by each parameter changes. Each line indicates the possible changes in average *tph-1* expression levels at two temperatures based on simulation. Red triangles represent experimental results of mutant alleles in the allowable range of the phenotypical space, which may potentially carry mutations downstream from CaMKII.

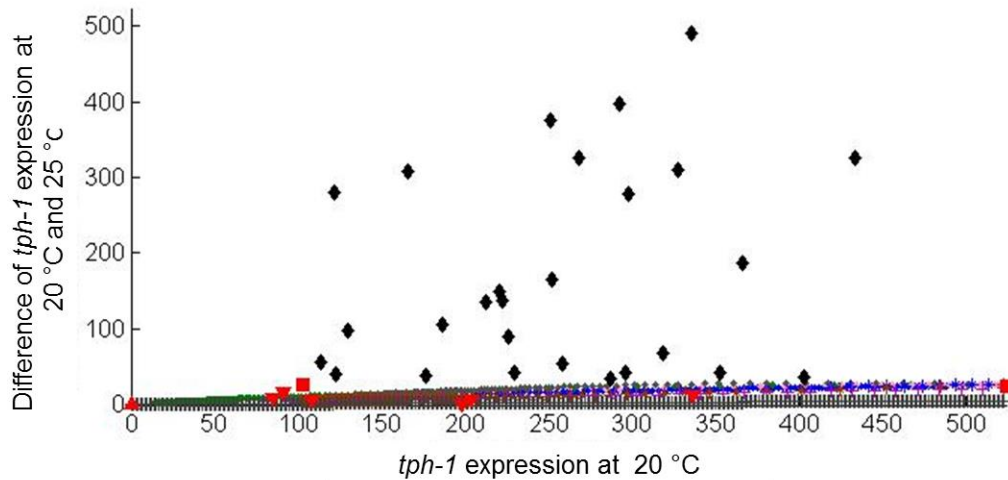


Figure 3.9 Comparison of phenotypic changes generated by model and average expression levels of putative mutants. Fig. 3.8 is zoom-in view of Fig. 3.9 (see *y-axis*). Red triangle indicates that phenotypes of double mutants exist within the allowable range generated by parameter changes. Black diamonds represent phenotypes of double mutants having larger differences of *tph-1* expressions at the two temperatures.

3.5.3 Robustness test

Because of uncertainties of parameters, we needed to validate the system robustness. To do that, first we generated random parameter sets that have error less than the defined value (here, 10 (AU); 1.9% over mean of *tph-1* expression in *unc-43(gf)* at 20 °C). We defined the threshold based on experimental measurement; the average of the standard errors in *unc-43* mutants at two temperatures is 9.06 (AU). Next, we performed the sensitivity analysis as we discussed above. In Fig. 3.10 we measured the changes in average *tph-1* expression at two temperatures by varying v_2 from multiple parameter sets. We also tested sensitivity analysis based on v_4 in Fig. 3.11. The v_2 and v_4 are two parameters downstream of CaMKII. We observed the allowable range of difference in

tph-1 expressions at two temperatures was increased by ~2 fold higher than the range obtained using optimal parameter set; the differences at temperatures, however, remained small. Based on the robustness test, we suggest sequencing mutants that have small *tph-1* temperature effect but more validations are required for analyzing the model network and parameters.

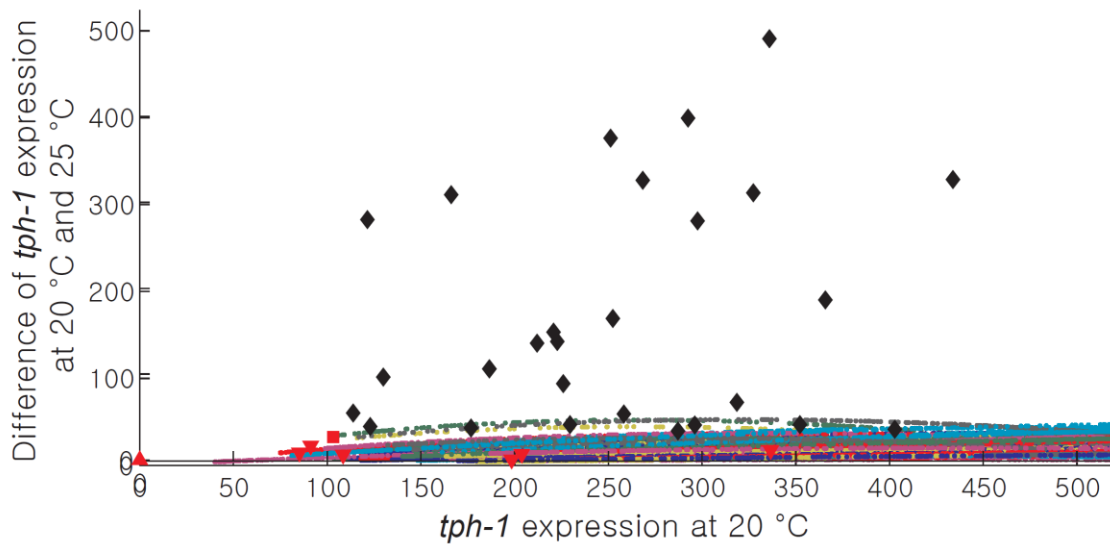


Figure 3.10 The simulation results of changes in average *tph-1* expression at 20 °C and 25 °C by variation parameter v_2 from 91 parameter sets. These parameter sets are generated from 10^6 random sampling; then, 91 parameter sets are selected based on defined error (here, 10 (AU)) compared to experimental results. Each line constituted with circles showing the possible changes in *tph-1* expression by v_2 variation at each parameter set. Red triangle indicates that phenotypes of double mutants exist within the allowable range generated by parameter changes from the optimal set (see section 3.4.2 and Fig. 3.9). Black diamonds represent phenotypes of double mutants used not to be within the range by single parameter variation from the optimal set.

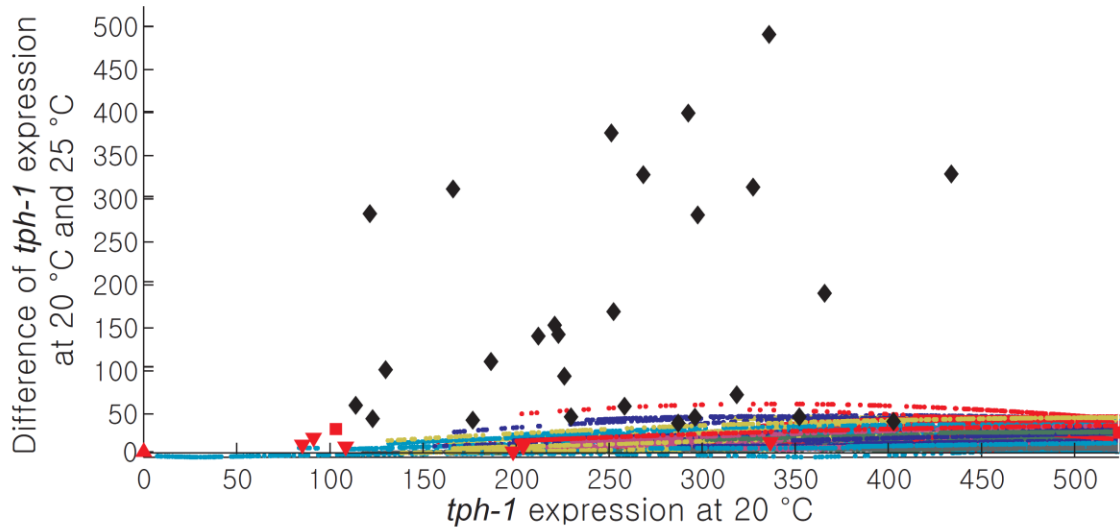


Figure 3.11 The simulation results of changes in average *tph-1* expression at 20 °C and 25 °C by variation parameter v_4 from 137 parameter sets. These parameter sets are generated from 1.5×10^6 random sampling; then, 137 parameter sets are selected based on defined error (here, 10 (AU)) compared to experimental results. Each line constituted with circles showing the possible changes in *tph-1* expression by v_4 variation at each parameter set. Red triangle indicates that phenotypes of double mutants exist within the allowable range generated by parameter changes from the optimal set (see section 3.4.2 and Fig. 3.9). Black diamonds represent phenotypes of double mutants used not to be within the range by single parameter variation from the optimal set.

3.6 Stochastic effects

3.6.1 Stochastic models to match the population variations in *unc-43* mutants

The above analysis was based on steady state expression profile and perturbations in the kinetic or affinity parameters. It is possible that the stochastic

signatures of the mutant populations can also inform us of mechanisms. To understand the differences in expression distributions in populations of animals, we considered stochastic effects on CaMKII, CaN, and *tph-1* expressions themselves. The stochastic effects on CaMKII and CaN are considered by multiplying random numbers from the normal distribution with mean 1 and defined standard deviation σ . Due to positive feedback in Fig. 3.2 and Fig. 3.3,[12] if CaMKII or CaN is higher than their own threshold, their levels are amplified to normal distribution with mean $CaMKII^{pos}$ or CaN^{pos} , respectively. Since CaMKII encoded by *unc-43* does not bind to Ca^{2+} in *unc-43(gf)* mutants (assumption 1 in section 3.3), CaMKII is not assumed to be involved in feedback loop. Parameters are roughly optimized to match the phenotypic distribution in *unc-43(gf)*, the parent single mutant before mutagenesis (Tab. 3.4). For the stochastic effects on *tph-1* expression, we used Gillispie algorithm.[24] Gillispie algorithm generates numerical trajectories of target production as shown in Fig. 3.12. Fig. 3.15 and Fig. 3.16 represent the simulational results of *unc-43* mutants, and can be compared to experimental results in Fig. 3.13 and Fig. 3.14.

Table 3.4 Parameters optimized for stochastic effects in CaN activity.

k_2	0.64
CaN^{pos}	1.3

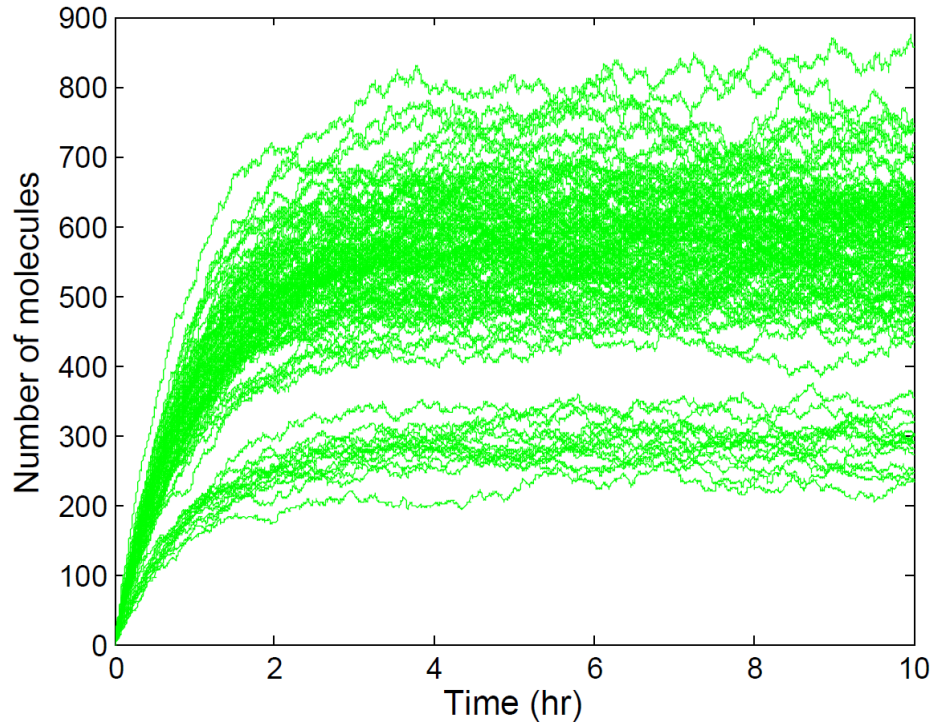


Figure 3.12 The numerical trajectories of number of molecules as a function of time, generated by Gillispie algorithm. Here, we measured the *tph-1* expression levels in *unc-43(gf)* at 25 °C. A total of 100 iterations were simulated.

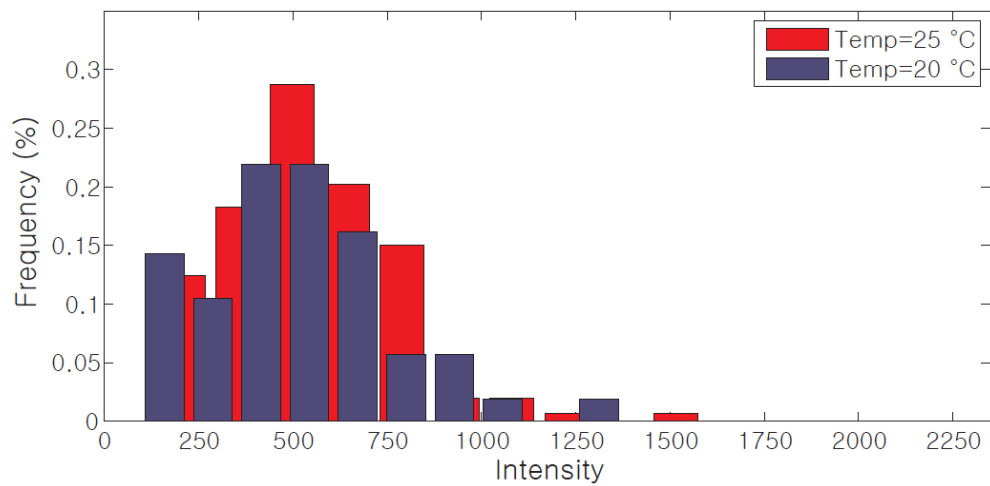


Figure 3.13 The histogram of experimental results of *tph-1* expression in *unc-43(gf)* at 20 °C and 25 °C.

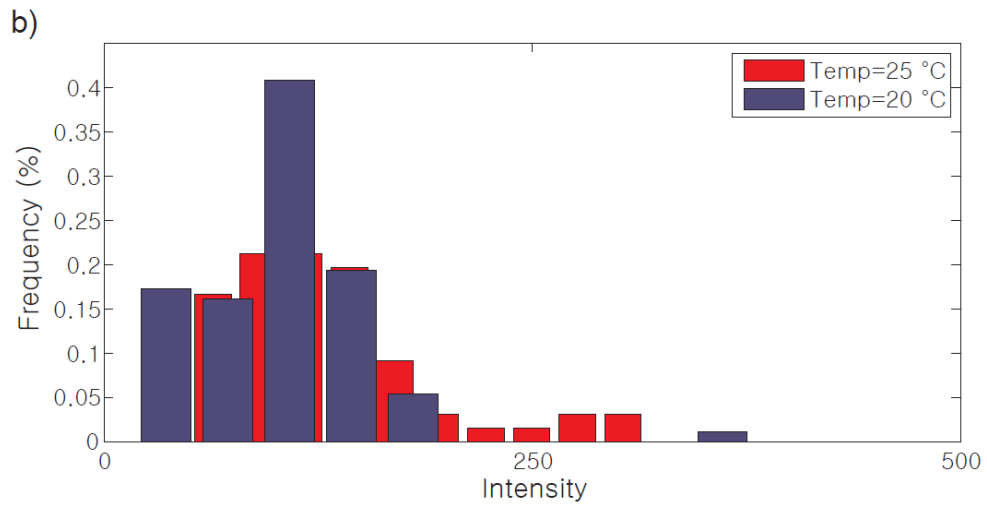
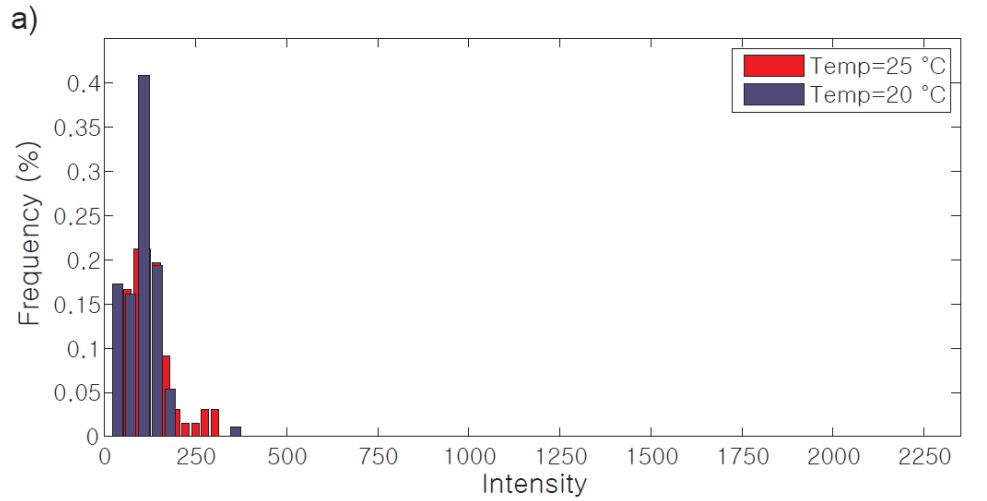


Figure 3.14 a) The histogram of experimental results of *tph-1* expression in *unc-43(lf)* at 20 °C and 25 °C. (Same *x*-scale in Fig. 3.13 for comparing the genetic influence on target gene expression.) b) zoom-in view of a) to visualize the changes of distribution by temperature.

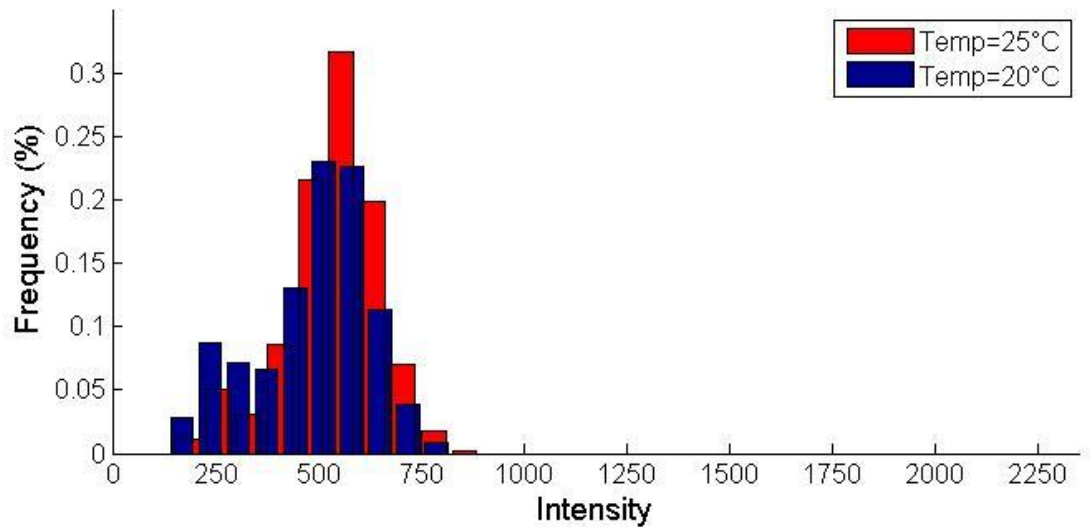


Figure 3.15 The histogram based on simulation results of *tph-1* expression in *unc-43(gf)* at 20 °C and 25 °C; the model parameters are roughly optimized to fit the experimental results.

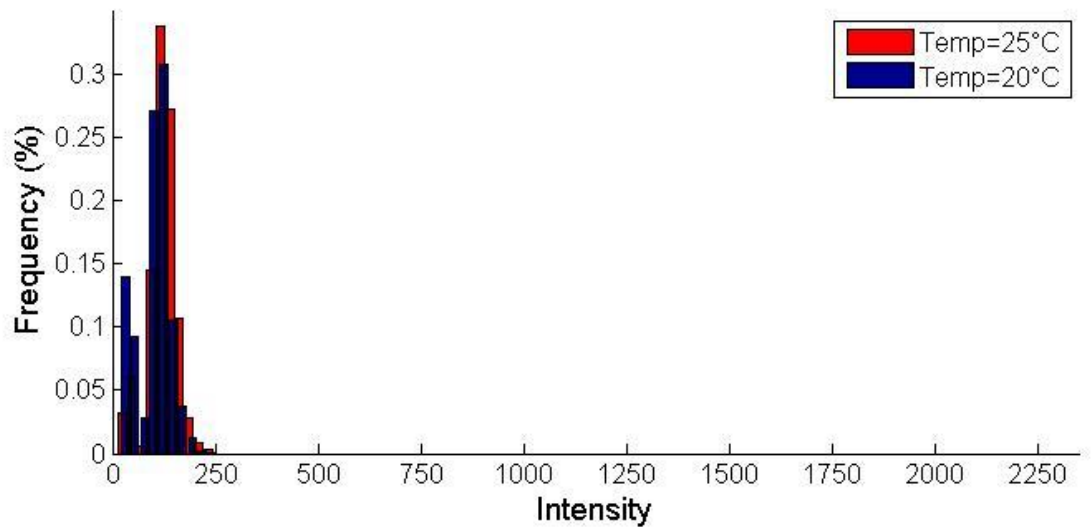


Figure 3.16 The histogram based on simulation results of *tph-1* expression in *unc-43(lf)* at 20 °C and 25 °C. The profile here also fits the experimental results.

3.6.2 Analysis of distribution of isolated mutants

To analyze the phenotypic changes in isolated mutants, we re-created the phenotypic space based on coefficient of variation (CV) in *tph-1* expression levels by single parameter variation. CV is a normalized measure of dispersion of a probability distribution. In Fig. 3.17, simulation results are compared to experimental CV of putative mutants that have negligible temperature changes by statistical analysis ($p > 0.01$). Based on Fig. 3.17, we observed that large population variations in expression levels is not produced in the stochastic models, suggesting that the mutations are not in the pathways captured in the current model. Thus, we suggest that changes of parameters for downstream of CaMKII and CaN pathways can produce only narrow distributions in populations, and these mutants should be sequenced first.

As we discussed in section 3.5.2, the regulations upstream of CaN (and CaMKII) and possible additional feedback need to be considered to understand all phenotypic characteristics of double mutants. Also, further validation is required for parameters and system robustness.

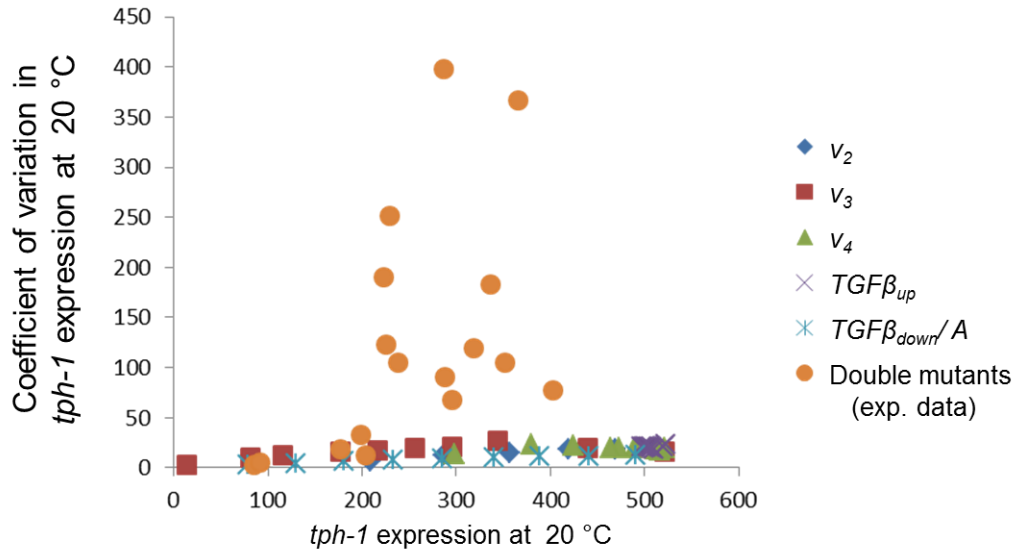


Figure 3.17 The simulation results of coefficient of variation (CV) in *tph-1* expression at 20 °C and 25 °C by changes of each parameter. Each line indicates the possible changes by each parameter variation. Orange circles represent experimental results of mutant alleles that have negligible temperature dependency based on statistical analysis ($p > 0.01$). Only seven of them exist within the allowable narrow range generated by changes of parameters from the optimal values (see section 3.4.2)

3.6.3 Stochastic models for characterizing wild-type phenotypes

The stochastic effects considered here can also be useful in characterizing wild-type phenotypes. Fig. 3.18 shows that *tph-1* expression at 25 °C having large deviation compared to that of *unc-43(gf)* mutant. It is possible that 1) switch-like behavior of CaN and CaMKII due to different association constant to Ca^{2+} levels, 2) their crosstalk, and 3) the feedback regulation could induce this large variation. To simulate the distribution of *tph-1* expression in wild-type, we roughly selected the parameter sets in Tab. 3.5. Using these parameters, we were able to obtain the

simulation results in Fig. 3.19 that mimic the experimental data.

Table 3.5 Parameters obtained for stochastic effects in CaMKII activity.

k_1	0.65
CaMKII ^{pos}	5
crosstalk	0.15

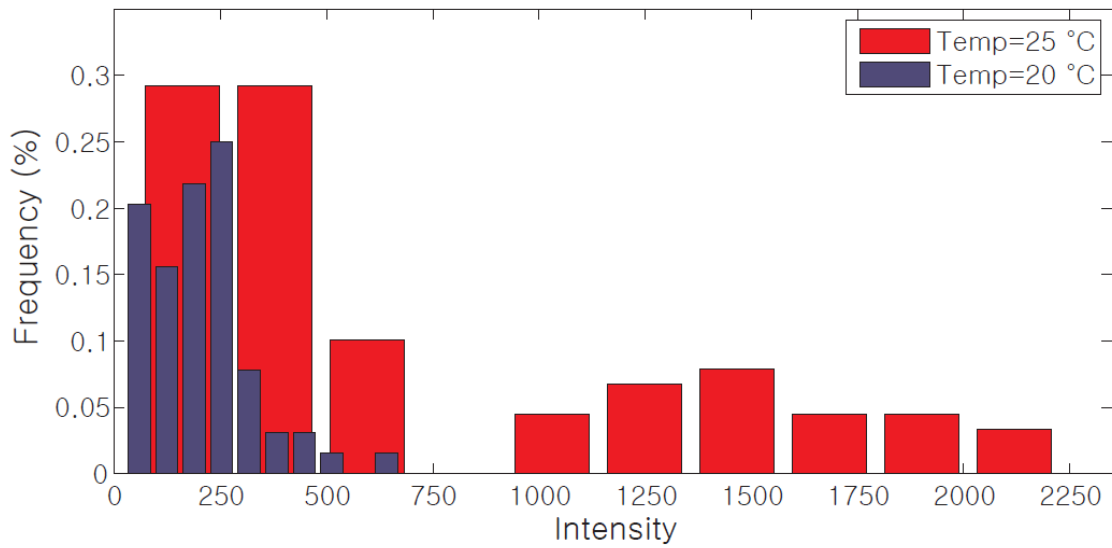


Figure 3.18 The histogram of experimental results of *tph-1* expression in wild-type at 20 °C and 25 °C.

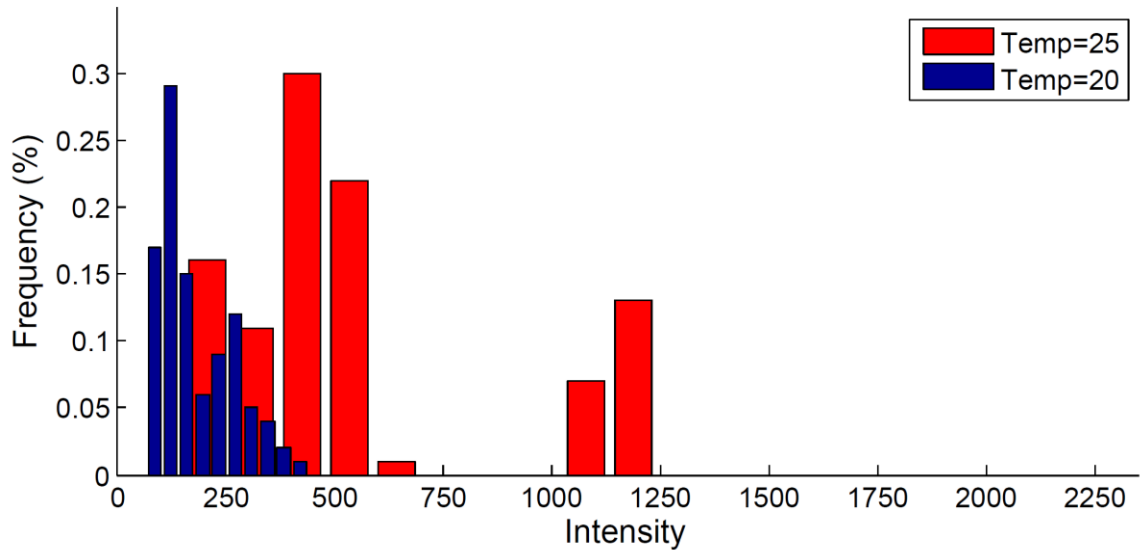


Figure 3.19 The histogram of simulation results of *tph-1* expression in wild-type at 20 °C and 25 °C. The parameters are optimized roughly to consider experimental results of *tph-1* expression 20 °C and (especially) 25 °C

3.7 Conclusion

Here, we developed and analyzed the model as a set of coupled ODEs to account for UNC-43-dependent regulatory network of *tph-1* expression in response to the environmental factors. This simulation allows us to probe the detailed mechanism of *unc-43* signaling pathway for transducing thermal stress to *tph-1* transcription. Using the steady-state model, we compared the average expression levels of *tph-1* at 20 °C and 25 °C under various mutant backgrounds. Based on simulation results, we suggested some plausible phenotypic changes of mutation in downstream of CaN and CaMKII. By considering variations in expression level of experimental results, it is possible to prioritize the target mutants whose expression levels of *tph-1* are not much changed at different temperatures. In contrast, mutants showing large variations of

expression levels at two temperatures are possibly perturbing the regulatory mechanism in upstream (or possibly parallel) of CaMKII and CaN activities because their behavior cannot be explained with the current model even when the parameter space was largely explored. In addition, we used the stochastic computation to characterize the individual differences, which also can contribute to the environmental responses. It is possible that we can manipulate the phenotypic changes in wild-type by incorporating dynamics regulatory activities of CaMKII and CaN.

3.8 Future work

3.8.1 Testing hypothesis of bistability

Some modeling studies have shown that a system including CaMKII and associated pathways could be bistable in a range of calcium concentrations.[25-27] To test hypothesis of bistability in this system, we need to measure the expression level of *tph-1* cultured at intermediate temperature in between 20 °C and 25 °C.[28] Otherwise, one should track the dynamic response of *tph-1* expression levels as a function of temperature. In the preliminary experiments, we monitored the changes of *tph-1* expression after shifting culture temperature from 20 °C to 25 °C for 9hr (Fig. 3.20). First, we cultured animals at 20 °C about 3 days to reach day 1 adult, and imaged them (t=0 in Fig. 3.20). Then, we transferred animals to 25 °C incubator, then cultured, imaged, and finally quantified the expression level of *tph-1* at 3, 6, and 9 hr after shift. However, we observed that the changes in *tph-1* expression are not rapid, and thus 9 hr measurement was not enough to reach new steady-state at 25 °C. Thus,

as a future work, we will increase the time of observation (>24hr) and compare temperature shift study to dynamic aspects of the model to test bistability.

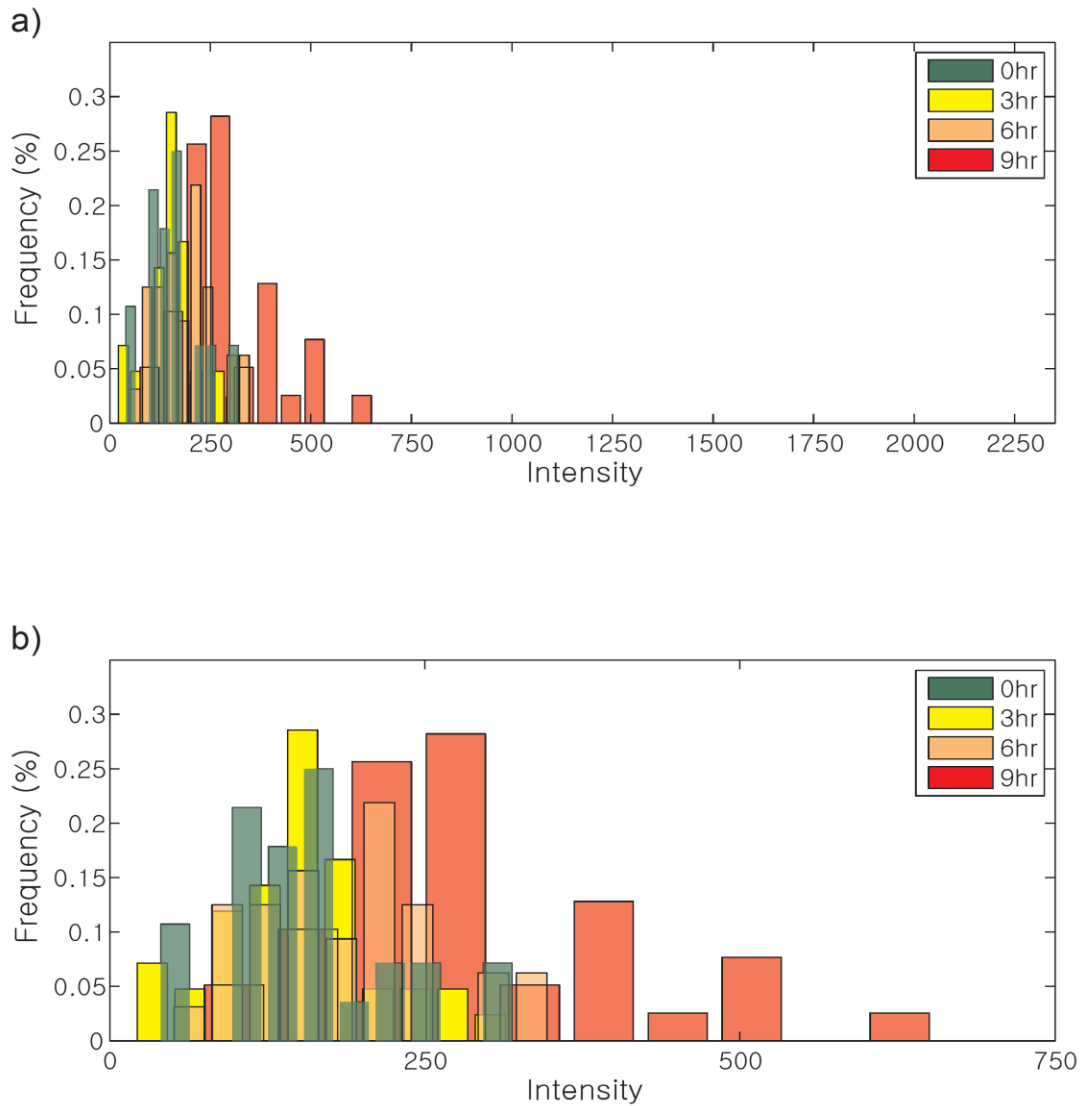


Figure 3.20 Preliminary results of temperature shift experiment (20 °C to 25 °C). Animals are initially cultured at 20 °C to become adults; here, we used this as a reference (0hr) before the shift. Every 3 hr after shifting temperature, the expression levels of *tph-1* were measured. b) zoom-in view of a) to visualize the temperature dependent distribution changes.

3.8.2 Incorporation of Ca²⁺ signaling pathway

To measure the dynamic response of *tph-1* expression with (or possibly without) temperature changes, we need to include regulatory network in upstream of CaN and CaMKII in model. The current model is developed based on the simple assumption of fixed CaMKII and CaN activity at each temperature. By using this model and comparing to experimental results, we found some likely mechanisms of regulators downstream from CaMKII and CaN. However, unless we incorporate this Ca²⁺ signaling network, we cannot simulate the dynamic response of *tph-1* expression. One possibility is to look into literature so that we can incorporate dynamic regulatory mechanism in CaMKII and CaN activities to our model.

Moreover, in addition to measurement of dynamic responses, Ca²⁺ signaling pathway needs to be considered since it plays an important role in regulatory mechanism of *tph-1* expression in wild-type and even in *unc-43(gf)* mutants. Some mutants are known to have defects in Ca²⁺ channels have shown interesting results.[8, 11, 27] For example, mutations in voltage-gated calcium channel (UNC-2) and ion channel Transient Receptor Potential Vanilloid (TRPV) result in different changes of *tph-1* expression. The *tph-1* expression in *unc-2; unc-43(gf)* double mutant is known to be very high, and we experimentally confirmed Estevez *et al.*'s observation (Fig. 3.21).[8] (We obtained this strain courtesy of the authors). However, the expression level of *tph-1* in *unc-43(gf); osm-9* is half rescued from *osm-9* single mutant; *tph-1* expression is very minimal in *osm-9*. [27] It is possible that this difference is caused by feedback regulation since TRPV is known to be involved in feedback loop. [5]

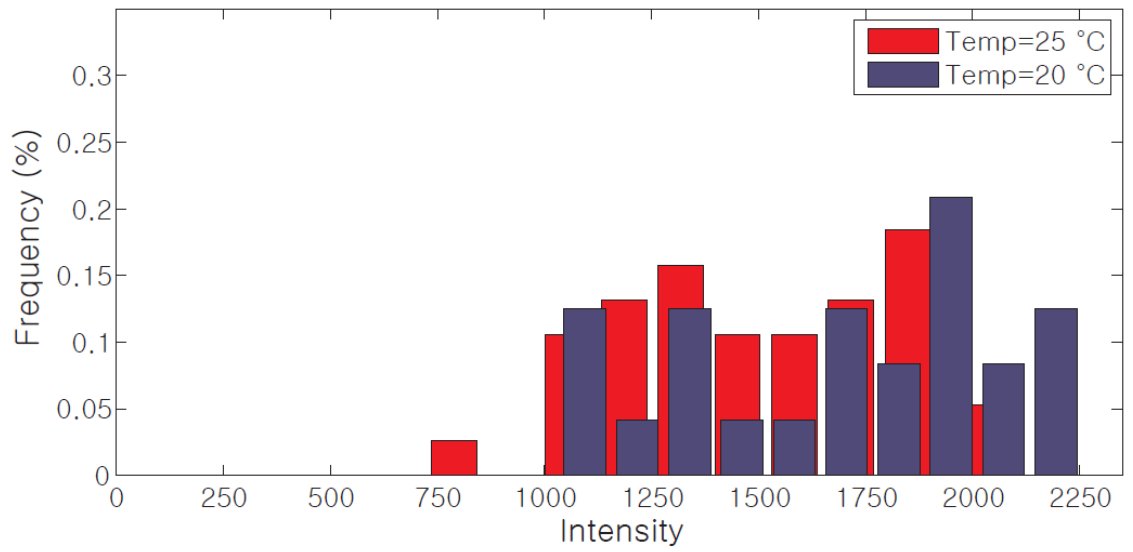


Figure 3.21 The histogram of experimental results of *tph-1* expression in double mutants: *unc2; unc43(gf)* at 20 °C and 25 °C. This experimental result agrees well with observation by Estez *et al.*[8]

CHAPTER 4

DESIGN AND CONSTRUCTION OF MULTI-CHANNEL DEVICE FOR HIGH DENSITY TARGET-SELECTIVE STIMULATION OF *C. ELEGANS*

Some of the KilleRed experiments are performed in collaboration with Shinae Kim in Dr. Lu's group.

4.1 Overview

To dissect the neuronal functions in multicellular model organisms such as *Caenorhabditis elegans*, selective ablation of neurons is extensively applied. For example, one of optogenetic tools, KillerRed, has greatly facilitated for selective ablation of cellular and subcellular features in a temporally and spatially precise manner. This powerful tool requires stimulating (5min-1hr), culturing (~24hr) and imaging (often repeatedly) a large number of individual animals. However, the existing methods cannot efficiently perform the entire procedure. Conventional manual microscopy allows optical irradiation on multiple animals simultaneously, but the overall process is very time-consuming and labor-intensive due to manual manipulation of the animals. In addition, the usage of anesthetics can damage animals' physiology. On the contrary, various microfluidic systems have been developed for each purpose (e.g. subcellular imaging, automated microsurgery, long-term culture or fast screening). However, the existing microdevices are not applicable for parallel selective illumination and continuous feeding during imaging and stimulation. To overcome these limitations, we developed a densely-

packed multi-channel device to enable simultaneous stimulation, long-term continuous feeding, and ease repetitive imaging over 100 worms. We verified the usability of the device for the high-throughput ablation with KillerRed-encoded worms. The ability of loading worms in identical location with high loading efficiency permits us to ablate selective neurons on multiple worms. We also observed cellular phenotypical changes for a day after optical ablation and investigated their behaviour changes after efficient recovery. We expected that our multi-channel device will be useful for long-term repeatable imaging and selective stimulation, and will greatly facilitate a broad range of developmental and functional studies in neuroscience.

4.2 Motivation and limitations of single-channel devices

Many microfluidic devices have been designed for stimulating and imaging of *C. elegans* to increase the throughput.[50, 51, 53, 54, 56, 71-76] For example, Chronis *et al.* reported the device which enables imaging neuronal activities in response to chemical stimulation to characterize their function.[54, 56] Even though most microfluidic devices have superior abilities to handle animals than manual methods, most chips consist of a single trapping channel, which is not beneficial in long-term processes such as optical stimulation and on-chip culture. Additionally, the fabrication processes and their operations are relatively complex, because most devices are based on controls of active components on- or off-chip.

In contrast to single-channel designs, multi-channel devices have increased the throughput of imaging *C. elegans*. [53, 57, 58, 77-79] Hulme *et al.* created the 128 channels to trap and image animals [78] and applied it (16 channel-version) to track

the changes in body size and locomotion for the entire adult lifespans.[57] Although the process of loading *C. elegans* is very simple and fast, the channels of this device are not closely packed and worms are not loaded in identical location. Thus, it is difficult to illuminate multiple worms at the same time, which cannot facilitate the time-consuming optical manipulation process. Moreover, while the tapering channel enables immobilizing animals for imaging at high resolution, the clasped features restrict food and chemical delivery to the worms while they are in the channel. This type of design, therefore, is unsuitable for long-term optical activation/cell kill and imaging.

Altogether, the existing methods cannot efficiently perform the sequential procedures of irradiation and (repeated) imaging of a large number of animals in parallel with continuous delivery of bacteria. To overcome these limitations, we developed a multi-channel microdevice for simple and rapid loading, trapping, stimulating and imaging worms. The advantages of the design of microfluidic device developed are as follows: (1) trapping channels are densely packed allowing multiple worms to be stimulated and imaged simultaneously, which enables the high-throughput analysis; (2) the device does not include any active components, and thus its operation is simple and does not require any expensive and complex external components; (3) chemicals, media, and bacteria can be easily delivered in a controlled manner, which is feasible for long-term observations; (4) it is easy to recover worms from the device to investigate their physiological outcomes regulated by target neuron activities; (5) The device operation is robust with negligible possibility of clogging since the size of main channel is much larger than the width of *C. elegans*;

Furthermore, the device is not limited to use in optical surgery of high-density worms, but it can be applied to many versatile applications of imaging and stimulating *C. elegans*.

4.3 Materials and methods

4.3.1 KillerRed-expressed *C. elegans* strain

We used a KillerRed (KR)-expressed transgenic worm: *zDis5(Pmec-4::GFP), vdEx405[Pmec-4::KR; odr-1::DsRED2]*. All worms were fed with *Escherichia coli* (*E. coli*) OP50 on culturing agar plates and maintained at 20 °C based on standard culture conditions.[80] The hermaphrodite worms were synchronized to L4-stage before loading worms in the microfluidic device.

4.3.2 Fabrication of devices

All microdevices were fabricated in polydimethylsiloxane (PDMS) (Dow Corning Sylgard 184, Midland, MI) by soft lithography.²⁶ The master molds were fabricated with a negative photoresist, SU8-2025 (Microchem, Newton, MA) by UV photolithographic processes. Before molding process, the surfaces of 45 µm-thick patterned wafers were treated with tridecafluoro-1,1,2,2-tetrahydrooctyl-1-trichlorosilane vapor (United Chemical Technologies, Bristol, PA) to allow release of PDMS from the masters. To obtain ~1 mm-thick layer, a PDMS mixture of A and B in 20:1 ratio was poured on the mold after removing air bubbles, and then partially cured at 70 °C for 15 min. On top of the first layer, a PDMS mixture in 10:1 was poured to obtain ~5 mm-thick second layer for mechanical integrity.[58] After fully curing the mold at 70 °C for 2 hours, the whole PDMS layer was peeled off and devices were cut into shape. For fluidic connections, two holes (one inlet and one outlet) in

individual devices were punched with 19 gauge needles (McMaster-Carr, Elmhurst, IL). Finally, all devices were bonded onto either a slide or cover glass by plasma bonding.

4.3.3 System operation and bacteria preparation

For each experiment, the microfluidic device was filled with M9 solution to remove air bubbles. Then, worms were delivered with M9 solution into device at a flow rate of 2.5-3.5 ml/hr using a syringe pump. For feeding *C. elegans*, bacteria OP50 were cultured at 37 °C for 16 hours shaking at ~200 rpm. To inactivate the bacteria, these cultures were spiked with Streptomycin (50 µl/ml final concentration). After spinning down the bottles at 4500rpm in a refrigerated centrifuge set at 4 °C for 20 min, supernatant was discarded and pellet was resuspended with a mixture of S-basal, Streptomycin(50 µg/ml), and Carbenicillin (50 µg/ml) to reach OD₆₀₀=10. The mixture including bacteria was flowed into the device in 2-3 ml/hr usually for a day. To recover animals from the device to characterize the physiological outcomes, M9 solution was introduced from the outlet (backflow) at a flow rate of 5~10 ml/hr and worms were collected from the inlet of the device.

4.3.4 Microscopic setup for optical ablation and imaging cells

Two different types of microscopic systems were used for optical ablation. High-throughput ablation was performed with whole field illumination on a fluorescence dissecting scope (Leica, MZ16F) with 2x objective for 2 hrs. To kill the target cells by KR activation, green light was illuminated for an hour. The green light was filtered with TXR filter (green light: 560/40 nm).

For the selective optical ablation, a modified LCD projector system was

employed.[81] The green color of the LCD projector (Hitachi, CP-X605) was modified with a green filter (568/50 nm band-pass) and emission lights were measured with Hamamatsu EM-CCD camera (512 x 512 pixels) on a fluorescence scope (Leica DMIRB). Two objectives (4x and 10x) were used for selective optical ablation. For selective illumination on multiple target regions, a LabVIEW program was made to create and control multiple regions of interests (ROIs). Green light was illuminated on the selected ROIs for an hour and blue light was applied to measure the change of target GFP signals 24 hours after illumination. The GFP signal was monitored with 4x objective for cell body observation and 20x objective for cell body and axon observation.

4.3.5 Computational Fluid Dynamics

To characterize the fluid dynamics in the device according to the channel geometry, three-dimensional fluid flow model was developed using Computational Fluid Dynamics (CFD) module of the finite element modeling software, COMSOL (Stockholm, Sweden). To simplify the numerical simulations, 3 x 3 or 20 x 3 array formats were used. Incompressible steady-state Navier-Stokes equations were solved to obtain the velocity profiles. Inlet pressure was set to obtain a volumetric flow rate equal to the measured value, and outlet pressure was fixed at atmospheric pressure. In the simulation, the value of density was 1000 kg/m^3 and dynamic viscosity was $8.90 \times 10^{-4} \text{ Pa}\cdot\text{s}$ based on the property of water at room temperature.

4.3.6 Behavior assay

To perform the classical mecahnosensory behavior assay, ablated or unablated control worms were placed on smooth agar surface of testing plates one day after illumination. The testing plate was prepared as a standard agar plate without OP50 bacteria layer to prevent food-driven behavior. Eyelash was used to deliver gentle touch to the anterior (just behind the pharynx) and posterior (just before the anus) worm bodies[82-84], which triggers backward and forward locomotion in unablated wildtype worms, respectively.

4.4 Results and discussion

4.4.1 Design of microfluidic device

In order to stimulate and image a large number of animals in a high-throughput manner, we developed a simple high-density multi-channel microdevice (Fig. 4.1). This one-layer PDMS device includes 140 densely-packed individual channels in 20 (column) x 7 (row) format to trap worms; it also allows for stimulating and imaging worms overtime. The array of these trapping channels is connected in each row by the serpentine channel and each row to the next (Fig. 4.2). Specifically, the serpentine channel (A) is 500 μm wide and carries worms and media throughout the device from the inlet, top-left-end of the serpentine channel, to outlet. The 40 μm wide trapping channels (C) fit closely with the size of young adults, which allows selectively stimulating target worms and neuroimaging to monitor the changes of neuronal activities. We minimized the space between neighboring trapping channels (~ 70 μm in a column) so that we achieved a density of 2.42 traps/ mm^2 , which is ~ 4 times

higher than what has been previously developed.[78] With 10x magnification, 6-7 trapping channels can be illuminated using multi-channel device while ~1 channel can be visualized for previous device.

Each trapping channel includes novel components to load and confine single animals efficiently to trapping channels, and deliver chemicals uniformly without active component controls (valves) (Fig. 4.2). At the outlet of trapping channel, 8 μm wide restriction channels (D) prevent worms from escaping and enable continuous flow to deliver flow and chemicals. Additionally, continuous flow across the restriction channel is fast enough to draw worms to the end of trapping channels, and help to position worms in relatively identical locations. Another key feature is the 300 μm wide resistance channels (E) between trapping and serpentine channels to make the bulk of the flows along the serpentine channel. To allow long-term (>10hrs) monitoring target worms, we designed the inlet of trapping channel to be small enough to prevent worms from escaping (B). We engineered its size as 25 μm wide to balance between maximizing loading efficiency and minimizing escaping of *C. elegans*.

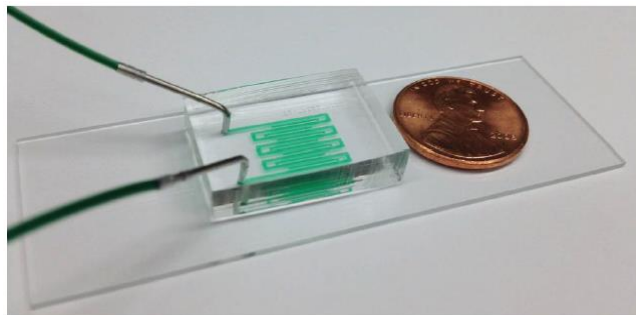


Figure 4.1 Optical micrograph of the high-density array device. The channels were filled with colored dye for visualization.

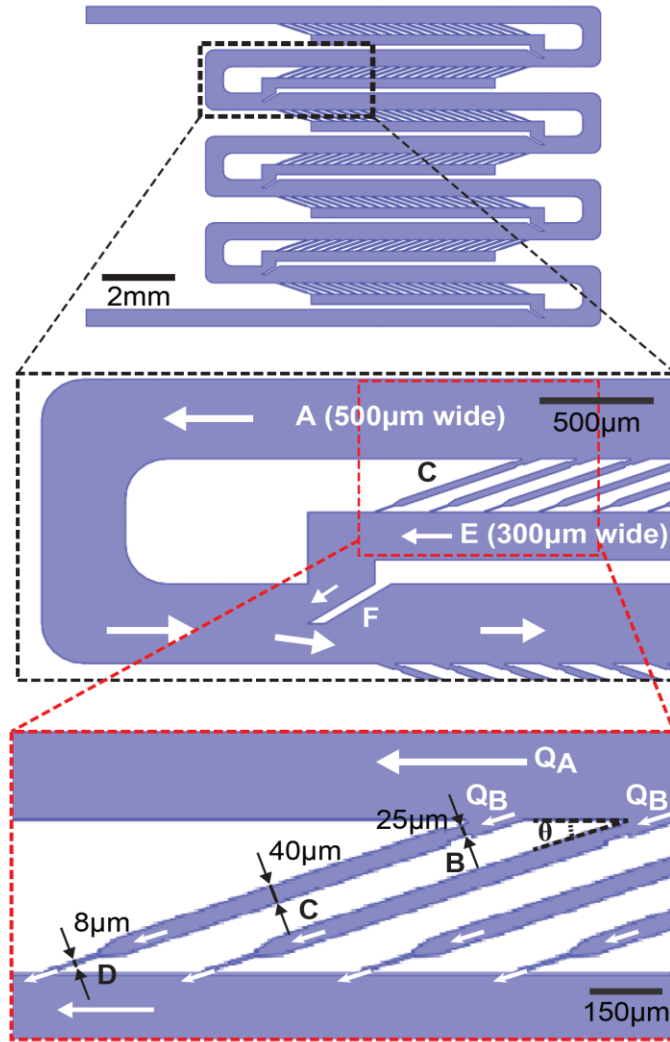


Figure 4.2 The schematics of multi-channel device showing the array of 140 trapping channels connected to the serpentine channel. Zoomed in views of the boxed region showing microfluidic components to enable efficient single-worm loading and continuous media delivery: A, serpentine channel; B, the inlet of trapping channel; C, trapping channel for imaging individual worms; D, restriction channels; E, resistance channels; F, slanted protrusion for fast recovery. White arrows represent the direction of flow which can carry worms and chemicals; specifically, Q_A represents stream flowing along the serpentine channel and Q_B indicates a stream into the trapping channel.

4.4.2 Simple and efficient trapping mechanism

These features enable rapid and efficient worm loading without the need of any active elements on the device; thus, the device operation is very simple and does not require any complex off-chip components. To minimize the variations in flow through the trapping channels and possibility of clogging, most of the fluid is engineered to travel along the serpentine channel; the small but significant enough flow across each trapping channel drags worms into the individual channels within a few seconds (Fig. 4.3a-d). On average, to fill most of the loading channels on each chip takes less than 30 min and loading efficiency is generally higher than 80% (Fig. 4.3e). Note that 100% is not possible because the animals have active locomotion, and thus they can swim against flow stream and tend to escape when geometrically restricted. Despite of this, we can achieve relatively high occupancy, which makes it possible to apply homogeneous optical and/ or chemical stimulation on densely-packed multiple animals in parallel. Also, it facilitates repeated characterization of specific cellular or subcellular phenotypes because the animals are regularly arrayed.

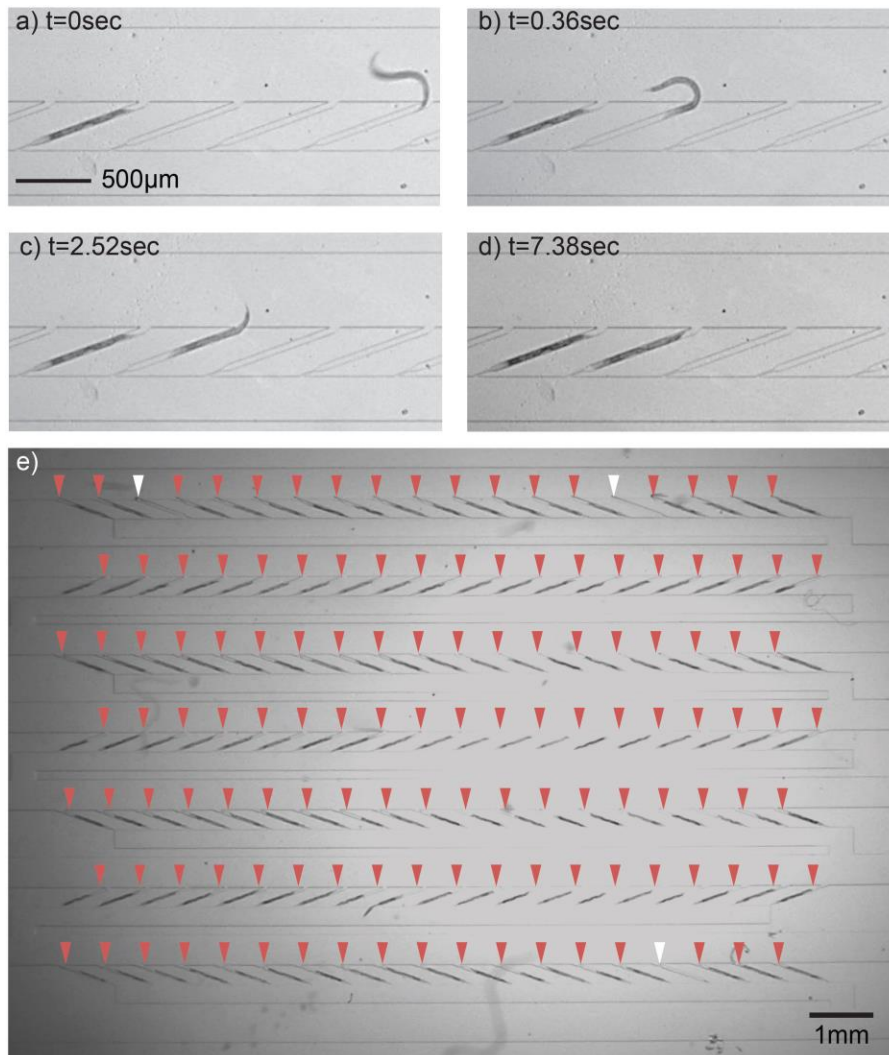


Figure 4.3 The Optical photographs showing *C. elegans* loading in the trapping channels. a)-d) Sequential images showing the single worm trapping in a channel in a few seconds. e) Optical photographs of the whole chip loaded with *C. elegans* (97.7% occupancy). Red triangles point at traps successfully loaded with single worms; white triangles at empty channels.

4.4.3 Loading efficiency depending on design geometry

Geometries were optimized in order to trap a single animal per a trapping channel efficiently, and thus to achieve overall high occupancy in array microdevices

(Tab. 4.1). Specifically, we empirically determined the optimal angle between the trapping channel and the serpentine channel (θ) (Fig. 4.4) by varying θ from 10° to 90° (Fig. 4.4a). We observed that small angles (e.g. 10° and 20° as shown in the data) show superior loading efficiency. In a previously published work[58], the angle (θ) is optimized as 20° because worms need to bend their body significantly to enter the channels if angles are too large. However, loading efficiency still depends on θ , even after we remove worms' mobility by the treatment of anthelmintic tetramisole (Fig. 4.4b). We hypothesize that the balance between a stream flowing along the serpentine channel (Q_A) and a stream directing the worms into the trapping channel (Q_B) affects the loading efficiency (Fig. 4.2). For validation, we characterize the flow ratio (Q_A/Q_B) based on fluid dynamics using finite element model (COMSOL) (Fig. 4.5). The more slanted the imaging channel, the higher the ratio of flow rates, which correlates with higher loading efficiency. The analyzed data suggest that small angles are preferred for high loading efficiency because of flow rate balance as well as the movement of *C. elegans*.

In contrast, the head-tail orientation of the loaded worms depends more on worm's locomotion ability and the overall flow rates (Fig. 4.6a and b). Head-bias is important for housing worms for a long time in the trapping channels because worms oriented tail-first tend to escape more easily. In addition for optical stimulations, relatively uniform head-tail orientation reduces the complexity of selective illumination since cells of interest can be easily identified without having to scan through the entire worm. Specifically, in the case of the field of view is smaller than the illumination area; since worms locate in the relatively identical positions, we can

roughly target the neurons of interest based on channel locations. Thus, to maximize the head-bias loading efficiency, the flow rate is optimized as 2.5-5ml/hr in addition channel angle is preferred in 20° .

Table 4.1 Design considerations for optimal operation

	Small	Optimal	Large
Trapping channel	Low loading efficiency	~size of target worms (young adults)	1) High possibility for multiple worm loading 2) High mobility of trapped worms → inhibit imaging and selective stimulation
Width of serpentine channel	High susceptible for clogging	>> width of worm < length of worm	Low loading efficiency
Height of serpentine channel	1) Inefficiently deliver worms 2) High susceptible for clogging	slightly higher than the size of target worms	Low loading efficiency
Restriction channel	Low loading efficiency	~8 μ m	Easy escaping

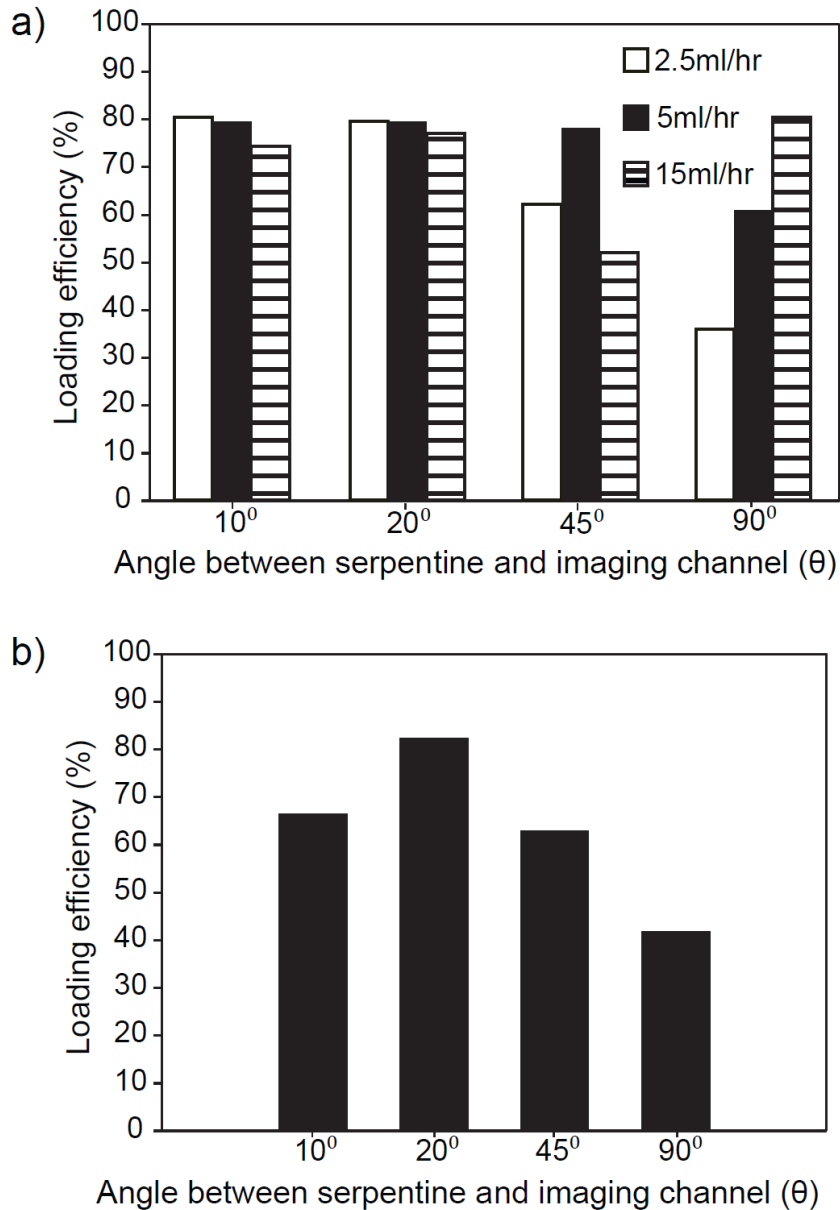


Figure 4.4 Loading efficiency optimized with channel geometry, particularly angle between the trapping channel and the serpentine channel (θ). a) The bar graph showing the channel occupancy as a function of channel angle and flow rate. b) The graph representing the loading efficiency of *C. elegans* with 1mM tetramisole to remove worms' mobility.

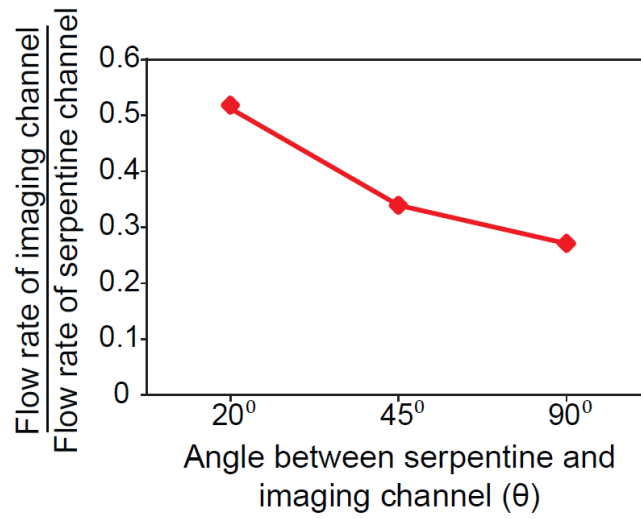


Figure 4.5 The plot of the flow ratio between serpentine and imaging channel at different angles based on COMSOL simulation.

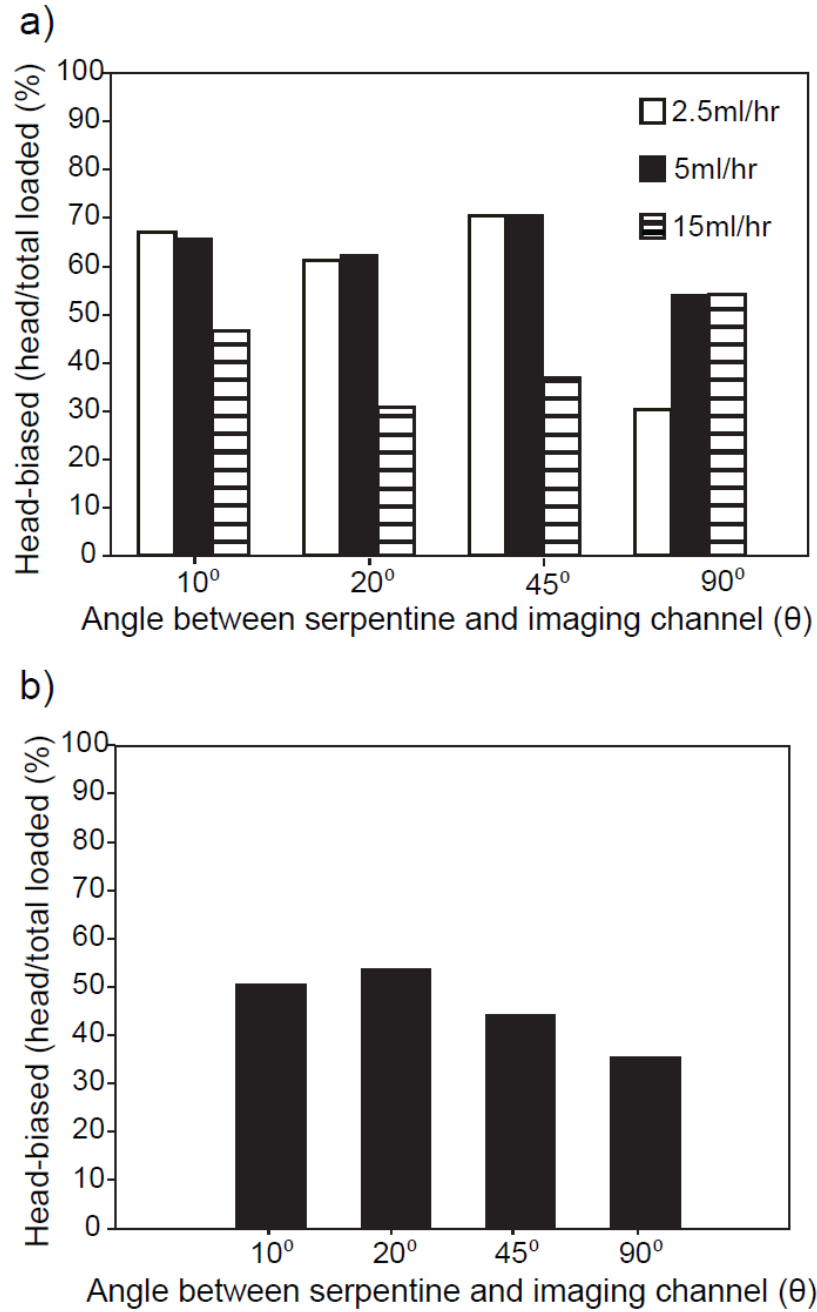


Figure 4.6 The orientation of loaded worms depending on flow rates, the mobility of animals, and angles between the trapping channel and the serpentine channel (θ). The bar graphs showing the head-bias of trapped animals a) without and b) with 1mM tetramisole.

4.4.4 Easy recovery without damaging animals

To analyze the physiological changes and investigate the function of specific neurons, one typically needs to recover worms; here we recover the worms from the device by applying flow in the reverse direction. To enable fast and efficient recovery of animals, we constructed the slanted protrusion (F) at the end of resistance channel (Fig. 4.2). It prevents worms from swimming to resistance channel, so that worms can travel through the serpentine channel (Fig. 4.7a). In the case of no slanted protrusion, worms can be easily re-trapped to resistance channel during recovery (Fig. 4.7b, c). If worms go into the resistance channel, it is hard to recover them by simply applying flow in the reverse direction because it is almost impossible for them to pass through the narrow restriction channel connecting resistance and serpentine channels (Fig. 4.2 and Fig. 4.7c). For recovering worms in the resistance channel, one option is to apply flow back-and-forth; however, this is really time-consuming. With slanted wall, we successfully recovered more than 90% of trapped animals which is more than twice of recovery rate without the feature (Fig. 4.7d).

For efficient recovery of animals, the balance of flows needs to be considered. The COMSOL simulation showed that slanted wall changes the flow streams but still enough flow can go into the resistance channels (Fig. 4.7e, f). To inhibit for worms to be re-trapped into resistance channel, most flow needs to be engineered to travel through the serpentine channel; meanwhile, still significant enough flow is required to be delivered to resistance channel to push worms in the trapping channels. Thus, we were successfully able to recover worms within a few minutes.

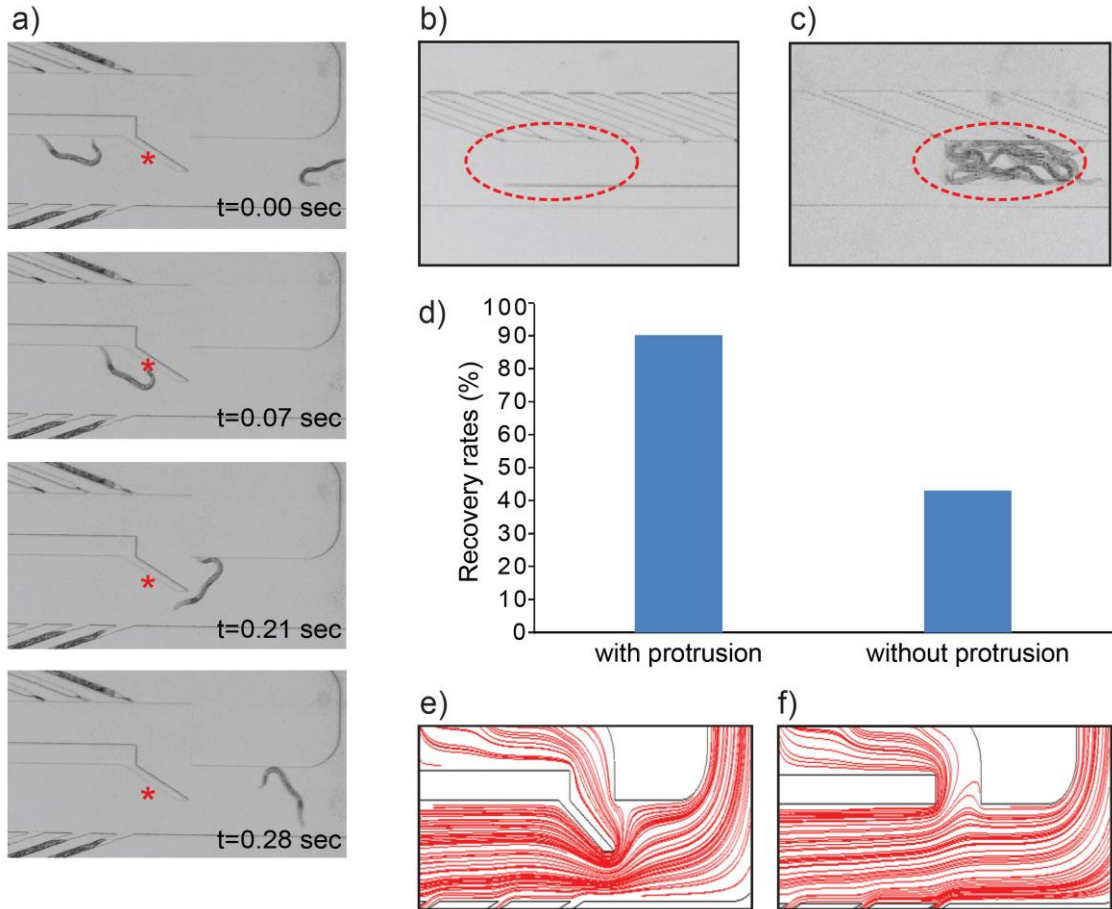


Figure 4.7 The slanted protrusion enables high-throughput recovery of animals. a) Sequential images showing the efficient recovery of animals. Worms are prevented from swimming into resistance channel while traveling along the serpentine channel. Red star indicate the protrusion feature. b) The bar graph showing the comparison of recovery rates with and without slanted wall. c) Representative image of empty resistance channel showing the successful recovery due to protrusion. d) Optical photograph showing the animals re-trapped to the resistance channel after recovery in the case of no slanted protrusion. e) and f) plots showing the flow stream lines e) with and f) without protrusion wall using COMSOL simulation.

4.4.5 Controlled delivery of chemicals, media, and bacteria

One of the advantages of this microfluidic platform is the ease of delivery of chemical and bacteria. Chemicals can be easily delivered to each worm in the imaging channel and switched within a few seconds (less than 10sec) in a controlled manner (Fig. 4.8), which could be useful as a chemical pulses for a temporal stimulation. Since worms are slightly smaller than the size of trapping channels, continuous flow was maintained through the trapping channel. To confirm the continuous delivery of channels occupied with worms, we imaged dye delivery and observed that chemicals can be continuously delivered to each worm in the trapping channel in a controlled manner. This continuous delivery is essential for bacteria supply on chip to avoid starvation. In addition, while culturing, continuous flow enables imaging individual worms even after laying eggs because it removes the newly-hatched progenies through the narrow restriction channels that adults cannot escape (data now shown). Moreover, flow mainly travel through the wide serpentine channel, which is useful in the uniform delivery of bacteria to trapped worms. To verify the successful food delivery to trapped worms, we flowed suspensions of 1.21 μm -diameter fluorescent beads. From this test, we observed beads were ingested and accumulated inside *C. elegans* body, which implies that trapped worms can easily consume the bacteria delivered (data not shown). Also, in our experiment, we observed the regular pharyngeal pumping rates and the number of eggs laid after culturing animals in device for a day. Pharyngeal pumping is well correlated with the animals sensing the presence of food, and thus we conclude that the animals are feeding properly. [85] We showed that the delivery of bacteria enables culturing animals in the channels for

more than a day, which is beneficial in observing optical ablation or other long-term imaging in high-throughput since worms are not required to be transferred from observation agar pad to bacterial lawn for physiology.[86-89]

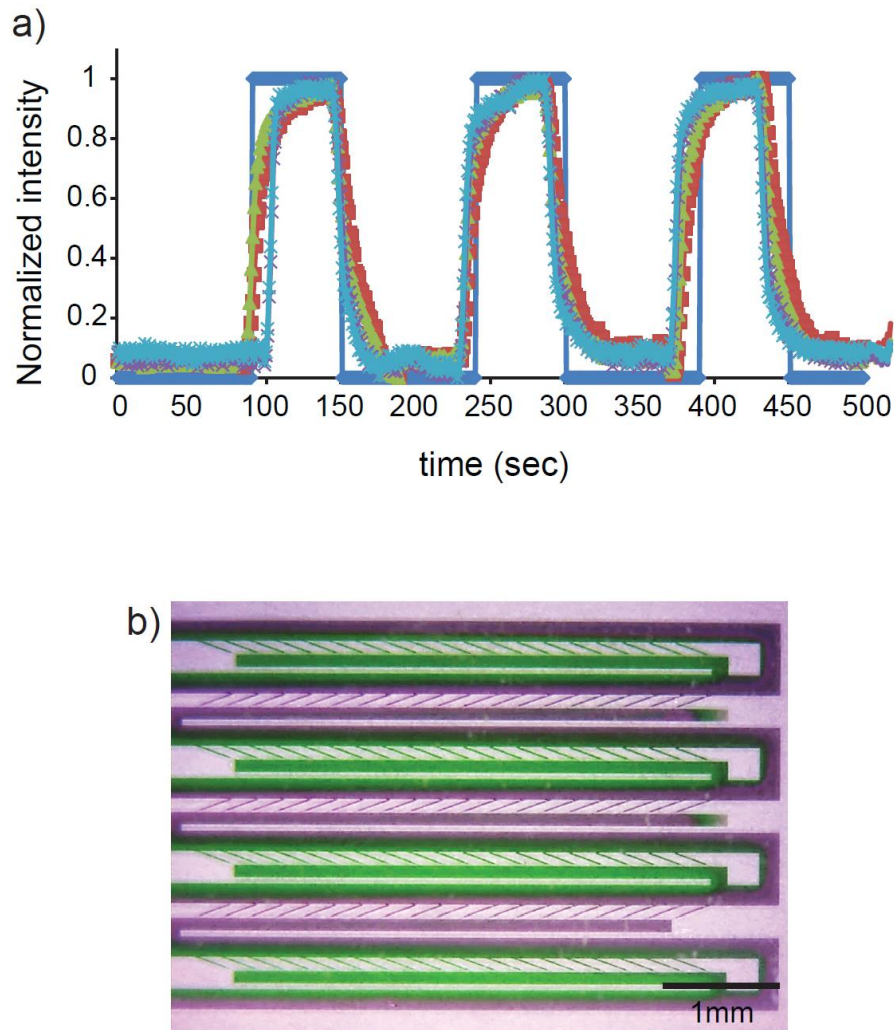


Figure 4.8 a) Temporal selective chemical delivery in multiple locations (including the channel in the first and last row) in a microdevice as a function of time. Channels were occupied with worms. Different color represents different locations in the device. b) Spatial-selective stimulation caused by tuning of the flow rates from two purple and green stimulants.

4.4.6 Parallel optical ablation of trapped worms

We showed that multi-channel device can successfully trap single animals with high loading efficiency (Fig. 4.3 and Fig. 4.4a). High trapping density of microdevice allows for high-throughput cell ablation of *C. elegans*. For the optical ablation experiments, we used wild-type nematodes expressing KR in the mechanosensory neurons: ALMs and PLMs (Fig. 4.9). The optical ablation technique with KR exploits the ability of ROS to damage any macromolecule within the genetically encoded target cells, when green light activates KR.[38, 39] Coupling with a green filter on the dissecting scope, we can kill all KR-expressed cells and monitor their changes in *C. elegans* on devices without expensive setup. To ensure the viability of target cells, we observed GFP signal of co-expression marker in the same cells. Fig. 4.9 shows GFP signals of ALMs and PLMs before and after KR activation with an hour irradiation. Twenty-four hours after KR activation, we found that GFP signals of mechanosensory neurons clearly vanished in the whole exposure area (Fig. 4.9b). Without illumination, all neurons were intact and had no damages including subcellular processes after a day (Fig. 4.11). By illuminating animals for 2 hrs at 2x magnification, we successfully ablated all KR-expressed neurons in the whole multi-channel device. In theory, we are able to ablate target cells in 140 worms at once, if all trapping channels are occupied with KR-integrated animals. In a manual experiment based on agar plates, we can also illuminate and ablate all KR-integrated cells in 30-50 animals at the same time. However, it is hard to identify individual animals and measure their phenotypic changes after optical activation. With our chip, we not only ablate multiple animals but also monitor individual degeneration

processes in parallel. Moreover, unlike manual methods, we are also able to eliminate the usage of anesthetics, which can be disruptive to developmental processes.

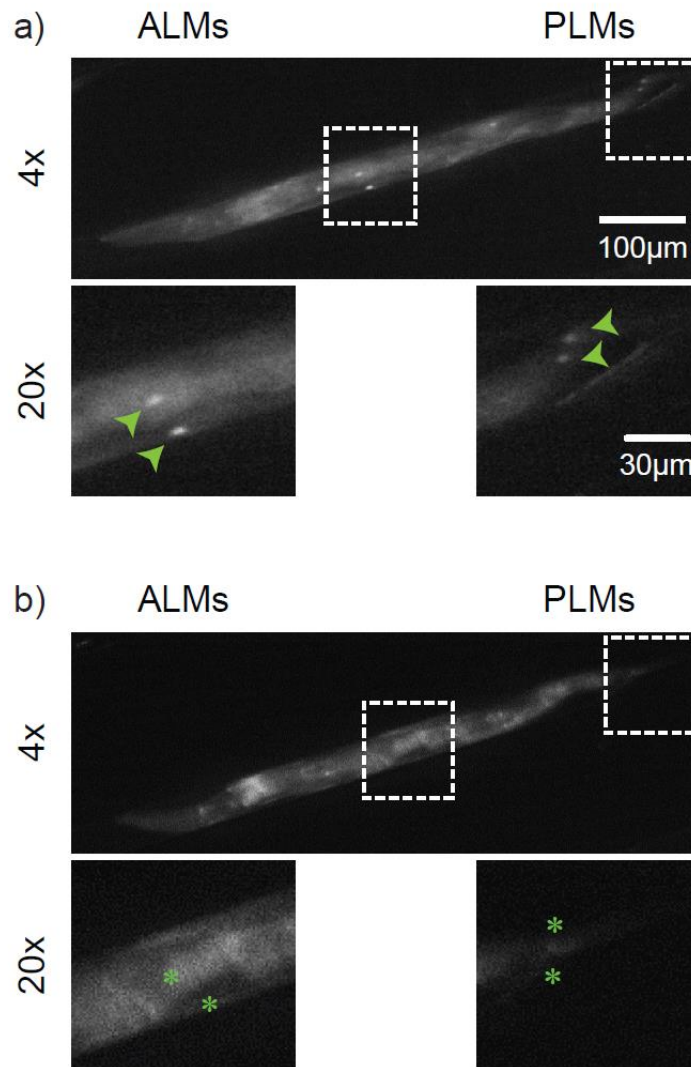


Figure 4.9 Fluorescent images of ablation on mechanosensory neurons of *C. elegans* in the device. The zoom-in views (20x) of each boxed region showing GFP signals of ALMs and PLMs a) before illumination and b) 24 hours after illumination. Green arrowheads and asterisks represent GFP signals of undamaged neurons and their death, respectively.

4.4.7 Simultaneous selective ablation of target neurons and long-term monitoring

Another advantage of our multi-channel microfluidic platform is identical alignment of multiple worms with minimized the space between neighboring trapping channels. Due to these repeated trapping channels and continuous flow through the restriction channels, worms are positioned in predictable locations, which enable fast ROI selection for selective ablation without time-consuming pre-imaging process. To create ROIs, we used a customized LCD projector system similar to the system in Stirman et al.[81] Fig. 4.10a shows results of selective illumination on PLMs (marked with green arrow heads) of a trapped worm. We observed the target-cell death 24 hrs after illumination; in contrast, unstimulated ALMs (marked with white arrow heads) in the same worms looked unchanged. In the same manner, we monitored the selective defects on ALMs with ALMs-selective-irradiation without effects on PLMs. Under 10x magnification, we ablated target cells in 2-3 worms at the same time (Fig. 4.11). To increase the number of animals in single field of view for improving cell-ablation throughput, we can use illumination at lower magnification with higher intensity of the light source.

As discussed in previous section, our microfluidic chip also has advantages in culturing animals due to easy and continuous delivery of bacteria. To maintain the natural cellular activity preferably at physiological conditions, worms are required to be fed with bacteria during the degenerative process based on KR photo-toxicity, which takes ~ 24hrs after illumination. Also, even during illumination to activate KR especially when it takes more than 30 min, it is important to allow for feeding *C. elegans* to minimize physiological side effects; however, none of previously

developed platforms is suitable for long-term optical activation because of immobilization technique and media delivery. In our experiment, worms were fed during and after illumination and can survive more than a day on chip. To ensure that physiology is not adversely affected by on-chip culture, we measured and compared the relative pharyngeal pumping rate with and without food delivery (Fig. 4.10b). While the pharyngeal pumping rate with food is comparable with that of culturing plate condition (control), without-food condition shows dramatically decreased pumping rate. This suggests that animals are feeding properly on multi-channel device. The consistent long-term culture on this device can increase the throughput of overall experiment by eliminating repeated worm-transfer between culturing plates and ablation/observation pads.

This long-term culture on chip is also beneficial in tracking specific neurons in animals over time. To observe long-term phenotypic changes, we collected time-lapse images hourly after the PLM illumination for a day. Fig. 4.11 shows the results of time-dependent phenotypic changes for 19 hours on two sets of different worms: one with PLM illumination and the other with no stimulation. Interestingly, we observed different rates of cell deaths in a single PLM pair; one of the GFP signals was not observed after 6 hours and the remaining GFP signal disappeared after 9 hours (Fig. 4.11 upper row, right worm.). Moreover, we also found that different degenerative speed between soma and axon. Both axon processes were not distinguishable within 2 hours in front of soma damages, whereas the somas remained over 6 hours or more (Fig. 4.11c upper row). In contrast, control worms show clear signals on their axons and somas for 19 hrs. These results demonstrate that our device is capable of

analyzing dynamic response in subcellular processes. Thus, this microfluidic platform can be applied to monitor multi-worms' degenerative or regenerative progress on subcellular level *in vivo*, which is useful in aging and neurodegenerative disease studies.

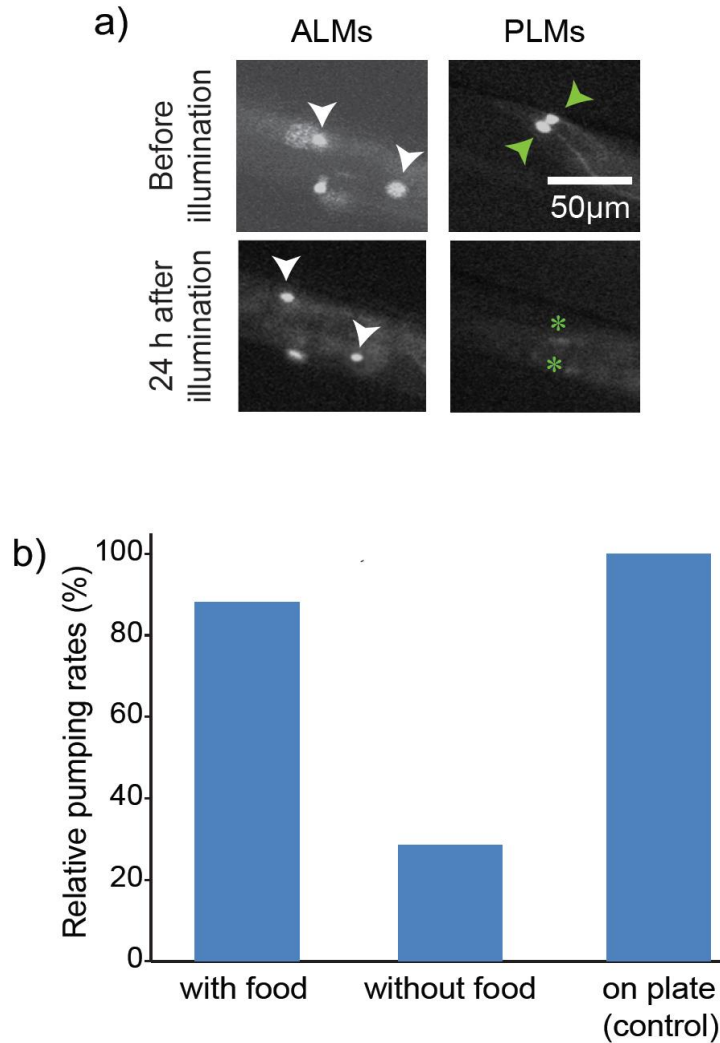


Figure 4.10 Selective neuronal ablation on the device. a) Fluorescent images of ALMs and PLMs of a single worm showing selective PLMs ablation. PLMs were illuminated for an hour with green light and imaged after one-day culture on the device. Green arrowheads and asterisks point to intact and vanished GFP signals on PLMs respectively; white arrowheads indicate control ALMs which has no changes. b) The bar graph showing relative pharyngeal pumping rates of worms with- (bacterial solution, $OD_{600}=10$) and without- food on chip, normalized to animals on standard agar plate with bacteria lawns (control). The pumping rates were averaged of three individual measurements.

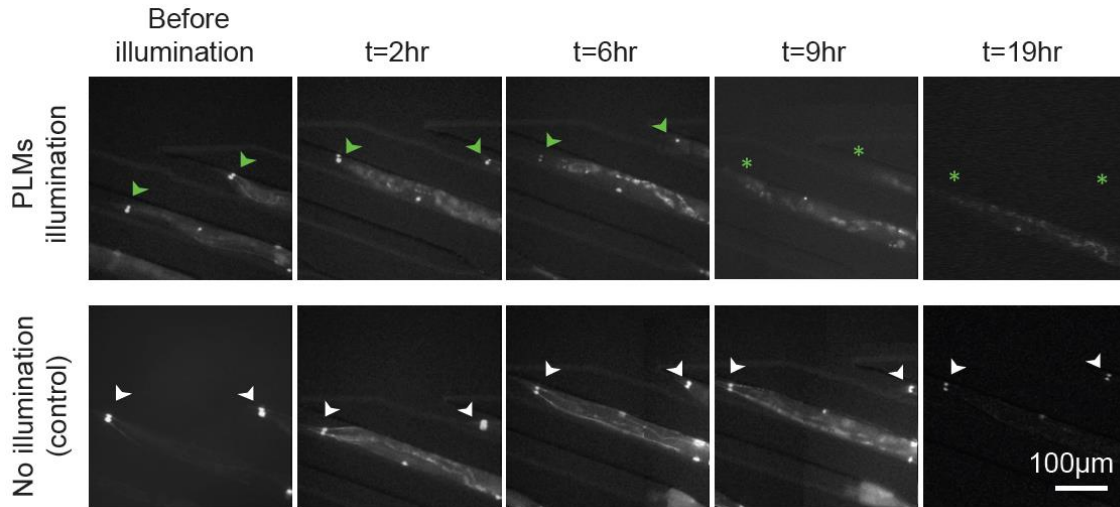


Figure 4.11 Time-lapse images of GFP signals of PLMs for 19 hours on two different rows after 1hr PLMs-selective illumination (upper) and without illumination (control, lower). The GFP intensity of illuminated PLMs decreases as a function of time, while all PLM signals have no critical changes without illumination. Arrowheads point PLM bodies and asterisks indicate vanished GFP signals on PLM bodies.

4.4.8 Post-illumination recovery and behavior assay

One of the advantages of array device, as we discussed, is ability to efficiently recover worms in simple way after experiments. Recovery of worms from the channel is important for verifying neuronal functions on behaviors. To easily recover animals in a high-throughput manner, we engineered the slanted protrusion walls in between serpentine and each resistance channel (Fig. 4.2 and 4.7). We observed that animals efficiently push away from the resistance channel, which enables fast recovery of animals without critical damage and worm loss (Fig. 4.7).

It is essential to analyze the physiological outcomes (e.g. behavior) of recovered animals for investigating the function of ablated cells. It has been shown

that mMechanosensory neurons, such as ALMs and PLMs, are the major sensory neurons that detect soft touches in the anterior and posterior of the body.[82, 84] The anterior and posterior touches cause worms to move backwards and forwards, respectively (Fig. 4.12a). As a proof of concept, we performed the classical behavior assay to examine the functional defects; we observed avoidance response by stimulating the touch receptor of the mechanosensory neurons. In the double-blind behavior assay, we verified that animals fail to respond to either anterior or posterior body touch with an eyelash. A worm showed halting or no accelerated forward locomotion after being touched posterior body, meanwhile the worm immediately showed backward locomotion after being touched anterior side (data not shown). After the behavior assay, we also reconfirmed the GFP markers in the mechanosensory neurons. When worm was insensitive on posterior stimulation, GFP signals were not observed on PLMs contrary to ALMs (Fig. 4.12b, c). In contrast, another worm showed no backward locomotion by touching anterior body, while the worm sensitively responded to posterior touching. When the worms were insensitive to the anterior body stimulation, GFP signals were not shown on ALMs only (Fig. 4.12d, e). These results are consistent with previous findings.[82, 84] Based on behavior test and GFP reimaging, it is evident that illumination on KR-expressed neurons disrupts their locomotion as well as cellular phenotypic changes. The results also showed that the device is capable for localized surgery and long-term culturing without functional damages as well as phenotypic changes on untargeted cells. Additionally, this observation indicates that recovered animals can be performed post analysis because they were not damaged by efficient and fast recovery process.

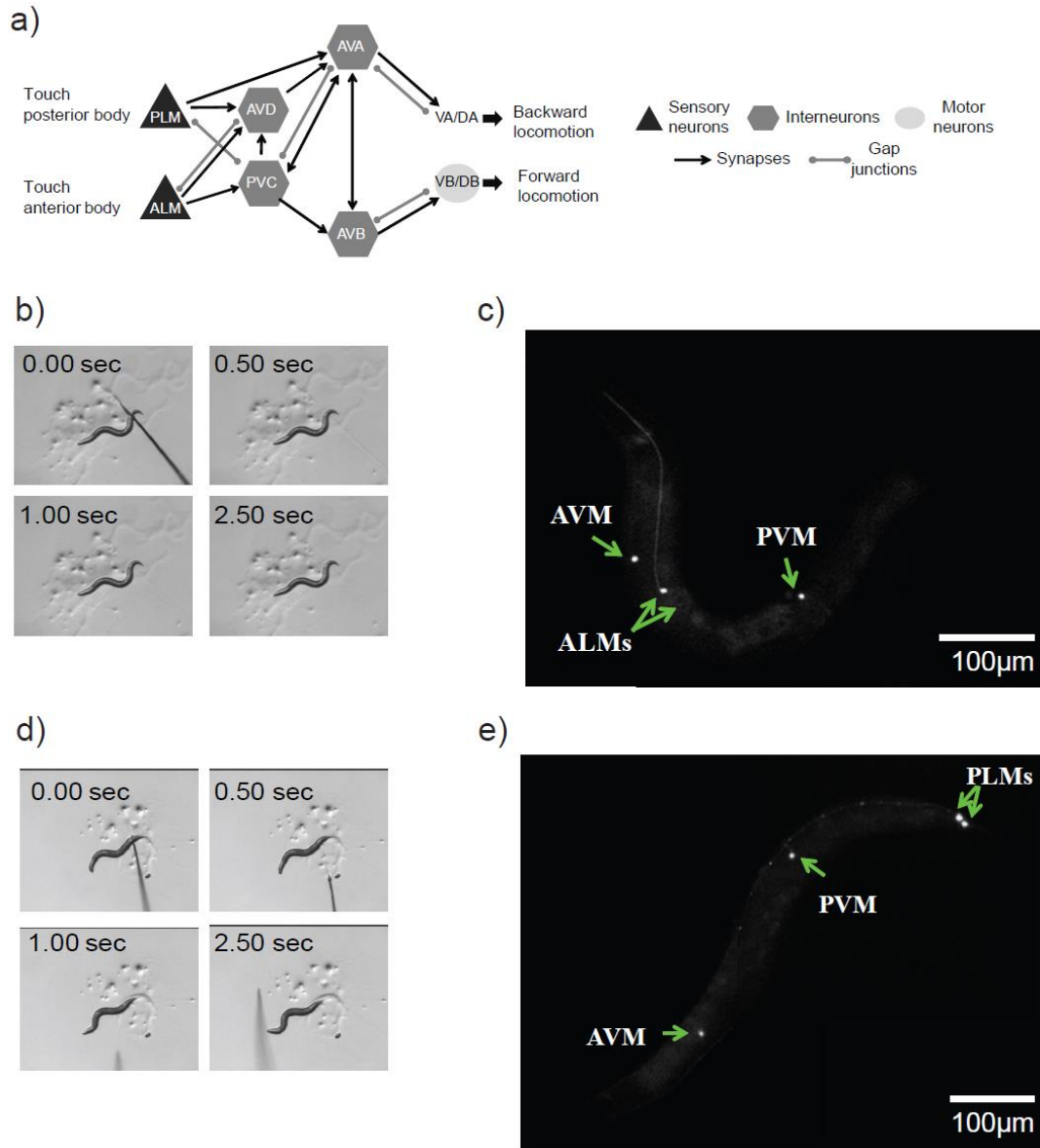


Figure 4.12 Functional verification of phenotypic changes by selective neuronal ablation. a) Simplified neural circuit from mechanosensation to behavior. The circuit is connected with synapses and gap junctions between individual neurons. b) Recovered worm failed forward locomotion when touched posterior body and c) its PLMs showing no GFP signals when re-imaged after blind behavior-test. In contrast, d) another recovered worm responded immediately when touched posterior body and e) re-imaging confirming its intact GFP signal on PLMs.

4.5 Conclusion

We developed a multi-channel microfluidic device that can load, trap, and image over 100 worms at the same time. Also, high-density array platforms are easy to promptly and selectively stimulate multiple targets without active elements. In addition, the continuous nutrient supply in the device enables both long-term imaging and irradiation. The ability of long-term monitoring in our device may be applicable to degenerative, regenerative, and developmental studies that require monitoring of transient response or time-lapse change. For example, it is easy to track the cellular and subcellular response (e.g. mitochondria distribution) to ROS over time. In addition, this controlled delivery has potential benefits in the supply of chemical stimulants to record neuronal responses such as calcium imaging and drug screening. Lastly, the ability of having safe and efficient worm-recovery in our device can be implemented in next generation study including functional behaviour test.

CHAPTER 5

THESIS CONTRIBUTIONS AND FUTURE WORK

5.1 Thesis contributions

The goal of this thesis was to develop robust and user-friendly microsystems for *C. elegans*, to use these systems and quantitative approaches to understand gene regulation and neurodevelopment in *C. elegans*.

The first contribution of this thesis is user-friendly and robust designs of microfluidics using hydrodynamics and single-layer designs. Even though microfluidics is increasingly popular in biological studies [1-6] with enhanced throughput of experiments and minimized human intervention, in almost all cases, its complex fabrication and operation limits widespread applications, especially for non-experts. The microfluidic device was created by optimizing an existing device developed by Dr. Matthew Crane (Lu lab, Georgia Institute of Technology). Through the development of single-layer chips, Dr. Crane and I reduced the fabrication burden (alignment and spin-coating processes) and time of fabrication process; moreover, we largely increased the reliability of the devices particularly during long and sustained operations (>24 hrs continuous use).

Using this general scheme, I developed the single-channel microfluidic device for imaging and sorting *C. elegans* to analyze genetic specification. This device operation is simple and achieves the throughput of up to 500 worms/hr, which is comparable to previous device operation and 1-2 order magnitude higher than conventional methods. Also, I developed multi-channel device for rapid trapping, parallel selective stimulating

(6-7 times higher throughput[7]), long-term (> 24hrs) culturing, and imaging (often repeatedly) a large number of animals (~140 animals at 2X magnification). The engineered microfluidic components achieve high loading efficiency (~ 80%) of regularly oriented (60-70% head-bias) and positioned worms in the high-density (2-3 time higher[7]) microarray without any active component, which makes its operation simple and efficient. Thus, the device developed is easy to use, even for non-experts without requirement of complex and expensive off-chip components. Both engineered systems will be useful in a broad range of genetic, developmental, and aging studies in neuroscience.

In addition, these tools were applied to address broad biological problems in neuroscience research. First, to quantify the gene expression levels, I modified and used quantitative analysis originally developed by Dr. Matthew Crane and Dr. Kwanghun Chung (Lu lab, Georgia Institute of Technology). It takes about a few seconds for image processing, which is comparable to other developed methods. To single-image analysis, I also incorporated tracking module to analyze sequential multiple images, which can be useful in tracking slightly moving animals (possible application is calcium imaging). Moreover, I developed for the first time an adaptive algorithm to define screening threshold based on the mutagenized population, not separate control populations measured prior to actual screening experiments, to account for stochasticity and day-to-day variations of gene expression. In this algorithm, the threshold is constantly updated to reflect the balance between maximizing sorting rate and minimizing false-positive rate.

I also developed a simple steady-state mathematical model that describes the genetic regulation of target expression that is regulated by rearing temperature. I

performed sensitivity analysis to measure the system output (here, the expression of a target gene) by parameter variation and use this information to create phenotypic space of parameters in specific parts of the pathways. Since changes in parameters may reflect actual changes in molecular behavior, the allowable range in the phenotypical space may potentially be useful in suggesting mechanisms of perturbations in specific pathways based on phenotypic characteristics.

I applied these technologies to identify the regulatory mechanism in tryptophan hydroxylase (*tph-1*), a key enzyme for serotonin synthesis. This thesis demonstrates for the first time the application of microfluidic system to quantitative screening for genes involved in the regulation of *tph-1* expression. I screened and identified 43 putative mutants using clonal imaging and statistical analysis; these genes may be potential targets for drugs to treat calcium-dependent serotonin deficient diseases such as migraine.

Additionally, I performed the selective ablation using the optogenetic tool KillerRed with incorporating multichannel microdevice developed in this thesis as another way to dissect the functions of nervous system. This analysis is performed in microdevice for the first time to enhance the throughput of entire process of illumination, culture, and (repetitive) imaging. I investigated both phenotypic and physiological changes (behavior test) induced by ROS-dependent degenerative process.

In summary, this thesis achieves the development of a few simple but efficient microdevices as well as quantitative analysis to allow high-content and complex interrogation into the nervous system of *C. elegans* both in regard to the genetic and the neural basis of phenotypic changes as well as physiological outcomes.

5.2 Future work

In this section, we discuss the possible application of technologies to improve the current system. In addition, the future work for modeling part is addressed in section 3.8.

5.2.1 Characterization of different responses from different cellular and subcellular features based on selective illumination

The collaborator, Dr. Massimo Hilliard (The University of Queensland, Queensland Brain Institute) use *C. elegans* as a genetic model system to study neuronal development.[8, 9] Paula Ramirez and Sean Coakley (Hilliard lab, The University of Queensland) constructed the KillerRed (KR)-expressed *C. elegans* strain (Chapter 4.3.1), and found that specific cell types are resistant to KR damage. Along with Dr. Shinae Kim (Lu lab, Georgia Institute of Technology) and Dr. Hang Lu, we also observed various vulnerabilities among mechanosensory neurons where KR is expressed with selective field of illumination using the projector system developed by Dr. Jeffrey Stirman (Lu lab, Georgia Institute of Technology).[10]

Both research groups have been investigating the intriguing possibility that some cells possess an intrinsic protection mechanism to ROS. One way to address this question is to identify the genetic components in ROS-dependent degenerative process as we performed the forward screening for *tph-1* regulation in Chapter 2. Based on preliminary screening about 1200 animals, we found some interesting putative mutants whose vulnerability is different from that of wild-type; i.e. the death rates of AVM and PVM are increased and/or the death rates of ALM/PLM are decrease. However, not all progenies of each selected mutants have the same phenotypic characteristics, probably because of

nature characteristics of non-integrated strains. Thus, further details of studies on these possible mutants should be followed.

5.2.2 Neuro-imaging responding to chemical stimulation using microfluidics

Another way to address the question in understanding how the structure and function of neural circuits regulate physiology is to record neuronal activity responding to external stimulation. The collaborator, Dr. Yun Zhang's (Harvard University, Department of Organismic and Evolutionary Biology) research has primarily focused on olfactory behavior and plasticity. Over the years, she has characterized the neuronal circuits encoding naïve and learned olfactory preferences.[11, 12] Calcium imaging is often applied to characterize the transduction of the activity of olfactory sensory neurons into downstream neurons.

For Calcium imaging is ideally performed in a microfluidic device to deliver temporal controlled stimuli to *C. elegans* and monitor neuronal activity in a controlled environment.[2, 13, 14] The developed microsystem is the excellent tool to trap animals and measure its dynamic response as a function of applied chemicals. However, this single-channel based device format often limits the throughput of the experiments, especially when we use calcium indicator transgene is not integrated; additional steps are required such as selecting target animals which have a calcium indicator before experiments. Additionally, the orientation of loaded animal is critical in this measurement; animals cannot be exposed and respond to chemical stimulus unless *C.elegans* is loaded with head-first orientation. In addition, even though the small channel that fits to *C. elegans* size inhibits its movement and enables the

measurement of dynamic responses, efficiency of immobilization is sensitive to animal size. Also, this small size channel sometimes inhibit robust operation due to clogging issues.

The current development of multichannel device can be an alternative tool to measure the target neuron activity efficiently. We have demonstrated that chemical delivery through the trapping channels is well controlled and can be switched within a few seconds (Section 4.4.5). Also, it is guaranteed that all trapped animals are exposed to delivery of stimuli because continuous flow is maintained even though all channels are occupied with animals. In addition, the sequential process of loading, imaging, and unloading a single animal can be converted to multiple animals in parallel, which would save the experimental time. To overcome one major drawback that animals are not tightly immobilized, we can use levamisole and image animals at low magnification. To measure the dynamic responses, we modified analysis code developed for quantifying gene expression levels (Chapter 2) to track the target neuron center over time-dependent images. We also optimized the experimental conditions to switch chemicals more efficiently and solved the photo-bleaching issues. If we can obtain the target strain of calcium indicator whose expression level is high enough to be observed at low magnification, we can extend our system to measure the calcium activity.

5.2.3 Imaging L1 stage (early developmental stage) of animals

As we discussed in Chapter 1, *C. elegans* is ideally suited for microfluidic manipulation because of its small size and has been extensively applied for various

biological studies. However, it is not easy to achieve robust operation of trapping and imaging animals since they can freely move and swim against the flow direction especially when they are stressed. In addition, worms can pass through the channels whose size is smaller than their body due to easily deformable cuticles. Moreover, it is more challenging to load and image smaller size of animals like L1 developmental stages and dauers. In addition, L1 animals often roll their bodies like coiled shape, which cause the decrease of loading efficiency. Current L1 imaging devices are high susceptible to be clogged even after using filters because of the small size and number of imaging channels.[15] However, array device has multiple trapping channels in one device, and clogging in one single channel does not fail the entire experiment.

For trapping L1 worms, we need to optimize all channel sizes, especially for restriction channels. Due to limitation of fabrication, we cannot incorporate restriction channels narrower than trapping channels. Thus, we need to use the two-layered channels to trap L1 animals in the multichannel format. The design for L1 device is compared to current version of device which is optimized for larger animals such as L4 and young adults (Fig. 5.1). Based on preliminary loading test, we observed that L1 animals can be easily trapped without clogging issues. Nonetheless, we observed that worms tend to escape easily from the trapping channels probably due to high mobility of smaller animals. If we can incorporate immobilization technique such as cooling and use of levamisole, we may inhibit their escape, and trap them for enough time to perform imaging. By using the developed microfluidic worm arrays, we can image a large number of worms and compare differences of gene expression pattern for worms in each developmental stage.

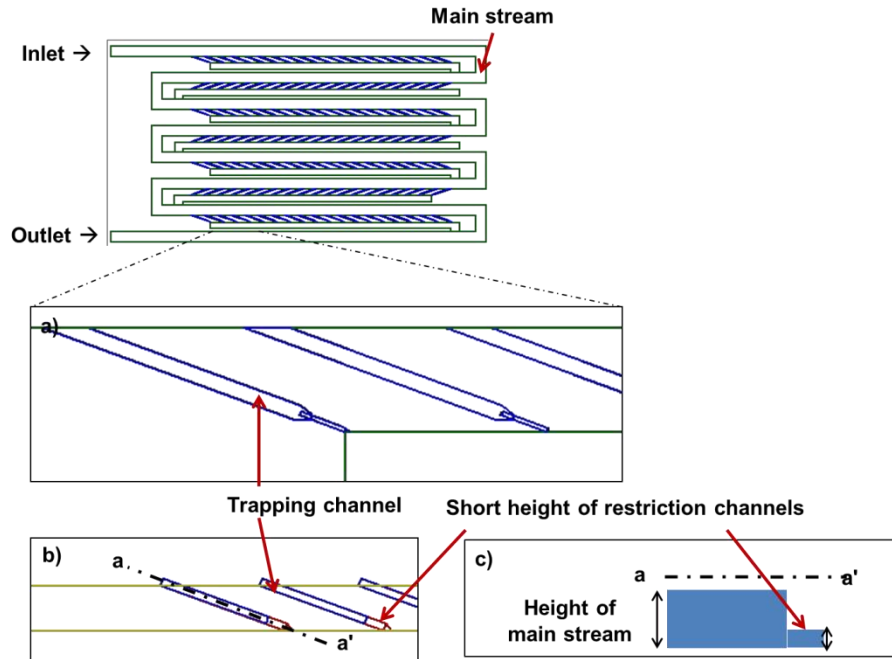


Figure 5.1 Design comparison of current version of device (optimized for L4 stage and young adult animals) and device for imaging L1 stage animals. Zoom-in view of trapping channels a) in current device and b) in L1 imaging device. c) Side-view of a-a' in b) representing the two-layered channel.

REFERENCES

1. Brenner, S., *Genetics of Caenorhabditis-Elegans*. Genetics, 1974. **77**(1): p. 71-94.
2. Grishok, A., et al., *Genes and mechanisms related to RNA interference regulate expression of the small temporal RNAs that control C-elegans developmental timing*. Cell, 2001. **106**(1): p. 23-34.
3. Ren, P.F., et al., *Control of C-elegans larval development by neuronal expression of a TGF-beta homolog*. Science, 1996. **274**(5291): p. 1389-1391.
4. Cassada, R.C. and R.L. Russell, *Dauerlarva, a Post-Embryonic Developmental Variant of Nematode Caenorhabditis-Elegans*. Developmental Biology, 1975. **46**(2): p. 326-342.
5. Garigan, D., et al., *Genetic analysis of tissue aging in Caenorhabditis elegans: A role for heat-shock factor and bacterial proliferation*. Genetics, 2002. **161**(3): p. 1101-1112.
6. Gerstbrein, B., et al., *In vivo spectrofluorimetry reveals endogenous biomarkers that report healthspan and dietary restriction in Caenorhabditis elegans*. Aging Cell, 2005. **4**(3): p. 127-137.
7. [Anon], *Genome sequence of the nematode C-elegans: A platform for investigating biology (vol 282, pg 2012, 1998)*. Science, 1999. **283**(5398): p. 35-35.
8. Watts, D.J. and S.H. Strogatz, *Collective dynamics of 'small-world' networks*. Nature, 1998. **393**(6684): p. 440-442.
9. Fire, A., et al., *Potent and specific genetic interference by double-stranded*

- RNA in Caenorhabditis elegans*. Nature, 1998. **391**(6669): p. 806-11.
10. Sonnichsen, B., et al., *Full-genome RNAi profiling of early embryogenesis in Caenorhabditis elegans*. Nature, 2005. **434**(7032): p. 462-9.
 11. Sieburth, D., et al., *Systematic analysis of genes required for synapse structure and function*. Nature, 2005. **436**(7050): p. 510-7.
 12. Budovskaya, Y.V., et al., *An elt-3/elt-5/elt-6 GATA transcription circuit guides aging in C. elegans*. Cell, 2008. **134**(2): p. 291-303.
 13. Finch, C.E. and G. Ruvkun, *The genetics of aging*. Annual Review of Genomics and Human Genetics, 2001. **2**: p. 435-462.
 14. Sze, J.Y., et al., *Food and metabolic signaling defects in a Caenorhabditis elegans serotonin-synthesis mutant*. Nature, 2000. **403**(6769): p. 560-564.
 15. Estevez, M., et al., *The voltage-gated calcium channel UNC-2 is involved in stress-mediated regulation of tryptophan hydroxylase*. Journal of Neurochemistry, 2004. **88**(1): p. 102-113.
 16. Murakami, H. and S. Murakami, *Serotonin receptors antagonistically modulate Caenorhabditis elegans longevity*. Aging Cell, 2007. **6**(4): p. 483-488.
 17. Liang, B., et al., *Serotonin targets the DAF-16/FOXO signaling pathway to modulate stress responses*. Cell Metabolism, 2006. **4**(6): p. 429-440.
 18. Bishop, N.A. and L. Guarente, *Two neurons mediate diet-restriction-induced longevity in C-elegans*. Nature, 2007. **447**(7144): p. 545-+.
 19. Kenyon, C., *The plasticity of aging: Insights from long-lived mutants*. Cell, 2005. **120**(4): p. 449-460.

20. Kenyon, C., et al., *A C-Elegans Mutant That Lives Twice as Long as Wild-Type*. Nature, 1993. **366**(6454): p. 461-464.
21. Murphy, C.T., et al., *Genes that act downstream of DAF-16 to influence the lifespan of Caenorhabditis elegans*. Nature, 2003. **424**(6946): p. 277-284.
22. Kingsley, D.M., *The Tgf-Beta Superfamily - New Members, New Receptors, and New Genetic Tests of Function in Different Organisms*. Genes & Development, 1994. **8**(2): p. 133-146.
23. Suzuki, Y., et al., *A BMP homolog acts as a dose-dependent regulator of body size and male tail patterning in Caenorhabditis elegans*. Development, 1999. **126**(2): p. 241-250.
24. Sze, J.Y., et al., *The C-elegans POU-domain transcription factor UNC-86 regulates the tph-1 tryptophan hydroxylase gene and neurite outgrowth in specific serotonergic neurons*. Development, 2002. **129**(16): p. 3901-3911.
25. Albertson, D.G. and J.N. Thomson, *Pharynx of Caenorhabditis Elegans*. Philosophical Transactions of the Royal Society of London Series B-Biological Sciences, 1976. **275**(938): p. 299-&.
26. Bargmann, C.I. and H.R. Horvitz, *Control of Larval Development by Chemosensory Neurons in Caenorhabditis-Elegans*. Science, 1991. **251**(4998): p. 1243-1246.
27. Collins, F.S., M. Morgan, and A. Patrinos, *The Human Genome Project: lessons from large-scale biology*. Science, 2003. **300**(5617): p. 286-90.
28. *Geneticist seeks engineer: must like flies and worms*. Nat Methods, 2007. **4**(6): p. 463.

29. Dupuy, D., et al., *Genome-scale analysis of in vivo spatiotemporal promoter activity in Caenorhabditis elegans*. Nat Biotechnol, 2007. **25**(6): p. 663-8.
30. Chalfie, M., et al., *Green Fluorescent Protein as a Marker for Gene-Expression*. Science, 1994. **263**(5148): p. 802-805.
31. Jorgensen, E.M. and S.E. Mango, *The art and design of genetic screens: caenorhabditis elegans*. Nat Rev Genet, 2002. **3**(5): p. 356-69.
32. Keene, A.C. and S. Waddell, *Drosophila olfactory memory: single genes to complex neural circuits*. Nature Reviews Neuroscience, 2007. **8**(5): p. 341-354.
33. Macosko, E.Z., et al., *A hub-and-spoke circuit drives pheromone attraction and social behaviour in C. elegans*. Nature, 2009. **458**(7242): p. 1171-1175.
34. De Vos, K.J., et al., *Role of Axonal Transport in Neurodegenerative Diseases**. Annu. Rev. Neurosci., 2008. **31**: p. 151-173.
35. Bargmann, C.I. and L. Avery, *Laser Killing of Cells in < i > Caenorhabditis elegans < / i >*. Methods in cell biology, 1995. **48**: p. 225-250.
36. Fang-Yen, C., et al., *Laser microsurgery in Caenorhabditis elegans*. Methods Cell Biol, 2012. **107**: p. 177-206.
37. Bulina, M.E., et al., *Chromophore-assisted light inactivation (CALI) using the phototoxic fluorescent protein KillerRed*. Nature Protocols, 2006. **1**(2): p. 947-953.
38. Shibuya, T. and Y. Tsujimoto, *Deleterious effects of mitochondrial ROS generated by KillerRed photodynamic action in human cell lines and < i > C. elegans < / i >*. Journal of Photochemistry and Photobiology B: Biology, 2012.
39. Bulina, M.E., et al., *A genetically encoded photosensitizer*. Nat Biotechnol,

2006. **24**(1): p. 95-9.
40. Bargmann, C.I. and L. Avery, *Laser killing of cells in Caenorhabditis elegans*. *Methods Cell Biol*, 1995. **48**: p. 225-50.
 41. Crowder, C.M., L.D. Shebester, and T. Schedl, *Behavioral effects of volatile anesthetics in Caenorhabditis elegans*. *Anesthesiology*, 1996. **85**(4): p. 901-12.
 42. Massie, M.R., et al., *Exposure to the metabolic inhibitor sodium azide induces stress protein expression and thermotolerance in the nematode Caenorhabditis elegans*. *Cell Stress Chaperones*, 2003. **8**(1): p. 1-7.
 43. Dittrich, P.S., K. Tachikawa, and A. Manz, *Micro total analysis systems. Latest advancements and trends*. *Anal Chem*, 2006. **78**(12): p. 3887-908.
 44. Whitesides, G.M., *The origins and the future of microfluidics*. *Nature*, 2006. **442**(7101): p. 368-73.
 45. Chronis, N., M. Zimmer, and C.I. Bargmann, *Microfluidics for in vivo imaging of neuronal and behavioral activity in Caenorhabditis elegans*. *Nat Methods*, 2007. **4**(9): p. 727-731.
 46. Heng, X., et al., *Optofluidic microscopy--a method for implementing a high resolution optical microscope on a chip*. *Lab Chip*, 2006. **6**(10): p. 1274-6.
 47. Hulme, S.E., et al., *A microfabricated array of clamps for immobilizing and imaging C. elegans*. *Lab Chip*, 2007. **7**(11): p. 1515-23.
 48. Guo, S.X., et al., *Femtosecond laser nanoaxotomy lab-on-a-chip for in vivo nerve regeneration studies*. *Nature Methods*, 2008. **5**(6): p. 531-533.
 49. Zeng, F., C.B. Rohde, and M.F. Yanik, *Sub-cellular precision on-chip small-animal immobilization, multi-photon imaging and femtosecond-laser*

- manipulation*. Lab Chip, 2008. **8**(5): p. 653-6.
50. Chung, K., M.M. Crane, and H. Lu, *Automated on-chip rapid microscopy, phenotyping and sorting of C. elegans*. Nat Methods, 2008. **5**(7): p. 637-43.
 51. Crane, M.M., K. Chung, and H. Lu, *Computer-enhanced high-throughput genetic screens of C. elegans in a microfluidic system*. Lab Chip, 2009. **9**(1): p. 38-40.
 52. Unger, M.A., et al., *Monolithic microfabricated valves and pumps by multilayer soft lithography*. Science, 2000. **288**(5463): p. 113-6.
 53. Stirman, J.N., et al., *High-throughput study of synaptic transmission at the neuromuscular junction enabled by optogenetics and microfluidics*. J Neurosci Methods, 2010. **191**(1): p. 90-3.
 54. Chokshi, T.V., D. Bazopoulou, and N. Chronis, *An automated microfluidic platform for calcium imaging of chemosensory neurons in Caenorhabditis elegans*. Lab Chip, 2010. **10**(20): p. 2758-63.
 55. Chung, K. and H. Lu, *Automated high-throughput cell microsurgery on-chip*. Lab Chip, 2009. **9**(19): p. 2764-6.
 56. Guo, S.X., et al., *Femtosecond laser nanoaxotomy lab-on-a-chip for in vivo nerve regeneration studies*. Nat Methods, 2008. **5**(6): p. 531-3.
 57. Hulme, S.E., et al., *Lifespan-on-a-chip: microfluidic chambers for performing lifelong observation of C. elegans*. Lab Chip, 2010. **10**(5): p. 589-97.
 58. Chung, K., et al., *Microfluidic chamber arrays for whole-organism behavior-based chemical screening*. Lab Chip, 2011. **11**(21): p. 3689-97.
 59. Weibel, D.B., et al., *Torque-actuated valves for microfluidics*. Anal Chem,

2005. **77**(15): p. 4726-33.
60. Hulme, S.E., S.S. Shevkoplyas, and G.M. Whitesides, *Incorporation of prefabricated screw, pneumatic, and solenoid valves into microfluidic devices*. Lab Chip, 2009. **9**(1): p. 79-86.
61. Thorsen, T., S.J. Maerkl, and S.R. Quake, *Microfluidic large-scale integration*. Science, 2002. **298**(5593): p. 580-4.
62. Duffy, D.C., et al., *Rapid Prototyping of Microfluidic Systems in Poly(dimethylsiloxane)*. Anal Chem, 1998. **70**(23): p. 4974-84.
63. Brenner, S., *The genetics of Caenorhabditis elegans*. Genetics, 1974. **77**(1): p. 71-94.
64. Lotters, J.C., et al., *The mechanical properties of the rubber elastic polymer polydimethylsiloxane for sensor applications*. Journal of Micromechanics and Microengineering, 1997. **7**(3): p. 145-147.
65. Carrillo, F., et al., *Nanoindentation of polydimethylsiloxane elastomers: Effect of crosslinking, work of adhesion, and fluid environment on elastic modulus*. Journal of Materials Research, 2005. **20**(10): p. 2820-2830.
66. Gervais, T., et al., *Flow-induced deformation of shallow microfluidic channels*. Lab Chip, 2006. **6**(4): p. 500-507.
67. Studer, V., et al., *Scaling properties of a low-actuation pressure microfluidic valve*. Journal of Applied Physics, 2004. **95**(1): p. 393-398.
68. Estevez, M., et al., *The voltage-gated calcium channel UNC-2 is involved in stress-mediated regulation of tryptophan hydroxylase*. J Neurochem, 2004. **88**(1): p. 102-13.

69. Zhang, Y., H. Lu, and C.I. Bargmann, *Pathogenic bacteria induce aversive olfactory learning in Caenorhabditis elegans*. *Nature*, 2005. **438**(7065): p. 179-84.
70. Estevez, A.O., et al., *Both insulin and calcium channel signaling are required for developmental regulation of serotonin synthesis in the chemosensory ADF neurons of Caenorhabditis elegans*. *Dev Biol*, 2006. **298**(1): p. 32-44.
71. Lee, H., et al., *Quantitative screening of genes regulating tryptophan hydroxylase transcription in Caenorhabditis elegans using microfluidics and an adaptive algorithm*. *Integr Biol (Camb)*, 2012.
72. Chung, K. and H. Lu, *Automated high-throughput cell microsurgery on-chip*. *Lab on a Chip*, 2009. **9**(19): p. 2764-2766.
73. Rohde, C.B., et al., *Microfluidic system for on-chip high-throughput whole-animal sorting and screening at subcellular resolution*. *Proceedings of the National Academy of Sciences*, 2007. **104**(35): p. 13891-13895.
74. Chronis, N., M. Zimmer, and C.I. Bargmann, *Microfluidics for in vivo imaging of neuronal and behavioral activity in Caenorhabditis elegans*. *Nature methods*, 2007. **4**(9): p. 727-731.
75. Zeng, F., C.B. Rohde, and M.F. Yanik, *Sub-cellular precision on-chip small-animal immobilization, multi-photon imaging and femtosecond-laser manipulation*. *Lab Chip*, 2008. **8**(5): p. 653-656.
76. Crane, M.M., et al., *Autonomous screening of C. elegans identifies genes implicated in synaptogenesis*. *Nat Methods*, 2012. **9**(10): p. 977-80.
77. Stirman, J.N., et al., *High-throughput study of synaptic transmission at the*

- neuromuscular junction enabled by optogenetics and microfluidics*. Journal of neuroscience methods, 2010. **191**(1): p. 90-93.
78. Hulme, S.E., et al., *A microfabricated array of clamps for immobilizing and imaging C. elegans*. Lab Chip, 2007. **7**(11): p. 1515-1523.
79. Shi, W., et al., *Droplet microfluidics for characterizing the neurotoxin-induced responses in individual Caenorhabditis elegans*. Lab Chip, 2010. **10**(21): p. 2855-63.
80. Stiernagle, T., *Maintenance of C. elegans*. WormBook, 2006: p. 1-11.
81. Stirman, J.N., et al., *Real-time multimodal optical control of neurons and muscles in freely behaving Caenorhabditis elegans*. Nat Methods, 2011. **8**(2): p. 153-8.
82. Chalfie, M., et al., *The neural circuit for touch sensitivity in Caenorhabditis elegans*. The Journal of neuroscience, 1985. **5**(4): p. 956-964.
83. Chatzigeorgiou, M., et al., *Spatial asymmetry in the mechanosensory phenotypes of the C. elegans DEG/ENaC gene mec-10*. Journal of neurophysiology, 2010. **104**(6): p. 3334-3344.
84. Wicks, S.R. and C.H. Rankin, *Integration of mechanosensory stimuli in Caenorhabditis elegans*. The Journal of neuroscience, 1995. **15**(3): p. 2434-2444.
85. Avery, L. and H.R. Horvitz, *Effects of starvation and neuroactive drugs on feeding in Caenorhabditis elegans*. J Exp Zool, 1990. **253**(3): p. 263-70.
86. Qi, Y.B., et al., *Photo-inducible cell ablation in Caenorhabditis elegans using the genetically encoded singlet oxygen generating protein miniSOG*. Proc Natl

- Acad Sci U S A, 2012. **109**(19): p. 7499-504.
87. Shu, X., et al., *A genetically encoded tag for correlated light and electron microscopy of intact cells, tissues, and organisms*. PLoS Biol, 2011. **9**(4): p. e1001041.
 88. Neumann, B., et al., *Axonal regeneration proceeds through specific axonal fusion in transected C. elegans neurons*. Dev Dyn, 2011. **240**(6): p. 1365-72.
 89. Kirszenblat, L., et al., *A dominant mutation in MEC-7/beta-tubulin affects axon development and regeneration in C. elegans neurons*. Mol Biol Cell, 2012.
 90. Chung, K., et al., *A microfluidic array for large-scale ordering and orientation of embryos*. Nat Methods, 2011. **8**(2): p. 171-6.
 91. Hilliard, M.A., *Axonal degeneration and regeneration: a mechanistic tug-of-war*. Journal of Neurochemistry, 2009. **108**(1): p. 23-32.
 92. Kirszenblat, L., et al., *A dominant mutation in mec-7/beta-tubulin affects axon development and regeneration in Caenorhabditis elegans neurons*. Mol Biol Cell, 2013. **24**(3): p. 285-96.
 93. Qin, Y.Q., X.D. Zhang, and Y. Zhang, *A Neuronal Signaling Pathway of CaMKII and Gq alpha Regulates Experience-Dependent Transcription of tph-1*. Journal of Neuroscience, 2013. **33**(3): p. 925-935.
 94. Ha, H.I., et al., *Functional Organization of a Neural Network for Aversive Olfactory Learning in Caenorhabditis elegans*. Neuron, 2010. **68**(6): p. 1173-1186.
 95. Chokshi, T.V., D. Bazopoulou, and N. Chronis, *An automated microfluidic*

platform for calcium imaging of chemosensory neurons in Caenorhabditis elegans. Lab Chip, 2010. **10**(20): p. 2758-2763.

96. Chalasani, S.H., et al., *Dissecting a circuit for olfactory behaviour in Caenorhabditis elegans*. Nature, 2007. **450**(7166): p. 63-+.